

Epitaxy of group IV optical materials and synthesis of IV/III-V
semiconductor analogs by designer hydride chemistries

by

Gordon Grzybowski

A Dissertation Presented in Partial Fulfillment
of the Requirements for the Degree
Doctor of Philosophy

Approved April 2013 by the
Graduate Supervisory Committee:

John Kouvetakis, Chair
Andrew Chizmeshya
Jose Menéndez

ARIZONA STATE UNIVERSITY

May 2013

ABSTRACT

The thesis studies new methods to fabricate optoelectronic $\text{Ge}_{1-y}\text{Sn}_y/\text{Si}(100)$ alloys and investigate their photoluminescence (PL) properties for possible applications in Si-based photonics including IR lasers. The work initially investigated the origin of the difference between the PL spectrum of bulk Ge, dominated by indirect gap emission, and the PL spectrum of Ge-on-Si films, dominated by direct gap emission. It was found that the difference is due to the suppression of self-absorption effects in Ge films, combined with a deviation from quasi-equilibrium conditions in the conduction band of undoped films. The latter is confirmed by a model suggesting that the deviation is caused by the shorter recombination lifetime in the films relative to bulk Ge. The knowledge acquired from this work was then utilized to study the PL properties of n-type $\text{Ge}_{1-y}\text{Sn}_y/\text{Si}$ ($y=0.004-0.04$) samples grown via chemical vapor deposition of $\text{Ge}_2\text{H}_6/\text{SnD}_4/\text{P}(\text{GeH}_3)_3$. It was found that the emission intensity (I) of these samples is at least 10x stronger than observed in un-doped counterparts and that the $I_{\text{dir}}/I_{\text{ind}}$ ratio of direct over indirect gap emission increases for high-Sn contents due to the reduced Γ -L valley separation, as expected. Next the PL investigation was expanded to samples with $y=0.05-0.09$ grown via a new method using the more reactive Ge_3H_8 in place of Ge_2H_6 . Optical quality, 1- μm thick $\text{Ge}_{1-y}\text{Sn}_y/\text{Si}(100)$ layers were produced using $\text{Ge}_3\text{H}_{10}/\text{SnD}_4$ and found to exhibit strong, tunable PL near the threshold of the direct-indirect bandgap crossover. A byproduct of this study was the development of an enhanced process to produce Ge_3H_8 , Ge_4H_{10} , and Ge_5H_{12} analogs for application in ultra-low temperature deposition of Group-IV semiconductors.

The thesis also studies synthesis routes of an entirely new class of semiconductor compounds and alloys described by $\text{Si}_{5-2y}(\text{III-V})_y$ (III=Al, V= As, P) comprising of specifically designed diamond-like structures based on a Si parent lattice incorporating

isolated III-V units. The common theme of the two thesis topics is the development of new mono-crystalline materials on ubiquitous silicon platforms with the objective of enhancing the optoelectronic performance of Si and Ge semiconductors, potentially leading to the design of next generation optical devices including lasers, detectors and solar cells.

ACKNOWLEDGMENTS

I am unable to imagine the completion of this work without the help and guidance of my advisor Dr. John Kouvetakis who took the time to mentor me through countless discussions, emails, and experiments. He proved to be a wealth of knowledge and an ever-present source of motivation throughout this process. I would also like to thank my committee members Dr. Andrew Chizmeshya and Dr. José Menéndez. Their knowledge of computational chemistry and electronic and optical properties of materials was pivotal in both influencing the direction of my research and in my understanding and the subtle nuances and the larger picture of my efforts.

I would also like to thank the members of my research group. Specifically I would like to thank Dr. Richard Beeler for his help with the plethora of growth systems and characterization techniques and for always being someone I could count on to lend a hand with the difficult tasks. Special thanks to Dr. Jesse Tice is also deserved for his patience with me as I learned the chemistry techniques and kept him from his family well past reasonable working hours. I would also like to thank Chi Xu and Liying Jiang for their help with ellipsometry, microscopy, and photoluminescence.

I gratefully acknowledge use of the facilities and equipment of the Center for Solid State Science (CSSS), the Center for High Resolution Electron Microscopy (CHREM) and the Center for Solid State Electronics Research (CSSER).

Additionally, I appreciate the help provided by Barry Wilkens with ion beam analysis and David Wright for his knowledge and help in maintenance and materials for experiments and laboratory equipment.

This work was funded by the National Science Foundation (DMR-0907600), U.S. Air Force (MURI program DOD AFOSR FA9550-06-01-0442), and U.S. Department of Energy (DE-FG36-08GO18003). Voltaix, LLC provided digermane used in this work.

Lastly, I am thankful to my friends and family. Special thanks to my parents Gordon and Nancy Grzybowski for the love, support, and care they have provided to me over the years, and for instilling a good work ethic in my siblings and I. Finally, I would like to thank the love of my life, my wonderful wife Raeleen, who puts up with my constant absence and has remained loving, steadfast, and grounded through this trying process.

TABLE OF CONTENTS

	Page
LIST OF TABLES	viii
LIST OF FIGURES.....	ix
CHAPTER	
1 INTRODUCTION.....	1
A. Germanium Tin alloys	2
B. Group IV(III-V) alloys	7
2 DIRECT VS. INDIRECT OPTICAL RECOMBINATION IN GERMANIUM FILMS GROWN ON SILICON SUBSTRATES.....	11
A. Introduction.....	11
B. Experimental.....	12
C. Results and discussion.....	13
D. Non-equilibrium model.....	21
E. Band gap renormalization	24
F. Conclusion.....	26
3 PHOTOLUMINESCENCE FROM N TYPE GERMANIUM TIN MATERIALS GROWN ON SILICON(100) BY DIGERMANE.....	28
A. Introduction.....	28
B. Results and discussion.....	29
C. Summary	35
4 NEXT GENERATION GERMANIUM TIN ALLOYS GROWN ON SILICON BY TRIGERMANE WITH TIN CONTENTS OF 1-9%: REACTION KINETICS AND TUNABLE EMISSION	36
A. Introduction	36

CHAPTER	Page
B. Results and discussion.....	38
C. Summary	46
5 INTRODUCING HIGHER ORDER GERMANES FOR THE ULTRA LOW EPITAXY OF GERMANIUM BASED SEMICONDUCTORS: TRIGERMANE, TETRAGERMANE	47
A. Introduction.....	47
B. Experimental results and discussion	52
C. Quantum chemical simulations of structural, vibrational, and thermochemical properties	56
D. Thermochemistry of tetragermanes.....	60
E. conclusion	65
6 GROUP III-V/IV ALLOYS OF ALUMINUM, PHOSPHOROUS, ARSENIC, AND SILICON GROWN ON SI(100)	66
A. Introduction.....	66
B. Theoretical predictions.....	67
C. Simulations of crystal structures and their properties	73
D. 10 Atom cell description	75
E. Band structure calculations.....	77
F. Experimental procedures	80
G. Synthesis and structural characterization of AlAsSi ₃	81
H. Synthesis and structural characterization of Al(As _{1-x} P _x)Si ₃ alloys.....	84
I. Raman studies	87
J. Conclusion.....	90

CHAPTER	Page	
7	QUANTUM CHEMICAL SIMULATIONS ON THE STRUCTURE, BONDING , AND REACTIVITIES OF (IV) ₃ M PRECURSORS AND THE THERMODYNAMICS OF CORRESPONDING (III-V)IV SOLID STRUCTURES.....	91
	A. Introduction.....	91
	B. Structural and bonding insights from first principle simulations.....	93
	C. Summary.....	104
	REFERENCES	106
APPENDIX		
A	SYNTHESIS OF REACTANTS	115
B	COPYRIGHT RELEASE AUTHORIZATIONS	121

LIST OF TABLES

Table	Page
1. Structural and energetic computational results for trigermane and the isomers and conformers of tetragermane	57
2. Summary of LDA equilibrium crystalline properties calculated for (III-V)IV ₃ alloys, binary alloys, and elemental reference states	100

LIST OF FIGURES

Figure	Page
1.	Room temperature PL spectrum of a Ge-on-Si film compared with the corresponding spectrum from bulk Ge after self-absorption corrections 14
2.	Population ratio for the Γ - and L -valleys in the conduction band of Germanium as a function of the total electron density in the conduction band..... 16
3.	Room temperature PL spectrum of a fully relaxed, n -type Ge-on-Si film with a thickness of 1200 nm and carrier density of $1.9 \times 10^{19} \text{ cm}^{-3}$, as grown 19
4.	Room temperature PL intensity from p -type Ge-on-Si samples.....23
5.	Room temperature PL spectrum from Ge-on-Si films with different P doping concentrations.....25
6.	Room temperature PL signal of n -type $\text{Ge}_{1-y}\text{Sn}_y$ samples as-grown and after rapid thermal annealing 31
7.	Room temperature PL from annealed $\text{Ge}_{0.975}\text{Sn}_{0.025}$ samples The weaker signal corresponds to nominally intrinsic material.....33
8.	Ratio of direct and indirect emission intensities for annealed doped $\text{Ge}_{1-y}\text{Sn}_y$ samples.....35
9.	Sn/Ge ratio in $\text{Ge}_{1-y}\text{Sn}_y$ films on Si vs. the corresponding ratio in the gaseous mixture for the $\text{Ge}_2\text{H}_6/\text{SnD}_4$ and $\text{Ge}_3\text{H}_8/\text{SnD}_4$ deposition reactions..... 40
10.	TEM micrographs of a 7% and 8% and tin GeSn alloy layer showing the high-resolution interface and bulk material42
11.	HR-XRD 224 plots GeSn alloys containing 2.5, 5.2 and 7% tin, and RBS spectrum of 5, 8, and 9% tin films.....44

Figure	Page
12. Room temperature photoluminescence spectra from $\text{Ge}_{1-y}\text{Sn}_y$ alloys on containing 0 to 8% tin Si substrates.....	45
13. Molecular structures of trisilane (Si_3H_8) trigermane (Ge_3H_8) and the two isomers of tetragermane (Ge_4H_{10}).....	50
14. NMR spectra of the isomeric tetragermane mixture	55
15. Comparison of the calculated and experimental FTIR spectrum for trigermane.....	59
16. Low and high frequency FTIR spectra of the individual isomers of tetragermane used to construct the composite spectrum	61
17. Calculated temperature dependence of the tetragermane isomer mol fractions from 200-600K and the composite gas phase FTIR spectrum of tetragermane isomers	64
18. Calculated structure of $\text{AlAs}_{0.25}\text{P}_{0.75}\text{Si}_3$ showing tetrahedral AlAsSi_3 and AlPSi_3 building blocks incorporated into the structure	69
19. Calculated equilibrium structures of $(\text{SiH}_3)_3\text{As}$ and $(\text{SiH}_3)_3\text{P}$, their bonded structures to AlH_3 , and the tetrahedral AlAsSi_3 and AlPSi_3 dimensions extracted from their respective crystal structures	72
20. Structural models and specification of atomic positions for the 20-atom unit cell of III-V-IV ₃ compounds	74
21. Silicon lattice with lines designating the monoclinic 10-atom (C1c1) representation containing two III-V-(IV) ₃ units.....	76
22. Comparison of the band structure of silicon Si and AlAsSi_3 using a common 10-atom base-centered monoclinic setting	77

Figure	Page
23. Band structure plots for AlPSi_3 , $\text{Al}(\text{P}_{0.5}\text{As}_{0.5})\text{Si}_3$, and AlAsSi_3 in the band gap region.....	78
24. RBS spectra of Si/As/Al films showing well-separated As, Si, and Al signals. XTEM micrograph of the entire AlAsSi_3 layer thickness exhibiting threading defects penetrating to the surface	82
25. 224 HR-XRD map of the 260 nm thick AlAsSi_3 exhibiting bimodal growth.	83
26. RBS spectra of an alloy sample acquired at 2 MeV showing that the signals of Al, Si, P, and As exhibit the same degree of channeling, indicating single phase material.....	85
27. XRD plots of $\text{Si}_3\text{AlAs}_{0.25}\text{P}_{0.75}/\text{Si}(100)$ showing that the alloy peak is in-plane lattice matching and XTEM micrographs showing a largely defect free bulk material..	86
28. Experimental and theoretical Raman spectra for AlAsSi_3 and $\text{Al}(\text{As}_{1-x}\text{P}_x)\text{Si}_3$ films.....	89
29. Equilibrium structures of $(\text{SiH}_3)_3\text{M}$ for $\text{M} = \text{P}, \text{As},$ and N in both unbonded and bonded to configurations with AlH_3 . Electrostatic potential maps indicating nucleophilicity and tetrahedral character of intermediates extracted from $(\text{SiH}_3)_3\text{M}-\text{AlH}_3$ species.....	96
30. Structures and of molecular cores extracted from equilibrium crystal structures (and lattice constants) of AlNSi_3 , AlPSi_3 , and AlAsSi_3 indicating a regularization of tetrahedral units in the sequence N, P, and As	102
31. Structural models of AlNSi_3 and AlAsSi_3 illustrating deviation from perfect tetrahedral atomic positions by the nitride	103

Figure	Page
32. Formation energies of AlPSi_3 , AlAsSi_3 , and AlSbSi_3 compounds relative to the elements and binary AlN , AlP , and AlAs alloys	104

Chapter 1

INTRODUCTION

The importance of group IV materials to today's technology-based society cannot be overstated. The elemental semiconductors silicon and germanium provide the materials that are found in many of the current generation devices such as solar cells, detectors, and microprocessors. The use of these materials by the electronics industry has allowed the development of technologies such as mobile phones, the internet, and personal computers. Widespread use of electronics in all aspects of our lives has led to the need for increased energy production and the desire for smaller and more efficient devices, yielding both reductions in power use and increased device capability for the end user. As the current dominant technology, group IV semiconductors are advantageously placed to provide the basis for development of new and functional materials that will be needed for future generation of devices. These new group IV materials based on silicon and germanium will provide greater absorption and emission capabilities than the current systems, leading to increased functionality and efficiency for applications such as photovoltaics for power production, and detectors. Additionally they will lead to new light emission devices suitable for laser applications.

For ease of implementation, it would be advantageous for newly developed materials to be compatible with current deposition and processing technologies. The most straightforward way to accomplish this is to produce new materials based on silicon and germanium that extend their current capabilities. An additional advantage can be realized if these materials can be directly integrated on silicon, due to current widespread availability of low cost, large area Si substrates. Optical devices integrated with the latter also provide the opportunity for silicon based photonics and structures combining both optical and electronic capabilities on a single device. Two materials that

are currently in development for these types of applications are $\text{Ge}_{1-x}\text{Sn}_x$ and Group IV/(III-V) alloys grown directly on silicon.

GeSn Background

Elemental germanium is an indirect semiconductor with an indirect band gap of 0.66eV. The difference between the band gap and the lowest direct gap is only 0.14eV. This unique electronic structure has motivated considerable research efforts seeking to modify the band structure of germanium to make it suitable for optoelectronic applications. For instance, semiconductor lasers require direct gap materials because luminescence from indirect gaps is extremely inefficient due to the necessary participation of phonons in the radiative recombination process. Accordingly, several methods have been developed to enhance the luminescence in germanium by inducing direct or near-direct gap conditions.

The application of tensile strain to the germanium lattice has been proposed to reduce the separation of the direct and indirect gaps and lower the gap energies making the material more direct.¹ However, the introduction of strain into vapor deposited germanium films on Si is theoretically limited to a value of $\xi = 0.3$, due to the maximum levels that can be introduced by the mismatch of thermal expansivities between Ge and Si. This amount of strain is not enough to achieve direct gap conditions. Another method that has been shown to have equivalent effects to strain is the incorporation of tin into the germanium lattice², first proposed in 1982.³

In contrast to germanium, tin is typically found in the diamond structure only at temperatures lower than 13°C⁴, where it exhibits a “negative” direct band gap of -0.4eV. Accordingly, the incorporation of Sn into the germanium lattice as a substitutional impurity has been theoretically predicted to lower the energy of both the direct and indirect gap energies, and to lower the separation between the indirect and direct gaps,

ultimately leading to a direct gap material in the infrared range.⁵ The calculations indicated that the indirect to direct crossover should occur with 20% tin incorporation into the alloy. Recent photoluminescence experiments with $\text{Ge}_{1-x}\text{Sn}_x$ alloys grown on Si(100) qualitatively corroborate the early theoretical band structure changes, but indicate the crossover to occur at a much lower concentration, below 10%.⁶ If the indirect to direct crossover can be realized, efficient light emission from group IV materials should be observed for the first time due to the direct gap nature of the material.

Alloys of $\text{Ge}_{1-x}\text{Sn}_x$ in general pose an exciting possibility due to the ability to tune the band gap of a wide range of compositions grown directly on silicon using CVD routes. However, thus far the experimentally observed photoluminescence and electroluminescence intensity from such materials has been too weak for application in light emission devices.⁶ This thesis work with $\text{Ge}_{1-x}\text{Sn}_x$ alloys was directed at the goal of enhancing the light emission of these materials in preparation for their application to prototype device structures for silicon photonic applications.

Recent work on germanium light emission from MIT has yielded an electrically pumped laser. Near direct gap conditions were achieved through the application of strain and n-type doping of the germanium structure.⁷ Increased direct emission by n-type doping has been extensively reported.^{7,8} Incorporation of n-type dopants such as phosphorous elevates the Fermi level such that the population of the direct valley is increased. The higher population results in an enhancement in the observed radiative recombination during photoluminescence. Similar to germanium, $\text{Ge}_{1-x}\text{Sn}_x$ alloy light emission is also increased through the application of n-type doping as shown for the first time in this thesis work.

The underlying requirements for the production of efficient light emitting germanium materials highlighted in these previous methodologies are the production

highly doped and highly substituted $\text{Ge}_{1-x}\text{Sn}_x$ films with tensile strain states conducive to the observation of radiative recombination. Recent experimental and theoretical data on $\text{Ge}_{1-x}\text{Sn}_x$ films on silicon has indicated that the incorporation of 1% Sn is equivalent to a strain of $\xi = 0.35$.⁶ Comparison with the theoretical maximum value of strain in vapor deposited thin films suggests that attempting strain manipulation would yield a smaller effect than the incorporation of large amounts of substitutional Sn. Accordingly, efforts to increase light emission should be focused on the maximum incorporation of substitutional Sn into the germanium lattice. Thin $\text{Ge}_{1-x}\text{Sn}_x$ films with Sn contents up to 17%,⁹ well above the recent prediction of the indirect-direct crossover, below 10%, have already been realized. However, luminescence from these films has not been achieved. A major observation of recent photoluminescence studies of GeSn films on silicon is the requirement of thick active layers in which the useful volume fraction (near the 500 nm range) from the film away for the defective interface has been significantly increases to induce of PL. This requirement is presumably due to the non-radiative recombination of carriers at the intrinsically defected silicon-germanium interface.¹⁰ As a result of this non-radiative recombination channel, the enhancement of light emission of germanium tin materials is inherently tied, not only to the incorporation of Sn, but also to the production of thick, high crystal quality layers with low concentrations of deleterious threading defects.

The thermodynamics of the $\text{Ge}_{1-x}\text{Sn}_x$ system present significant hurdles for the production of highly saturated solid solutions in thick film form. The solubility of tin in germanium has been found to be less than $\sim 1.1\%$.¹¹ Accordingly the depositions must be conducted at low temperatures. The thermodynamic incompatibility is highlighted by attempts at producing thin films on silicon by MBE growth, where α -Sn crystal growth has been optimized at 25°C ¹² and germanium growth requires temperatures exceeding

300°C.¹³ The low growth temperature required by MBE growth of GeSn films limits the achievable thickness, making the process unsuitable for the production of bulk like layers. Similarly, the use of chemical vapor deposition (CVD) technologies is not without issue.

Growth of CVD germanium films in optoelectronics is most commonly conducted with germane due to its commercial availability and purity. However, the relatively high growth temperatures of germane depositions ($\sim 350^\circ\text{C}$)¹⁴ preclude its compatibility with the production of $\text{Ge}_{1-x}\text{Sn}_x$ films with high tin compositions. Additionally, CVD technologies are also limited by the low availability of suitable sources of molecular tin. A significant milestone in CVD production of $\text{Ge}_{1-x}\text{Sn}_x$ alloys was the introduction of Ge_2H_6 as a germanium source with highly reactive and suitably volatile hydride of tin. The first such source was, PhSnD_3 ,¹⁵ which was ultimately replaced by the carbon-free SnD_4 .⁹ The use of $\text{Ge}_2\text{H}_6/\text{SnD}_4$ CVD reactions has led directly to the growth and fabrication of the first $\text{Ge}_{1-x}\text{Sn}_x$ diode devices with extended near-IR responsivity,¹⁶⁻¹⁸ and the observation of tunable gap emission in $\text{Ge}_{1-x}\text{Sn}_x$ films up to $x = 0.04$.^{5,19}

A remarkable feature of the emission spectra of $\text{Ge}_{1-x}\text{Sn}_x$ films on silicon is the dominance of the direct gap photoluminescence. This is in contrast to the indirect nature of bulk germanium. Chapter 2 of this work investigates intrinsic and n-doped germanium tin films with low tin contents in order to determine the mechanism by which the indirect gap is suppressed relative to the direct gap. The data, explained using a simple model, suggests that the conduction bands of intrinsic films deviate from quasi-equilibrium conditions due to shorter carrier lifetimes in the films when compared to the bulk material. The deviations occur because electron-hole pair lifetimes in these films are shorter due to non-radiative recombination at the film-substrate interface. It is also noted that due to the very long ambipolar diffusion length in bulk germanium, the direct

gap emission is preferentially suppressed by reabsorption. By contrast, when the layer thickness is much less than the ambipolar diffusion length, self-absorption effects are not important, and the direct gap luminescence becomes relatively stronger.

The dominance of the direct gap emission has been observed in $\text{Ge}_2\text{H}_6/\text{SnD}_4$ grown films up to 4% tin. However, for applications in light emission the luminescence intensity is far too low particularly for uses in laser structures. In order to enhance the observed intensity Chapter 3 reports the growth of n-type $\text{Ge}_{1-x}\text{Sn}_x$ films using $\text{P}(\text{GeH}_3)_3$ as a source of activated phosphorous dopant atoms. To this end n-type and intrinsic $\text{Ge}_{1-x}\text{Sn}_x$ films on Si (100) with compositions up to 3.6% tin were grown using Ge_2H_6 and SnD_4 in conventional hot wall CDV experiments with dopant levels up to 6×10^{19} atoms/cm³. The $\text{P}(\text{GeH}_3)_3$ phosphorous source is compatible with the low growth temperatures required to produce the metastable $\text{Ge}_{1-x}\text{Sn}_x$ compounds, and affords complete incorporation and full activation of the phosphorous.²⁰ PL studies of the resultant n-type films show an enhancement by at least 10 times compared to intrinsic materials, indicating the validity of the doping concept and applicability of the growth methods for the improving the optical response from $\text{Ge}_{1-x}\text{Sn}_x$ alloys on silicon. Using digermane the growth of thick optical quality $\text{Ge}_{1-x}\text{Sn}_x$ films with concentrations above 4 % Sn could not be achieved due to the reductions in growth rates, residual strains, and limited thicknesses with decreasing growth temperatures required for the production of higher tin content films. A new approach was then developed using trigermane (Ge_3H_8) as a low temperature germanium source to produce samples with appropriate thicknesses, defectivities, and relaxed strain states. Chapter 4 details the growths of intrinsic and n-type $\text{Ge}_{1-x}\text{Sn}_x$ alloys using Ge_3H_8 and SnD_4 . The data shows trigermane is a superior alternative to Ge_2H_6 enabling the growth of $\text{Ge}_{1-x}\text{Sn}_x$ alloys with tin contents as high as $x=0.09$. The lower thermal activation energy of trigermane

makes it a more suitable co-reactant for SnD_4 and allows the production of thick optical quality films characterized by PL measurements, and showing a wider range of tunability within the $\text{Ge}_{1-x}\text{Sn}_x$ system.

Chapter 5 covers the development and optimization of an enhanced process to produce Ge_3H_8 , as well as tetragermane (Ge_4H_{10}) analog for application in ultra-low temperature deposition of Ge based semiconductors. The molecules were produced in gram-scale quantities with semiconductor grade purity via a simple, single-step thermolysis reaction of Ge_2H_6 in a flow system using H_2 as the carrier gas. The identity and fundamental structural properties of these higher order germanes (including Ge_4H_{10} isomers) were thoroughly characterized using spectroscopic methods, and quantum chemical simulations. More importantly these hydride products were found to exhibit a remarkable stability and a “ease of use” comparable to conventional group IV chemical sources, making them compatible with current industry standards. The above described applications of Ge_3H_8 as efficient and cost-effective precursors for ultra-low temperature CVD growth GeSn alloy films directly on Si(100) wafers, at conditions compatible with processes currently employed in next-generation group IV device designs suggest the potential for rapid adoption into the device application arena. In the case of GeSn alloys as indicated above the high growth rates achieved at low temperatures allow the formation of highly concentrated bulk-like layers with unprecedented thicknesses compatible with Si-based photonic applications such as IR emitters and detectors directly on Si wafers.

Silicon-like (III-V/IV) alloys

An alternative group of materials that offers an extension of traditional group IV semiconductor capabilities are IV(III-IV) compounds which represent hybrids of the IV and III-V end members. Alloys of such group IV and III-V phases have attracted

considerable attention for some time.²¹⁻²⁶ An important subclass consist of combinations of elements from the same row of the periodic table, for which the group IV diamond and group III-V zinblende materials have nearly identical lattice parameters but different electronic structures. This property is potentially useful for multijunction solar cells, which require the stacking of compounds with increasing band gaps with the restriction that they must also share a common lattice parameter to avoid defect generation. A good example of such application is the $(\text{Ge}_2)_{1-x}(\text{GaAs})_x$ alloy with x adjusted to obtain a band gap close to 1 eV, has been identified as candidate material to be incorporated as the second junction in Ge / 1 eV / InGaAs / InGaP 4-junction solar cells.²⁵ The very similar lattice constants of Al- and Ga- compounds sharing the same anion (AlP/GaP, AlAs/GaAs, AlSb/GaSb) should add to the versatility of this approach by providing extended families of (III-V)-(IV) compounds with common lattice parameters and tunable band gaps.

(III-V)-(IV) alloys are also of great interest from a fundamental perspective because they exhibit a fascinating interplay between the zinblende symmetry, which requires that the group III and group V elements be located on separate sublattices, and the diamond structure, where the two sublattices are equivalent. Thus at very low concentrations group III or group-V atoms in Si, Ge, or Sn are not sensitive to their sublattice location. It has been argued theoretically that the zinblende-diamond interplay leads to a phase transition between ordered and disordered sublattices, which might explain the unusual compositional dependences of some alloy properties.²⁷ The possibility of phase transitions has elicited a lively controversy in the literature.²⁸⁻³⁰ Aside from $(\text{Ge}_2)_{1-x}(\text{GaAs})_x$, several other IV/III-V compounds have been experimentally explored using different growth methods with the common feature that the III-V and group-IV components are separately delivered and allowed to react at relatively high

temperatures. The material systems range from BNC_2 (a hybrid between diamond C and c-BN), which has recently been shown to exhibit hardnesses that rival that of diamond,³¹ to $(\text{Ge}_2)_{1-x}(\text{GaSb})_x$ (Ref.32). However, the systematic exploration of the very rich physics and potentially exciting applications of (III-V)-(IV) alloys has been traditionally hindered by the very severe phase separation that plagues these systems. Because of these issues, the interest in (III-V)-(IV) materials has been on the wane for the past decade.

A significant breakthrough in the field of (III-V)-(IV) alloys occurred in 2011 in my lab at ASU, as an entirely new approach to the synthesis of these materials was introduced that was specifically designed to avoid phase separation issues. Key to this success was the use of $(\text{H}_3\text{-IV})_3\text{V}$ molecules as CVD growth precursors. When one such compound— $(\text{H}_3\text{Si})_3\text{P}$ —was combined with Al atoms generated from a Knudsen cell, thick mono-crystalline films with AlPSi_3 stoichiometry grew pseudomorphically on Si (100) substrates with excellent crystallinity and no hint of phase separation.³³ The incorporation of tetrahedral building blocks in the (III-V)IV alloys produced by this method create an interesting structural motif in which the central group V atoms are 3rd nearest neighbors. Raman spectra have indicated that the tetrahedral units are orientationally disordered. The growth method was subsequently extended to $\text{Si}_{5-2y}(\text{AlP})_y$ alloys with tunable Si concentrations, effectively lowering the concentration of the substitutional impurities in the silicon matrix.³⁴

ALP donor-acceptor pairs have been shown to seamlessly incorporate due to the similar lattice constants of the parent compounds, ALP and silicon. Work in this thesis represents the expansion from the in row-lattice matched materials to lattice mismatched growth, providing the basis and proof of concept for the development of a wide range of film compositions that are represented by the general form (III-V) (IV)_x.

The most straightforward deviation from the in-row lattice matched AlPSi_3 is the use of $(\text{H}_3\text{Si})_3\text{As}$ and $(\text{H}_3\text{Si})_3\text{P}$ for the production films on Si (100). Using $(\text{H}_3\text{Si})_3\text{As}$ as a co-reactant the stoichiometric AlAsSi_3 films have been produced. Due to the larger lattice constant of AlAs relative to AlP , the AlAsSi_3 phase does not grow lattice-matched on the silicon substrate.³⁵ As an attempt to minimize the lattice mismatch mixtures of $(\text{H}_3\text{Si})_3\text{As}$ and $(\text{H}_3\text{Si})_3\text{P}$ were reacted with an Al atomic flux to produce the $\text{AlAs}_{1-x}\text{PxSi}_3$ alloys over the range of $x=0-1$. The synthesis and characterization of these alloys as well as the stoichiometric AlAsSi_3 phase are described in Chapter 6.

Complimentary computational simulations are used to provide insights on the structure of the precursors, reaction intermediates, and solid structures of the materials. While the incorporation of both a $(\text{H}_3\text{Si})_3\text{As}$ and $(\text{H}_3\text{Si})_3\text{P}$ reactants produced alloys with lower lattice constants below that found for AlAsSi_3 , the mismatch between the film and silicon will always exist in alloys due to the large difference between AlAs and silicon lattice constants. The partial substitution of arsenic by phosphorous in these materials somewhat compensates for the increased size of AlAs , but due to the similarity in size with Si it can not compensate completely. As an alternative to phosphorous, nitrogen can be incorporated using $(\text{H}_3\text{Si})_3\text{N}$. The much smaller size of nitrogen can in principle be used to completely compensate for the larger size of AlAs by replacing 18% of the arsenic, yielding a material with the same lattice constant as Si. Chapter 7 details computational simulation data, which provide insight into the reactivities of the reactants and the structure of these materials. These results demonstrate that the growth method can be extended to several and perhaps to most (III-V)-(IV) combinations.

Chapter 2

DIRECT VS. INDIRECT OPTICAL RECOMBINATION IN GERMANIUM FILMS GROWN ON Si SUBSTRATES

Reprinted with permission from “Direct vs. indirect optical recombination in Ge films grown on Si substrates”; G. Grzybowski, R. Roucka, J. Mathews, L. Jiang, R. T. Beeler, J. Kouvetakis, and J. Menéndez, Physical Review B84, 205307 (2011). American Physical Society

Introduction

Germanium has unique optical properties related to the small separation of 0.14 eV between the absolute minimum of the conduction band at the L -point of the Brillouin zone and the Γ -point local minimum. Possible perturbation schemes leading to direct or quasi-direct band gap conditions have been known for a long time. These include n -type doping,³⁷ alloying with Sn,⁵ and the application of tensile strain.¹ Over the past few years these approaches have been contemplated as a possible way to integrate direct gap semiconductors with Si technology, fueling an intense research effort that culminated in the recent announcement of an optically pumped Ge-on-Si laser with emission close to 1550 nm.³⁸

A remarkable feature of most published room temperature luminescence studies of Ge-on-Si films is the dominance of direct gap emission from the Γ -point local minimum in the conduction band to the absolute maximum of the valence band at the same $k = 0$ wave vector.^{6,7,19,39-43} This is in sharp contrast with similar experiments on bulk Ge samples,⁴⁴ for which indirect gap emission from the L -minimum is much stronger. In this chapter, is presented a combined experimental and theoretical study

focused on explaining this discrepancy. It is argued that the difference between films and bulk arises from self-absorption effects, which are far more important in the bulk case, and—in the case of undoped films—from a deviation from quasi-equilibrium conditions in the presence of strong non-radiative recombination at the film-substrate interface. Presented here is an explicit model that accounts for this effect. This peculiar behavior is the result of the unique properties of Ge, which has a direct gap slightly above the indirect edge and a carrier diffusion length of almost macroscopic dimensions.

Experiment

Sn-doped Ge-on-Si samples grown by a novel CVD approach recently introduced by Beeler and co-workers were studied.⁴⁵ This method is an extrapolation—to ultra-low Sn concentrations—of the growth procedure introduced by Bauer and co-workers to synthesize $\text{Ge}_{1-y}\text{Sn}_y$ alloys.⁹ Briefly, the growth is conducted on high resistivity Si(100) wafers via reactions of digermane (Ge_2H_6) and deuterated stannane (SnD_4) diluted in H_2 . Films with thicknesses up to several microns are commonly produced at high growth rates approaching 30 nm/min via reactions of Ge_2H_6 with appropriate amounts of SnD_4 at $T=380\text{-}400$ °C. The incorporation of dopant levels of substitutional Sn into the Ge-on-Si films at nominal levels of 0.03-0.15% is sufficient to suppress the traditional layer-plus-island growth mode (Stranski-Krastanov). The resultant layers are found to exhibit flat surfaces, relaxed strain states, and crystallinity/morphology comparable to those observed in the intrinsic materials, as evidenced by a range of analytical methods including Rutherford Backscattering, Atomic Force Microscopy, high resolution x-ray Diffraction, Secondary Ion Mass Spectrometry and Cross-sectional Transmission Electron Microscopy. The films can be systematically co-doped with P and B atoms at controlled levels of up to 5×10^{19} / cm^3 in situ using the single-sources $\text{P}(\text{GeH}_3)_3$ and B_2H_6 . This process produces tunable and highly controlled atomic profiles of the

donor/acceptor atoms by judiciously adjusting the $P(\text{GeH}_3)_3/\text{Ge}_2\text{H}_6$ or $\text{B}_2\text{H}_6/\text{Ge}_2\text{H}_6$ ratio in the reaction mixture.

Photoluminescence (PL) was measured using a 980 nm laser focused to a ~ 100 μm spot on samples with thicknesses on the order of $1\mu\text{m}$. The average incident power was 200 mW. The emitted light was analyzed with an $f = 320$ mm spectrometer equipped with a 600 lines/mm grating blazed at 2 μm , and collected with a single-channel, LN_2 -cooled extended InGaAs detector that covers the 1.3-2.3 μm range, well above and below the entire spectral range of Ge-like emission.

Results and discussion

Figure 1 shows the PL signal from a Sn-doped Ge film on Si. The as-grown sample shows no measurable PL, but after rapid thermal annealing (RTA) at 680°C (which improves crystallinity, as seen from the narrowing of the x-ray diffraction peaks), followed by a heat treatment under hydrogen, as described in Ref.6, the signal is maximized. The RTA treatment causes a tensile strain due to the thermal expansion mismatch with the Si substrate. In the case of the sample in Fig. 1, the strain was measured by analyzing x-ray reciprocal space maps, obtaining $\varepsilon = 0.24\%$. The main emission feature is assigned to the direct gap E_0 . The shoulder at lower energies corresponds to indirect gap emission. The PL spectrum is virtually identical to that from a pure Ge film on Si (not shown) grown by the method introduced by Wistey *et al* (Ref. 46). This confirms that the extremely small amount of Sn in the film does not change the optical properties in any measurable way. Accordingly, from this point forward the films will be referred to as Ge-on-Si, ignoring the small residual Sn concentration.

It seems natural to compare the film PL with bulk Ge emission. However, this comparison must be done with care because the PL spectrum from bulk Ge is severely distorted by self-absorption effects. With an ambipolar diffusion constant of $D = 65$

cm^2s^{-1} (Ref. 47) and a recombination lifetime of $\tau = 30 \mu\text{s}$ (Ref. 48), the diffusion length of electron-hole pairs in Ge exceeds 0.4 mm, so that reabsorption cannot be neglected, and since the absorption coefficient is higher for 0.8 eV than for 0.7 eV photons, the observed direct gap PL is preferentially suppressed.

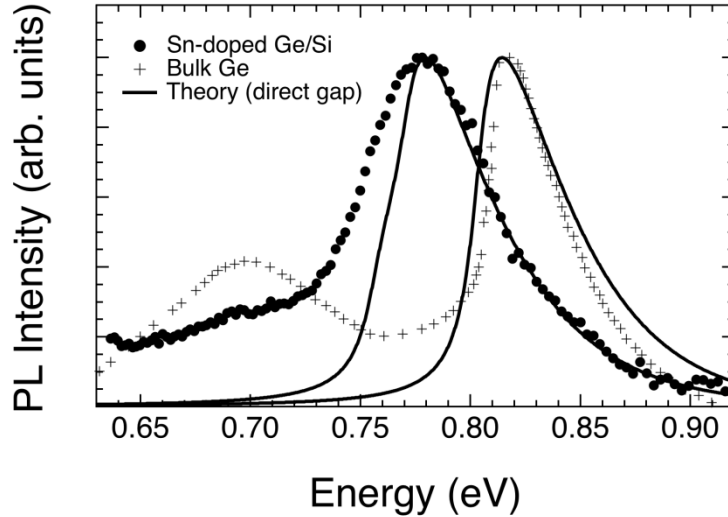


Figure 1 Room temperature photo-luminescence spectrum of a Ge-on-Si film compared with the corresponding spectrum from bulk Ge after self-absorption corrections (Ref. 47). The maximum is assigned to direct gap emission. The weaker feature at lower energy corresponds to indirect gap emission. The spectra are normalized to the same peak intensity. The solid lines are theoretical fits to the direct gap emission, as discussed in the text.

By performing experiments on thin specimens in a transmission geometry with lamp illumination, for which reabsorption can be easily computed, Haynes⁴⁹ generated a "corrected" emission spectrum for bulk Ge, which is shown as crosses in Fig. 1. This corrected spectrum shows clear peaks corresponding to direct and indirect transitions, with the direct gap emission being the strongest one. Since the Ge-on-Si films have thicknesses on the order of 1 μm , self-absorption corrections are much less important and the corresponding spectra should be compared with the "corrected" one from bulk Ge. Thus the dominance of the direct gap emission in the Ge films is to be expected.

To understand the spectral lineshape and relative shifts, the direct gap emission was modeled using a generalized van Roosbroeck-Shockley expression according to which the emission rate at photon energy E (in units of $\text{s}^{-1} \text{cm}^{-3} \text{eV}^{-1}$) is given by⁵⁰

$$R(E) = \left(\frac{n^2 E^2}{\pi^2 \hbar^3 c^2} \right) \alpha(E) \frac{1}{\exp \left[\frac{E - (E_{Fc} - E_{Fv})}{k_B T} \right]} \quad (1)$$

Here n is the index of refraction, E_{Fc} (E_{Fv}) is the quasi-Fermi level for the conduction (valence) bands, and $\alpha(E)$ is the absorption coefficient at temperature T . The absorption can be written as $\alpha(E) = \alpha_0(E)[f_v(E) - f_c(E)]$, where $\alpha_0(E)$ is the absorption coefficient for empty conduction bands and full valence bands. This factorization is valid for parabolic bands, for which the Fermi functions $f_v(E) = \frac{1}{\{1 + \exp[(E_v(E) - E_{Fv})/k_B T]\}}$ and $f_c(E) = \frac{1}{\{1 + \exp[(E_c(E) - E_{Fc})/k_B T]\}}$ give the occupation probability for the valence band state of energy E_v and the conduction band state of energy E_c such that $E_c - E_v = E$. In all of these expressions the standard notation for fundamental physical constants are used. For the function $\alpha_0(E)$ I developed an analytical model, discussed in full detail in the appendix of Ref. 16, which reproduces the experimental absorption curve over a range of up 0.1 eV above the direct band gap based on standard band structure parameters, without introducing any additional parameter to adjust for the absorption strength. As explained in Ref. 16, including excitonic effects is critical to obtain this agreement. The advantage of using a realistic analytical absorption model—as opposed to the experimental absorption coefficient—is that the effect of temperature and strain can be easily introduced. For the temperature (T) dependence of the Ge direct band gap an expression of the form $E_0 = E_0(0) - \frac{\alpha T^2}{T + \beta}$ is used, with $E_0(0) = 0.891$ eV, $\alpha = 5.82 \times 10^{-4}$ eV/K, and $\beta = 296$ K, which reproduces very well the literature data and in

measurements of the direct band gap on the system used here. For the strain calculations the deformation potentials given in Ref. 16 were used. While the calculated absorption is limited to the direct band gap only, the conduction band minima at the L points are fully taken into account for the computation of E_{Fc} . The density of states for the L valley is computed using a longitudinal effective mass $m_l = 1.58m_0$, (Ref. 51) where m_0 is the electron's free mass, and a transverse effective mass m_t obtained from a standard $k \cdot p$ expression with a momentum matrix element $P = 12.6$ eV, which gives $m_t = 0.080m_0$ for pure Ge at 300K. The calculated relative populations n_Γ/n_L of the two conduction band valleys, of importance for the subsequent discussion, is shown in Fig. 2 as a function of the total electron population.

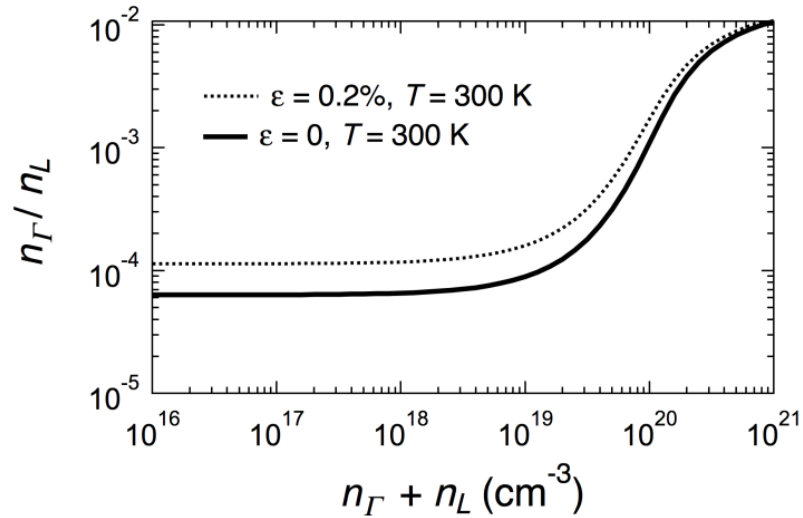


Figure 2 Population ratio for the Γ and L valleys in the conduction band of Ge as a function of the total electron density in the conduction band. The calculations are shown for relaxed Ge ($\epsilon = 0$) as well as for Ge with a biaxial tensile strain in the (001) plane ($\epsilon = 0.2\%$)

Calculated emission profiles using Eq. 1 are shown as solid lines in Fig. 1. For the bulk Ge case, good agreement in peak position and overall lineshape are found assuming that the sample temperature is $T = 290$ K and the photoexcited electron density is less than $1 \times 10^{18} \text{ cm}^{-3}$. The residual disagreement between theory and experiment may be due

to systematic errors in the self-absorption correction, caused mainly by the fact that the absorption coefficient of Ge in this spectral range is very strongly dependent on temperature.⁵² For the Ge-on-Si sample, the emission is calculated using the measured tensile strain of 0.24% and a sample temperature of 320 K. The tensile strain explains 80% of the red shift with respect to bulk Ge, whereas the higher sample temperature, which is expected for laser excitation, accounts the remaining 20%.

Most prior experimental work on light emission from Ge-on-Si films is based on standard Ge or InGaAs detectors with excellent noise-equivalent (NEP) power characteristics but with cut-offs near 0.7 eV, which make it very difficult to measure indirect gap PL. More recently, however, researchers using extended range detectors comparable to the one used here have noticed an enhancement of the intensity ratio $I_{\text{dir}}/I_{\text{ind}}$ between direct and indirect emission in Ge-on-Si films relative to bulk Ge uncorrected for self-absorption.⁴²⁻⁴⁴ $\text{Ge}_{1-y}\text{Sn}_y$ films on Si also show a similar trend.^{6,19} These relative intensity changes have been attributed to the presence of defects, but the analysis above indicates that the self-absorption correction removes—at least in part—the discrepancy between bulk and thin-film Ge. Moreover, any model that invokes defects must provide a mechanism by which the population ratio n_{Γ}/n_L changes, since this ratio determines the relative intensity $I_{\text{dir}}/I_{\text{ind}}$.⁵³ This is far from obvious. If quasi-equilibrium conditions prevail in the conduction band, *i.e.* if there is a common conduction band quasi-Fermi level E_{F_c} , the n_{Γ}/n_L ratio depends only on the temperature, the energy separation between the two valleys, and their corresponding density of states. The enhancement of non-radiative recombination via defects reduces the steady-state photoexcitation level $n_{\Gamma}+n_L$, but, as seen in Fig. 2, the ratio n_{Γ}/n_L is insensitive to $n_{\Gamma}+n_L$ up to levels close to $1 \times 10^{19} \text{ cm}^{-3}$, much higher than can be achieved by photoexcitation. Moreover, from Fig. 2 it is apparent that a decrease in $n_{\Gamma}+n_L$ would lead to a decrease in

n_{Γ}/n_L and thus to a *decrease*, not an increase, in $I_{\text{dir}}/I_{\text{ind}}$. One might also expect a decrease in $I_{\text{dir}}/I_{\text{ind}}$ if defects relax the crystal momentum conservation rules and enhance the no-phonon indirect recombination. Jan *et al.* argue that the presence of defects lead to a spread of trap levels in momentum space that enhances the non-radiative recombination from the indirect edge,⁴² but it is not obvious how $I_{\text{dir}}/I_{\text{ind}}$ might change if quasi-equilibrium is preserved. It appears that any model based on defects should involve a change in the density of states (which would require exceptionally high defect densities) or a deviation from quasi-equilibrium conditions.

If defects don't play an important role in determining the relative intensities of direct and indirect emission, the $I_{\text{dir}}/I_{\text{ind}}$ ratios in Fig. 1 should be explained based on the valley population ratios in Fig. 2. Approximate values are obtained for $I_{\text{dir}}/I_{\text{ind}}$ by fitting the data with simple empirical expressions that appear in commercial data analysis packages. For the direct emission exponentially modified Gaussians were used,⁵⁴ which fit the theoretical profiles in Fig. 1 remarkably well, and for the indirect emission a simple Gaussian is used. The width of the Gaussian is fit to the bulk data of Haynes⁴⁹ and kept fixed for subsequent fits of all samples, a reasonable assumption because the width of the indirect gap emission is essentially given by phonon energies which are expected to change very little in Ge films relative to bulk Ge. Under these conditions, using the peak areas, $I_{\text{dir}}/I_{\text{ind}} \sim 1.3 \pm 0.2$ is obtained for bulk Ge and $I_{\text{dir}}/I_{\text{ind}} = 7 \pm 2$ for the Ge-on-Si film in Fig. 1, the large errors arising from the different results obtained by assuming alternative expressions for the spectral background. The higher sample temperature and tensile strain in the Ge-on-Si sample enhances its n_{Γ}/n_L ratio with respect to the bulk sample, as seen in Fig. 2. A theoretical enhancement factor of 2.9 is computed, which is less than the experimental enhancement $7/1.3 = 5.4$. This suggests that an additional contribution may be needed to explain the high $I_{\text{dir}}/I_{\text{ind}}$ ratio in the Ge-on-Si sample.

To investigate the $I_{\text{dir}}/I_{\text{ind}}$ ratio in more detail PL experiments have been carried out in doped n -type Ge films. The rationale behind these experiments is that for doping levels close to 10^{19} cm^{-3} the n_{Γ}/n_L population ratio should be determined by standard equilibrium conditions between the two valleys and not by the photoexcitation process. Therefore, if photoexcited *intrinsic* films somehow deviate from quasi-equilibrium, their doped counterparts should exhibit quite different $I_{\text{dir}}/I_{\text{ind}}$ ratios. The experimental result is shown as solid circles in Fig. 3 for a 1200 nm-thick Ge-on-Si film with a doping concentration of $1.9 \times 10^{19} \text{ cm}^{-3}$ and vanishing $\varepsilon = 0.05\%$.

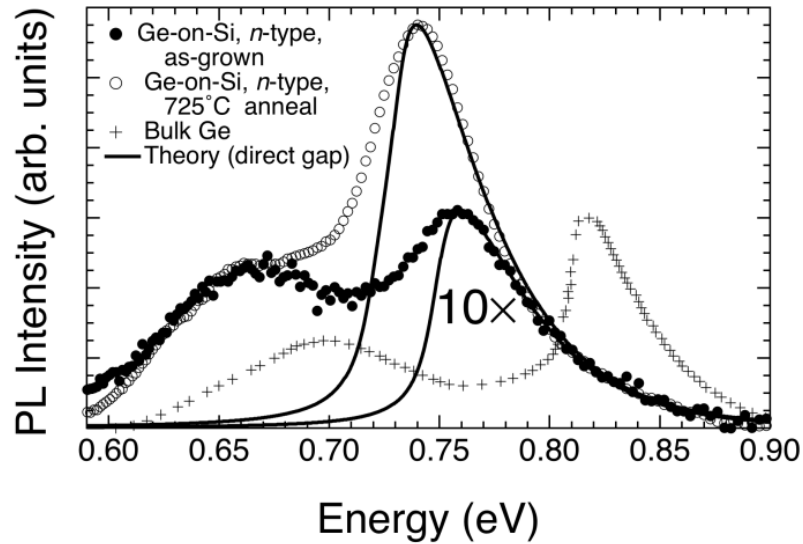


Figure 3: Room temperature PL spectrum of a fully relaxed, n -type Ge-on-Si film with thickness of 1200 nm and carrier density of $\sim 1.9 \times 10^{19} / \text{cm}^3$, as grown (solid circles) and annealed at 725 °C (empty circles). Bulk Ge emission from Haynes (Ref. 49) is shown as crosses. The solid lines are fits with Eq. (1). The bulk Ge spectrum has been normalized to the same maximum intensity as that from the as-grown Ge-on-Si sample.

This low level of strain is possible because the RTA step can be omitted due to the PL enhancement associated with doping. Quite remarkably, the PL spectrum lineshape now looks much more similar to the emission from bulk Ge, which is also reproduced for convenience in Fig. 3. In spite of the vanishing strain there is still a significant shift between the two spectra, which can be explained in terms of band gap

renormalization induced by doping. This is discussed in detail in a later section. It does not affect the analysis in this section because doping shifts the conduction band rigidly.⁵⁵ The $I_{\text{dir}}/I_{\text{ind}}$ for the doped Ge-on-Si sample is 1.7 ± 0.3 , clearly much less than the ratio $I_{\text{dir}}/I_{\text{ind}} = 7 \pm 2$ observed in Fig. 1, even though a calculation based on Fig. 2 predicts that the difference between the two ratios should not exceed 25%. Next the sample was RTA-treated to 725 °C and its post-annealing PL spectrum is shown as empty circles in Fig. 3. The overall intensity increases by a factor of 20, which correlates with a large reduction in the full width at half maximum of the x-ray diffraction peak, from 0.48° (as grown) to 0.061° (725 °C). This suggests that the improved PL is due to a reduced non-radiative recombination rate, and explains the failure to observe PL in undoped, unannealed samples. On the other hand, the $I_{\text{dir}}/I_{\text{ind}}$ ratio only increases by 50% to 2.6 ± 0.3 after annealing. This can be explained in terms of the 0.18% tensile strain induced by the annealing process, which leads to a predicted increase of 45% in the n_{Γ}/n_L ratio, in good agreement with the experimental results.

The conclusion from the above experiments is that the results from doped Ge-on-Si films can be understood in terms of quasi-equilibrium conditions in the conduction band. Consistent with this model, the elimination of defects via annealing changes the overall intensity dramatically, but the $I_{\text{dir}}/I_{\text{ind}}$ only changes according to the quasi-equilibrium model following the strain induced by the annealing process. On the other hand, the $I_{\text{dir}}/I_{\text{ind}}$ ratio in intrinsic, undoped Ge-on-Si films is too large compared with bulk Ge and with doped Ge-on-Si films, suggesting that in this case there is an additional mechanism that affects this ratio. As mentioned above, the presence of defects can only be invoked if a mechanism can be identified that generates a departure from quasi-equilibrium in the conduction band. A model that meets this requirement is discussed in the next section.

Non-equilibrium model

The foregoing discussion suggests that quasi-equilibrium conditions may not prevail in the conduction band of photoexcited intrinsic Ge-on-Si films. Presented here is a very simple toy model that provides a mechanism for the departure from equilibrium. A system of two interacting states is considered, representing the Γ - and L valleys. It is assumed that electrons are being pumped into the Γ -valley at a rate of G electrons/s. This is the case in Ge under 980 nm laser excitation. The excited electrons will redistribute themselves between the two valleys, and they will also recombine with holes via radiative and non-radiative channels. The simplest rate equations that can be written to represent this situation are:

$$\frac{dn_T}{dt} = G - \left(\frac{1}{\tau_{\Gamma L}} + \frac{1}{\tau_{\Gamma}} \right) n_T + \frac{1}{\tau_{L\Gamma}} n_L, \quad \frac{dn_L}{dt} = - \left(\frac{1}{\tau_{\Gamma L}} + \frac{1}{\tau_L} \right) n_L + \frac{1}{\tau_{L\Gamma}} n_T \quad (2)$$

The transfer rates between the valleys are characterized by the time constants $\tau_{\Gamma L}$ and $\tau_{L\Gamma}$, and the constants τ_{Γ} and τ_L represent the recombination lifetimes for each valley. There is of course an additional coupled equation involving the valence band holes, but at this level of simplicity this equation is not needed for the argument which is about to be made. Eq. (2) is a generalization of a two-state model introduced by Stanton and Bailey to discuss electron dynamics in GaAs and InP.⁵⁶ If the generation and recombination terms are deleted, it is easy to show⁵⁶ that for arbitrary initial occupations the system of equations has asymptotic solutions for $t \rightarrow \infty$ that imply $\frac{n_{\Gamma}(\infty)}{n_L(\infty)} = \frac{\tau_{\Gamma L}}{\tau_{L\Gamma}}$. Since this limit corresponds to quasi-equilibrium, the $\tau_{\Gamma L} / \tau_{L\Gamma}$ ratio must equal the ratio n_{Γ} / n_L computed in Fig. 2, which leads to $\tau_{\Gamma L} / \tau_{L\Gamma} \leq 10^{-4}$ for the total electron concentrations of relevance for this discussion. If the full Eq. (2) is now considered, when steady-state conditions are reached (for example, under illumination with a cw laser) the time derivatives become zero and the following is obtained

$$\frac{n_{\Gamma}}{n_L} = \frac{\tau_{\Gamma L}}{\tau_{L\Gamma}} + \frac{\tau_{\Gamma L}}{\tau_L} \quad (3)$$

Therefore, one can expect deviations from equilibrium if the second term on the right-hand side of Eq. 3 is comparable to or greater than 10^{-4} . Under such circumstances the relative valley populations cannot be computed using a common quasi-Fermi level. The transfer rate $\tau_{\Gamma L}$ in Ge has been measured by time-resolved inelastic light scattering, and its value is $\tau_{\Gamma L} = 1.2$ ps.⁵⁷ On the other hand, the recombination time τ_L can be associated with the minority carrier lifetime, which in bulk Ge is about $30 \mu\text{s}$.⁴⁸ Thus for bulk Ge $\tau_{\Gamma L} / \tau_L$ is 4×10^{-8} , and the second term in Eq. (3) is much smaller than the first term. In other words, deviations from quasi-thermal equilibrium in bulk Ge are negligible, and the PL spectrum can be calculated by assuming a unique quasi-Fermi level for the conduction band.

The situation is very different in Ge-on-Si materials due to the presence of a surface and an interface. The recombination velocity s at a bare Ge surface is about 140 cm/s.⁵⁸ On the other hand, the interface recombination velocity at a dislocated Si-Ge interface can be as high as $s = 4000$ cm/s.⁵⁹ Using this value for a film thickness $W = 1 \mu\text{m}$, the effective lifetime becomes $\tau_L = W/2s = 12$ ns, so that $\tau_{\Gamma L} / \tau_L = 10^{-4}$ and the second term in Eq. (3) is no longer negligible. For this particular value of $\tau_{\Gamma L} / \tau_L$, the ratio n_{Γ}/n_L would be doubled relative to the quasi-equilibrium prediction, and the $I_{\text{dir}}/I_{\text{ind}}$ PL ratio would be enhanced proportionally. (Of course, both n_{Γ} and n_L decrease in absolute terms for shorter recombination lifetimes, so that the overall PL intensity is reduced, as also observed experimentally). Interestingly, from studies of $\text{Ge}_{1-y}\text{Sn}_y$ devices with a thickness $W = 300$ nm recombination lifetimes approaching 5 ns⁶⁰ are found, very close to my estimates based on interface recombination velocities. In Fig. 4 PL spectra from three different p -type samples are shown. These samples have comparable total thicknesses

but different doping profiles. Sample A is highly doped ($p = 1 \times 10^{19} \text{ cm}^{-3}$), whereas sample B has much lower doping ($p = 1 \times 10^{18} \text{ cm}^{-3}$).

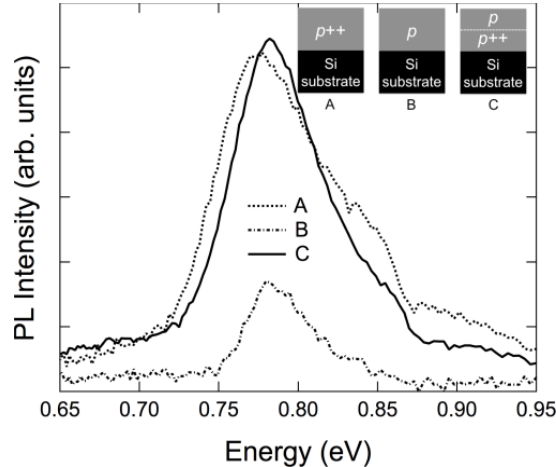


Figure 4: Room temperature PL intensity from p -type Ge-on-Si samples. Doping concentrations are $p++ = 1 \times 10^{19} \text{ cm}^{-3}$ (Sample A and C), $p = 1 \times 10^{18} \text{ cm}^{-3}$ (sample B) and $p = 1 \times 10^{17} \text{ cm}^{-3}$ (Sample C). Thicknesses are 830 nm (Sample A), 730 nm (Sample B) and 960 nm (Sample C). In sample C the $p++$ and p layers have equal thickness. All samples were subjected to three cycles of post-growth RTA at 680 °C (10 sec each).

The integrated PL intensity of sample B is six times weaker than that of sample A, in reasonable agreement with the doping concentrations. Sample C is a back-surface-field (BSF) type of structure, in which the bottom half of the Ge layer is highly doped ($p = 1 \times 10^{19} \text{ cm}^{-3}$) and the top half is verylightly doped ($p = 1 \times 10^{17} \text{ cm}^{-3}$). Accordingly, emission from the top layer should be much weaker than that of sample B, and emission from the bottom layer should be significantly weaker than that of sample A because this layer is thinner and it is located $\sim 500 \text{ nm}$ below the surface. However, the PL from sample C is strong, and that the peak energy is higher than that of sample A. This suggests that most of the emission actually originates from the top layer, where band gap renormalization due to doping should be negligible. This higher than expected emission from the top layer is associated with the built-in potential in the BSF structure, which repels the photoexcited electrons in the lightly doped layer away from the Si interface.

This behavior is consistent with the above suggestion that defects at the Si interface are the main cause of non-radiative recombination in these structures.

Notice that the $I_{\text{dir}}/I_{\text{ind}}$ ratios in the p -doped samples are very high, to the point that the indirect gap signal is difficult to quantify. This is qualitatively consistent with the above analysis, since only in n -type samples we would expect ratios approaching the equilibrium conditions depicted in Fig. 2. However, a quantitative comparison of $I_{\text{dir}}/I_{\text{ind}}$ ratios between n -type and p -type Ge-on-Si layers may not be straightforward, since even in highly doped p -type bulk Ge Wagner and Viña observed a laser wavelength dependence of the $I_{\text{dir}}/I_{\text{ind}}$ ratios.⁶¹ In the Wagner-Viña experiment these ratios were found to increase as the electrons become preferentially pumped into the Γ valley, the situation mimicked by Eq.(2). Thus the simple model may explain the experimental observations not only in Ge-on-Si materials but also on very highly doped p -type bulk material. In this latter case there are no interfaces with high recombination rates, so that the dominant non-radiative recombination mechanism should be associated with defects induced by the heavy doping.

Band gap renormalization

As briefly hinted above, the emission maximum of the as-grown doped Ge-on-Si film in Fig. 3 (dark circles) is expected to be much closer to that of bulk Ge than the PL maximum of the intrinsic, tensile strained quasi-Ge sample in Fig. 1. Surprisingly, the opposite is true. The emission maximum in the doped quasi-Ge sample is located at 0.755 eV, whereas the emission maximum for the intrinsic quasi-Ge sample in Fig. 1 appears at 0.778 eV. A possible explanation is that the presence of dopant atoms shifts the absorption edges in Ge, as has been shown in absorption measurements, where a clear redshift is detected.⁵⁵ Recent PL work on P -doped Ge also shows a redshift as a function of the P concentration, although its quantification is difficult because the PL

maximum is near the cutoff wavelength of the detector used by these workers.⁶² On the other hand, PL experiments using doped Ge-on-Si films show no such shift.³⁹ The redshift cannot be explained in terms of poor crystallinity, since the peak shifts further to lower energies upon annealing, as seen in Fig. 3 (white circles). To quantify this effect an adjustable rigid energy shift of the absorption coefficient is allowed. The fit redshifts are then 40 meV for the doped, as grown sample in Fig. 3 and 47 meV for the same sample annealed at 725 °C. These are close to the redshift of 37 meV in the direct gap absorption observed by Haas for a P-doped Ge sample at a level of $1.95 \times 10^{19} \text{ cm}^{-3}$.⁵⁵ To confirm this correlation additional PL experiments in samples with different doping levels were carried out. The results are shown in Fig. 5.

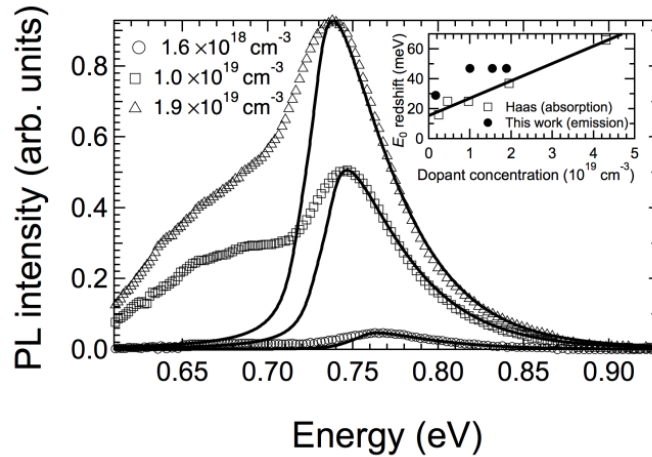


Figure 5: Room temperature photoluminescence spectrum from Ge-on-Si films with different P doping concentrations. The solid lines are theoretical fits to the direct-gap emission. The inset shows the redshift needed to adjust the spectra, compared with absorption measurements of the direct gap renormalization induced by P impurities in Ge. (Ref. 41).

The overall intensity and the $I_{\text{dir}}/I_{\text{ind}}$ ratio increase as a function of the doping concentration, as expected from the above models and reported earlier.⁴¹ In the inset shifts measured by Haas⁶⁶ were compared with the shifts determined from my fits. They seem to follow a similar trend, with the emission shifts higher by about 10 meV relative

to the absorption shifts, which may reflect a systematic error associated with the two different methods of band gap determination. It is understood that these results provide a strong indication that the redshifts observed in the samples used here are indeed caused by the dopant atoms and that the same mechanism is responsible for the shift in emission and absorption energies.

It is important to emphasize that band gap renormalization effects are not limited to the band minima where the donor electrons happen to reside. The shifts are caused by the perturbation associated with the presence of foreign atoms,⁶³ which changes the entire band structure. In Haas' absorption experiments, the indirect edge is seen to redshift by the same amount as the direct edge.⁵⁵ This is a non-trivial result which implies that the n_T/n_L ratio is not affected by renormalization effects, justifying the comparison above of I_{dir}/I_{ind} ratios in doped and undoped samples. In the PL experiments, however, the separation between the direct and indirect maxima decreases from 118 meV in the bulk case to 99 meV in the doped quasi-Ge sample. This is not thought to be inconsistent with a rigid shift of the two edges because the lineshape of the indirect gap emission may be affected by the presence of impurities.

Conclusion

In summary, the new experimental data presented here and the associated analysis indicate that the dominance of direct gap emission in Ge-on-Si films is due to two different effects. In all Ge-on-Si thin films, the lack of significant self absorption effects enhances the relative intensity of the direct gap emission in the experimental spectra. In *n*-doped Ge-on-Si films there is no evidence for any other contribution to the enhancement of direct gap emission. In intrinsic or *p*-type Ge-on-Si films, where the electron population in the conduction band is produced by photoexcitation, there appears to be an additional enhancement of the direct gap emission relative to the

indirect gap emission that suggests a departure from quasi-equilibrium conditions. A model is proposed to account for this departure in terms of a much shorter recombination lifetime than in bulk Ge. The $I_{\text{dir}}/I_{\text{ind}}$ ratio in intrinsic and p -type materials then becomes a useful figure of merit to assess the quality of the material for possible laser applications.

Chapter 3

PHOTOLUMINESCENCE FROM HEAVILY DOPED GESN:P MATERIALS GROWN ON SI(100)

Reprinted with permission from “Photoluminescence from heavily doped GeSn:P materials grown on Si(100)”; G. Grzybowski, L. Jiang, J. Mathews, R. Roucka, C. Xu, R. T. Beeler, J. Kouvetakis, and J. Menéndez, *Applied Physical Letters* 99, 171910 (2011) American Institute of Physics

Introduction

Ge-based group IV semiconductors are currently receiving renewed attention due to potential applications in Si-based photonics.⁶⁴ A significant enhancement in direct light emission, achieved in tensile-strained *n*-type Ge systems, has been extensively reported.^{7,8} The tensile strain reduces the separation between the Γ and L valleys in the conduction band of Ge, and the addition of electrons in the conduction band shifts the Fermi level toward the higher Γ -minimum, substantially increasing direct gap light emission. A technologically important way to apply tensile strain to Ge is to grow Ge films on Si substrates at high temperatures (~ 800 °C) and take advantage of the thermal expansivity mismatch between the two materials, which induces tensile strain on the Ge film upon cooling to room temperature. This property has been crucial for the recent breakthrough development of an optically pumped Ge-on-Si laser that uses tensile strain and heavy *n*-type doping to achieve a "quasi-direct" band gap condition in the Ge active component.³⁸ However, the band gap engineering underlying this technology is limited by the maximum strain achievable, which in this case cannot theoretically exceed 0.30

% . Higher strains that are tunable over a wide range have been produced by growing Ge on $\text{Ga}_{1-x}\text{In}_x\text{As}$ with larger lattice constants.⁶⁵⁻⁶⁷

An alternative approach to enhance direct gap emission in Ge-like materials is to alloy Ge with Sn.⁶⁸ The addition of Sn reduces the Γ -L valley separation and lowers the direct band gap, thereby providing emission wavelength tunability.² Based on experimental and theoretical data, it has been estimated that 1% Sn in Ge is approximately equivalent to a tensile strain of 0.35%, and corresponds to a sharp reduction in band gap energy.⁶ Very recently, binary $\text{Ge}_{1-y}\text{Sn}_y$ alloys ($y \leq 0.04$), grown on Si(100) by chemical vapor deposition of Ge_2H_6 and SnD_4 precursors, were shown to display tunable photoluminescence comparable to that of Ge on Si.⁶ In addition, direct gap electroluminescence has been observed in Si/ $\text{Ge}_{1-y}\text{Sn}_y$ heterostructure *pin* photodiodes.¹⁹ In this chapter, a study of the optical emission from *n*-type doped $\text{Ge}_{1-y}\text{Sn}_y$ alloys is presented. These materials are of great interest as the potential $\text{Ge}_{1-y}\text{Sn}_y$ analogs of the recently introduced Ge laser.

Results and discussion

The photoluminescence (PL) studies of *n*-type $\text{Ge}_{1-y}\text{Sn}_y$ alloys were conducted on samples with $0 < y < 0.036$ and thicknesses between 400 nm and 900 nm. They were grown at 320-385°C directly on high resistivity Si(100) using low pressure Chemical Vapor Deposition (CVD) reactions of SnD_4 and Ge_2H_6 .⁶ All materials were doped *in situ* using the single-source precursor $\text{P}(\text{GeH}_3)_3$, which is known to deliver fully activated P atoms at low growth temperatures under metastable conditions.¹¹ The donor carrier concentrations were found to be in the $2\text{-}6 \times 10^{19} \text{ cm}^{-3}$ range from Hall effect and infrared ellipsometry measurements. Secondary Ion Mass Spectrometry (SIMS) depth profiles revealed a uniform distribution of the P atoms throughout the layer. The P content was quantified using an implanted Ge standard, and the results indicate that,

within error, all P donors are activated before any post-growth thermal treatment. The Sn content and thickness of all films were measured by Rutherford Backscattering (RBS), which was also employed to investigate the degree of crystallinity and epitaxial registry of the layer using block ion channeling experiments. The ratio of the aligned and random peak heights was found to be identical in both the Sn and Ge signals of the spectrum, indicating full substitutionality of the constituent atoms in the lattice. High-resolution x-ray diffraction (HRXRD) reciprocal space maps of the as-grown materials revealed a residual compressive strain in the $\sim 0.20\%$ range. The full width at half maximum (FWHM) of the 004 rocking curve was relatively broad at 0.7° , indicating a non-negligible mosaic spread. The crystallinity is dramatically improved by a post-growth rapid thermal annealing (RTA) treatment described below. The relaxed lattice parameter is obtained from the HRXRD data and compared with the measured compositional dependence in Ref. 69. Very good agreement is found between the compositions determined from RBS and HRXRD.

The PL measurements were conducted at room temperature using a 980 nm laser focused to a $\sim 100 \mu\text{m}$ spot. The power incident on the samples was set to 400 mW. The emitted light was focused onto the entrance slit of an $f=320\text{mm}$ spectrometer that was equipped with a diffraction grating blazed at 2000 nm. The diffracted light was collected by a liquid-nitrogen cooled extended InGaAs detector. The PL signal contained a narrow contribution at 1950 nm corresponding to the laser line observed in second-order. This peak was fitted with a Gaussian profile and subtracted from the spectra for clarity of the presentation. PL spectra for representative samples are shown in Fig. 6. All spectra display a dominant high-energy peak and a lower-energy shoulder. They are assigned to emission from the direct and indirect gap, respectively. The solid lines show fits in which the indirect emission is modeled as a Gaussian peak with a fixed FWHM of 67 meV, the

value obtained from fitting the bulk Ge data from Ref. 49. The direct emission is modeled as an exponentially modified Gaussian curve⁵⁴(EMG) to account for the temperature-dependent high-energy tail. The EMG component is then fit with a theoretical expression for direct gap emission,¹⁹ based on a generalized Van Roosbroeck-Shockley expression that uses a realistic model for the direct gap absorption,¹⁶ including strain and excitonic effects. The model computes the direct gap emission only, but the L valleys associated with indirect emission are fully taken into account for the calculation of quasi-Fermi levels. Thus, changes in the relative intensity of direct and indirect emission (proportional to the ratio n_{Γ}/n_L between the electron concentrations at the Γ and L valleys) can also be predicted.

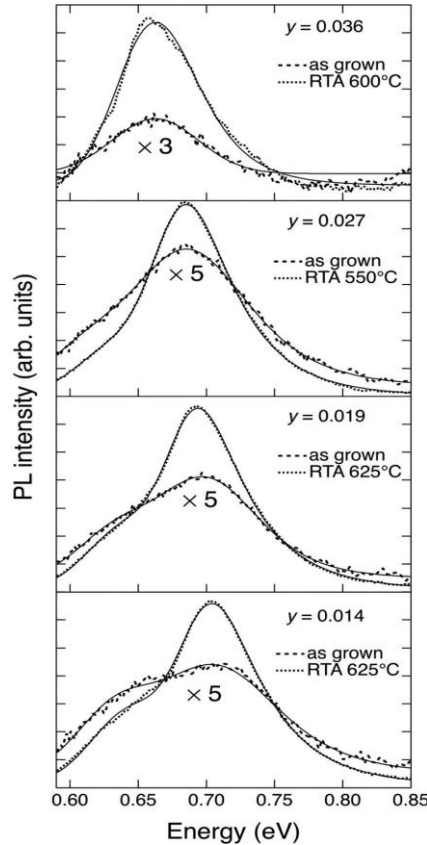


Figure 6. Room temperature PL signal of n-type $\text{Ge}_{1-y}\text{Sn}_y$ samples as-grown and after rapid thermal annealing. The solid lines show fits with expressions describing direct- and indirect-gap emissions.

It is apparent from a simple inspection of Fig. 6 that there is a progressive red shift of the PL as the Sn concentration is increased, as expected from prior work on undoped material.⁶ The observation of PL in as-grown materials is remarkable, since in previous work intrinsic Ge_{1-y}Sn_y/Si(100) layers only yielded measurable emission signals after annealing.⁶ In fact, the PL intensity from my as-grown doped films is of the same order of magnitude as the PL intensity from annealed undoped films. Samples with similar Sn concentrations and layer thickness typically exhibit a significant increase in emission intensity as a function of doping levels from $1-2 \times 10^{19} \text{ cm}^{-3}$ to $6 \times 10^{19} \text{ cm}^{-3}$.

An enhancement of the PL intensity has been reported for doped pure Ge.^{39,62} To further investigate this phenomenon in Ge_{1-y}Sn_y alloys, annealing studies were performed. All samples underwent RTA cycles (typically 3-10s) at temperatures between 625°C and 700°C, with lower temperatures being used on higher Sn-concentration samples. The thermal treatment resulted in a significant improvement of the crystallinity, as evidenced by the narrowing of the 004 rocking curve down to a FWHM of 0.15°. The RTA treatment also induces a change in the nature of the residual strain, from compressive to tensile (~0.1%), and a decrease in the carrier concentrations by a factor of approximately 2. PL results from RTA-treated samples are shown in Fig. 6. In all cases intensity enhancements were observed (integrated areas) by factors between 6 and 10. The changes in direct emission intensity and direct/indirect intensity ratios caused by the changes in strain and carrier concentration have been computed, and it was found that these contributions tend to cancel each other, since the tensile strain increases the relative population of the Γ -valley, whereas a decrease in carrier concentration produces the opposite effect. Thus, the observed increases in PL intensity upon annealing must be due to a reduction in non-radiative recombination rates as a result of the improved crystallinity of the annealed samples. This is strongly supported

by the sharper PL lineshapes: for the as grown samples, the Gaussian broadening of the EMG has a FWHM of about 80 meV, which is reduced to about 50 meV upon annealing.

The PL intensity from doped, annealed samples can now be directly compared with their undoped counterparts. Fig. 7 shows results from similar samples with a Sn concentration $y=0.025$. The doped sample was annealed at 625°C, whereas the undoped material was annealed at 680°C. The PL intensity from the doped sample is about 10 times stronger. From fits of the undoped sample PL with theoretical expressions, It is determined that the steady-state photoexcited hole concentration cannot be higher than 10^{18} cm^{-3} . Using this value, the doped sample intensity is predicted to be 15 times stronger, in reasonable agreement with the observed value. These results thus confirm that n-type doping at the 10^{19} cm^{-3} level and RTA at temperatures near 600°C have a comparable effect in terms of PL intensity enhancement, quantitatively confirming that the observation of PL in asgrown doped samples is directly related to their doping levels.

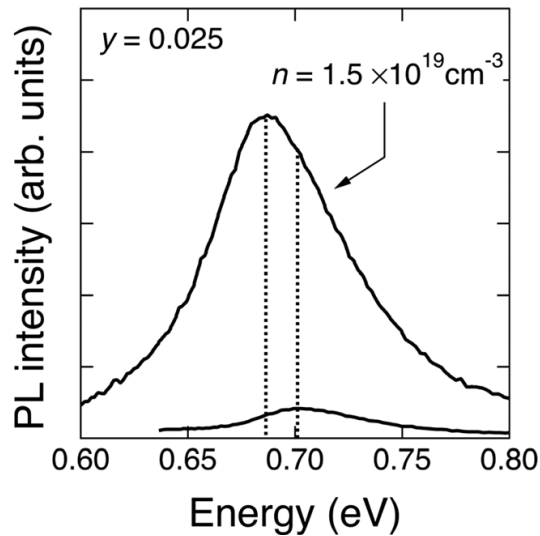


Figure 7. Room temperature PL from annealed $\text{Ge}_{0.975}\text{Sn}_{0.025}$ samples. The weaker signal corresponds to nominally intrinsic material. The relative emission shift is caused by band gap renormalization in the doped sample.

Annealing the Sn-rich samples at $T > 650^\circ\text{C}$ results in a dramatic quenching of the emission intensity and a concomitant shift of the corresponding direct gap to higher energy, suggesting that a significant fraction of the Sn atoms has shifted off their tetrahedral sites. This was confirmed using RBS, which showed that the profile of the aligned signal intensity has uniformly increased to a significant level halfway between that of the as-grown sample and the fully random counterpart. However, the random Sn trace remained constant throughout the layer, indicating no Sn segregation towards the film surface. The chemical environment of the Sn atoms in these “partially decomposed” samples is not fully understood and warrants further investigations. However, preliminary XRD measurement indicates a systematic reduction in the molar volume of the system, which can be explained by an offset of the atoms from the ideal diamond lattice positions.

An interesting byproduct of the study of doped samples is the observation that their emission is systematically redshifted relative to undoped films with the same Sn concentration, as seen in Fig. 7. Theoretical fits of the two samples in this figure give a direct band gap of $E_0 = 0.707$ eV for the undoped sample and $E_0 = 0.684$ eV in the doped one. The relative shifts are comparable to those observed in absorption measurements from doped Ge,⁵⁵ where they are attributed to band gap renormalization. Fig. 8 shows the observed intensity ratios $I_{\text{dir}}/I_{\text{ind}}$ between direct and indirect emission for my annealed doped samples. The lines are proportional to the calculated n_{Γ}/n_L population ratio. Since the RTA temperature is systematically lowered as a function of y , the residual tensile strain is a smoothly decreasing function of y , and this is incorporated into the n_{Γ}/n_L calculation. The dotted line is computed assuming no compositional dependence of the Γ -L separation, and predicts a decreasing $I_{\text{dir}}/I_{\text{ind}}$ as a function of y due to the reduced tensile strain for higher y . The solid line incorporates the decrease in the Γ -L

separation as a function of y and gives better agreement with experiment, confirming that Sn-alloying can be used as an alternative to tensile strain to enhance the direct gap emission in Ge.

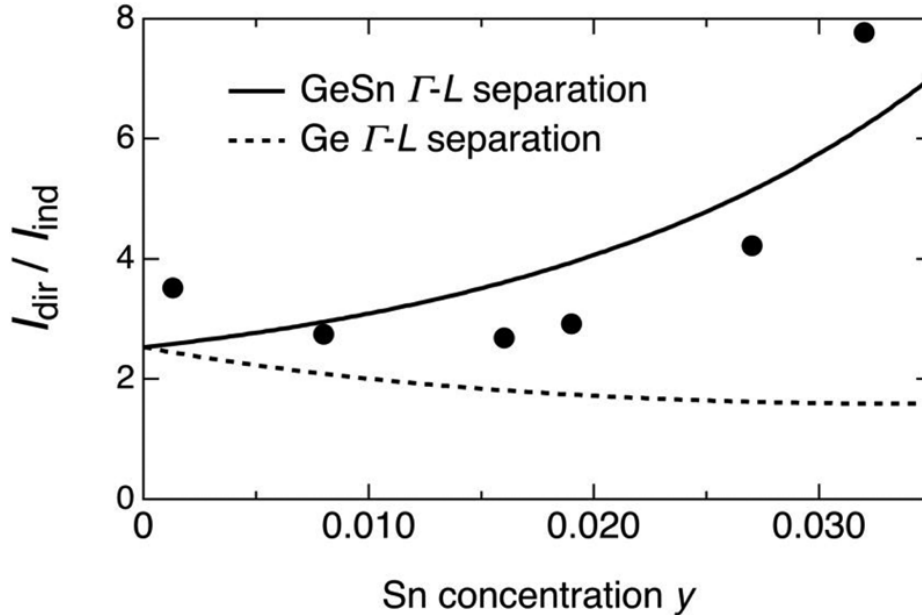


Figure 8. Ratio of direct and indirect emission intensities (from the areas of the peaks used to model the PL in Fig. 1) for annealed doped $\text{Ge}_{1-y}\text{Sn}_y$ samples with doping concentrations near $1.5 \cdot 10^{19}$. The lines show theoretical simulations using either the compositional dependence of the Γ -L separation in $\text{Ge}_{1-y}\text{Sn}_y$ alloys or a fixed value as in pure Ge.

Summary

Strong room temperature photoluminescence in n-type GeSn alloys has been measured. These films are found to be much better light emitters than intrinsic analogs with similar Sn contents. This behavior is explained by the increase in the electron population delivered through doping with P donors. Studies of intensity ratios between direct and indirect emission confirm that alloying with Sn is a viable alternative to tensile strain as a tool to enhance direct gap emission in Ge-like materials.

Chapter 4

NEXT GENERATION GERMANIUM TIN ALLOYS GROWN ON SILICON BY TRIGERMANE WITH TIN CONTENTS OF 1-9%: REACTION KINETICS AND TUNABLE EMISSION

*Reprinted with permission from “Next generation of $Ge_{1-y}Sn_y$ ($y = 0.01-0.09$) alloys grown on Si(100) via Ge_3H_8 and SnD_4 : Reaction kinetics and tunable emission”; G. Grzybowski, R. T. Beeler, L. Jiang, D. J. Smith, J. Kouvetakis, and J. Menéndez, *Applied Physics Letters* 101, 072105 (2012). American Institute of Physics*

Introduction

Ge-Sn alloys have attracted considerable attention after the unraveling of the band structure of α -Sn,⁷⁰ since a linear interpolation between α -Sn and Ge suggested that the alloy should be a direct gap semiconductor over a broad compositional range.⁷¹ Unfortunately, the exploration of this system has been limited by the very low solid solubility of Sn in Ge ($< 1.1\%$),¹¹. This limitation is in sharp contrast with the full miscibility of the Si-Ge system, which has enabled a broad array of technological applications.⁷² The epitaxial growth and stabilization of α -Sn in the early 1980's¹² raised hopes that crystalline $Ge_{1-y}Sn_y$ alloys might also be amenable to epitaxial stabilization on suitable substrates.^{3,73} However, the incompatibility of the α -Sn and Ge growth conditions represented a major obstacle for the synthesis of the alloys. In the case of molecular beam epitaxy (MBE), the growth of α -Sn was optimized at 25 °C,¹² whereas the growth of Ge requires temperatures close to 300 °C.¹³ Not surprisingly, the MBE route to $Ge_{1-y}Sn_y$ alloys has been plagued with difficulties such as Sn-segregation or non-uniform distribution, and it has usually required extreme non-equilibrium conditions.⁷⁴⁻

⁷⁶ On the other hand, the use of Chemical Vapor Deposition (CVD) has also been hampered by the relatively high temperatures ($>350\text{ }^{\circ}\text{C}$)¹⁴ required for growth with germane (GeH_4)—the standard Ge source—and by the lack of molecular Sn sources.

A significant breakthrough in the CVD route to $\text{Ge}_{1-y}\text{Sn}_y$ alloys was achieved with the introduction of a growth method based on reactions of digermane (Ge_2H_6) and PhSnD_3 ($\text{Ph}=\text{C}_6\text{H}_5$, $\text{D} = \text{deuterium}$).¹⁵ This method was simplified a year later with the use of carbon-free deuterated stannane (SnD_4) as the Sn source.⁹ More recently, the SnCl_4 precursor was also used in combination with Ge_2H_6 .^{77,78} The Ge_2H_6 approach has led to the first $\text{Ge}_{1-y}\text{Sn}_y$ diode devices with extended near-IR responsivity,¹⁶⁻¹⁸ as well as to the observation of tunable direct band gap emission.^{6,19} Key to these achievements is the fact that Ge_2H_6 can be used as a Ge precursor at temperatures as low as $300\text{ }^{\circ}\text{C}$, and therefore it is far more compatible than GeH_4 with the low temperatures required to grow GeSn alloys.

Despite these successes the growth of thick layers ($\sim 1\text{ }\mu\text{m}$) with high Sn concentrations on Si substrates remains very challenging. Using the $\text{Ge}_2\text{H}_6/\text{SnD}_4$ precursors, one can grow thick films ($0.5\text{-}1\text{ }\mu\text{m}$) with $y \leq 0.03$ at growth temperatures between $370\text{ }^{\circ}\text{C}$ and $340\text{ }^{\circ}\text{C}$. However, for higher Sn concentrations the temperature must be systematically lowered from $340\text{ }^{\circ}\text{C}$ ($y = 0.03$) to $290\text{ }^{\circ}\text{C}$, ($y = 0.09$) to ensure full substitution of the Sn atoms in the structure. Such temperature reduction results in a concomitant decrease in growth rate, and prevents the film from completely relaxing mismatch strain with the substrate, particularly for samples with $y > 0.04$.⁶⁹ These two factors reduce the overall thickness that can be achieved, ultimately diminishing the device potential of these materials as grown on Si, and precluding the likely observation of photoluminescence (PL), which in films with thicknesses below 500 nm is largely

suppressed by non-radiative recombination at the intrinsically defective Si/GeSn interface.¹⁰

A possible path to improvements over the Ge₂H₆/SnD₄ approach follows from the observation that grown films withstand thermal anneals at temperatures as high as 750 °C,⁷⁹ well above the maximum permissible growth temperature. This suggests that an increase in growth rate should allow the stabilization of films with higher Sn concentrations, while at the same time allowing larger film thicknesses. Very recently, Grzybowski *et al.*,⁸⁰ introduced trigermane (Ge₃H₈) as a Ge CVD precursor with a higher growth rate than Ge₂H₆, and confirmed that this new precursor can be used to grow Ge_{1-y}Sn_y films. In this section, it is demonstrated that the Ge₃H₈-SnD₄ approach provides a unique low temperature route to thick high-quality thick films with significant light emission at all concentrations. These outcomes represent a major advance in the development of this binary alloy as a viable semiconductor system fully integrated with Si technologies.

Results and discussion

Film growth was conducted via Ultra-High Vacuum (UHV) CVD reactions of 2.5 % Ge₃H₈ diluted in high purity H₂ intermixed with SnD₄. The Ge₃H₈ was previously obtained by thermolysis of Ge₂H₆, as described in Ref.⁸⁰ The reactor consists of a resistively heated 3”-diameter quartz tube that is attached to a UHV chamber (see Ref. 79 for design details). The substrates are 2×2” square segments cleaved from a 4” *p*-type Si(100) wafer exhibiting resistivities of 1-10 Ωcm. In a typical run the substrates were chemically treated to remove organic and metallic contaminants from their surface using the conventional RCA process. They were subsequently dipped in 10% HF/methanol solution to etch the native oxide, rinsed by methanol and dried under a flow of ultrahigh purity nitrogen. They were then loaded onto a quartz boat and inserted into the reaction

zone through a load lock under a flow of H₂ carrier gas at 10⁻⁴ Torr pressure, while the reactor was kept at the growth temperature. The H₂ pressure was increased to 0.200 Torr and stabilized over a period of several minutes using a throttle valve. At this time, the SnD₄ and Ge₃H₈ co-reactants were introduced into the H₂ stream through mass flow controllers and allowed to react over the substrate surface.

Under these conditions, films with $y = 0.01-0.06$ were deposited at temperatures ranging between 360°C-325°C, respectively. In this case, the experiments produced layers possessing a thickness up to 600-750 nm with growth rates of 9-10 nm min⁻¹. The higher Sn contents ($y = 0.07-0.09$) samples were grown at 310-300 °C with thicknesses up to 300-450 nm at growth rates near 5 nm min⁻¹. In all cases, the growth rates are increased by 3-4 times compared to those obtained using Ge₂H₆ under similar pressure and temperature conditions. Doped samples ($n=1-2 \times 10^{19}/\text{cm}^{-3}$) were also produced using previously developed methods based on the single-source P(GeH₃)₃. The materials properties were found to be comparable to those of the corresponding intrinsic analogs, as discussed below.

Figure 9 shows the Sn/Ge ratio in the films, r_{film} , versus the corresponding ratios in the gas phase, r_{gas} , for Ge₃H₈ and for previously reported Ge₂H₆ reactions. If the Ge and Sn incorporation were both impingement-flux-limited—the most desirable condition from the point of view of precursor compatibility—the data points should approach the solid line corresponding to $r_{\text{film}} = r_{\text{gas}}$. It is noted that growth based on Ge₃H₈/SnD₄ is much closer to this limit than its Ge₂H₆/SnD₄ alternative. In the inset is shown an alternative view of the data by plotting the relative Ge/Sn incorporation efficiency $K = r_{\text{gas}}/r_{\text{film}}$ as a function of temperature. While the temperature range is too narrow to confirm an activated behavior, it is instructive to fit the $K(T)$ data with an Arrhenius expression. In the case of Ge₂H₆ growth, $E_a = 0.9$ eV is obtained, which is not too far

from the value $E_a = 1.3$ eV obtained in Ref. 78 for the growth rate activation energy of Ge using Ge_2H_6 . For Ge_3H_8 , the temperature dependence is weaker and the fit activation energy is $E_a = 0.26$ eV.

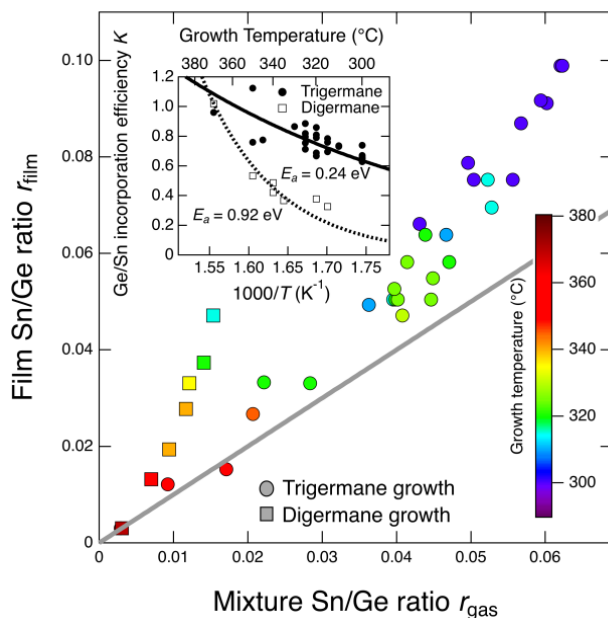


Figure 9 Sn/Ge ratio in $\text{Ge}_{1-y}\text{Sn}_y$ films on Si against the corresponding ratio in the gaseous mixture for the $\text{Ge}_2\text{H}_6/\text{SnD}_4$ and $\text{Ge}_3\text{H}_8/\text{SnD}_4$ deposition reactions. The data for the digermene process are limited to ratios below 5% Sn and temperatures below 355 °C due to the poor reactivity of the compound and inefficient growth rate of the crystal layer under lower temperatures below 330 °C. The solid line corresponds to $r_{\text{film}} = r_{\text{gas}}$. Growth temperatures are indicated by a color code. The inset shows the relative Ge incorporation efficiency K . The lines represent fits using an Arrhenius curve. The corresponding activation energies E_a are indicated in the diagram.

The smaller value is consistent with the increased Ge growth rate observed with this compound, although it is probably less accurate because some data points may lie within the impingement-flux-limited regime. These results strongly suggest that the deviations from the $r_{\text{film}} = r_{\text{gas}}$ line are essentially controlled by the temperature dependence of the Ge growth rate. For the same Sn/Ge ratio in the gaseous mixture, the reduced Ge incorporation using Ge_2H_6 leads to films with higher Sn fraction, but at the price of limited thickness due to the reduced growth rate. On the other hand, the higher

growth rates afforded by Ge₃H₈ make it possible to grow films using much higher Sn/Ge ratios in the mixture, ultimately leading to films with higher absolute Sn concentrations and larger thickness than those grown via the Ge₂H₆ route.

The analysis so far implicitly assumes that the incorporation of Sn and Ge from their respective precursors can be considered as independent events. This appears to be the case in Si_{1-x}Ge_x alloys, for which the growth has been modeled in terms of linear combinations of Si- and Ge-growth rate equations.⁸¹ However, a linear model may not be appropriate for the immiscible Ge-Sn system. The presence of weak Ge-Ge bonds in higher-order germanes may create an opportunity for interactions with SnD₄. For example, insertions of unsaturated SnD₂ into Ge-Ge could produce gas-phase intermediates with preformed Ge-Sn-Ge bonds. Recent reports of Ge growth using digermane and trace amounts of stannane,¹⁶ suggest that interactions between SnD₄ and the Ge sources may indeed play a role, and the lower (0.9 eV vs 1.3 eV) Ge₂H₆ activation energy found here would be consistent with such a view. In this context, an alternative (or complementary) interpretation of my results would follow from the assumption that Ge₃H₈ is more reactive toward SnD₄ than Ge₂H₆. An intriguing scenario to be explored in future work is the possibility that SnD₄ actually reacts *only* with Ge₃H₈. This would imply that Ge_{1-y}Sn_y growth with Ge₂H₆ proceeds via *in-situ* thermolysis to produce Ge₃H₈ in the reaction zone according to



The conversion of Ge₂H₆ to Ge₃H₈ would be less efficient at $T < 330$ °C. This would manifest itself in lower concentrations of Ge₃H₈ in the deposition mixture with decreasing temperature, leading to a concomitant reduction in the growth rates, as observed experimentally.

Optical images of all as-grown materials show a mirror-like appearance largely devoid of cracks and surface imperfections. Atomic Force Microscopy (AFM) scans reveal flat surfaces with root-mean-square (RMS) roughness between 1-5 nm. Transmission electron microscopy (XTEM) indicates the formation of single-phase, mono-crystalline layers with atomically flat surfaces and uniform thicknesses. Figure 10 (a) shows the diffraction data of a ~ 250-nm-thick $\text{Ge}_{0.92}\text{Sn}_{0.08}$ film “as grown” at 300 °C. The phase-contrast image indicates the presence of dense networks of threading defects throughout the lower segment of the layer near the interface region, while the upper portion is relatively devoid of such features within the XTEM field of view.

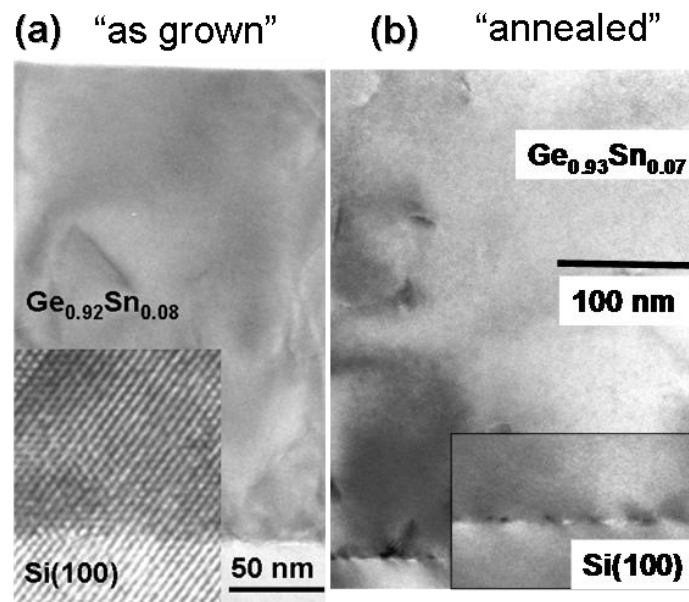


Figure 10 (a) Micrographs of a 250-nm-thick $\text{Ge}_{0.92}\text{Sn}_{0.08}$ layer. The phase-contrast image shows a flat surface and a uniform contrast microstructure indicating a homogeneous single-phase material. Threading dislocations and stacking faults are visible, particularly within the lower portion of the film. A high resolution image (inset) reveals a heteroepitaxial interface. (b) Micrograph of an annealed ~350-nm-thick $\text{Ge}_{0.93}\text{Sn}_{0.07}$ layer doped with P. Inset is a magnified view (4x) of the interface showing a pseudo-periodic array of strain-relieving Lomer dislocations.

Most of these defects correspond to stacking faults near the interface or dislocations that penetrate upward from the interface into the epilayer. High-resolution images (see inset) show a clear transition at the film/substrate heterojunction, and also reveal Lomer-type edge dislocations confined to the interface plane. These absorb much of the misfit strain, as evidenced by high-resolution X-ray diffraction (XRD) measurements of the (004) peaks and (224) reciprocal space maps (RSMs) (Fig. 11), which indicate the presence of a residual compressive strain with a magnitude that increases from 0.1 to 0.4% as a function of composition across the $y = 0.01-0.09$ range in the as-grown films. The lowest strains (0.1-0.2%) were measured in thick layers of dilute alloys ($y = 0.01-0.05$) while the thinner, highly concentrated counterparts ($y = 0.06-0.09$) exhibited the highest values of up to 0.43 % in 250 nm-thick $\text{Ge}_{0.91}\text{Sn}_{0.09}$ films.

Significant improvements of crystal quality were achieved via *ex situ* Rapid Thermal Annealing (RTA). Samples with $y = 0.03-0.04$ were heated at 650 °C for 2-10 second cycles while their $y = 0.05-0.07$ and $y = 0.08-0.09$ counterparts were subjected to similar treatments at 600 °C and 550 °C, respectively. The XTEM micrograph of a $\text{Ge}_{0.93}\text{Sn}_{0.07}$ film shown in Figure 10(b) illustrates elimination of deleterious threading defects within the layer after heating at 600°C. This is accompanied by the formation of strain-relieving edge dislocations at the interface, as visible in the inset of the figure. For samples with $y = 0.03-0.07$, the RTA treatment yielded a nearly relaxed strain state and a narrowing of the FWHM of the (004) rocking curve from 0.6° down to the 0.1°-0.3° range. Figure 11 shows the (224) RSMs for three samples, indicating marked improvement in the crystallographic alignment of the epilayer with the Si(100) platform, as evidenced by the vanishing strain (<0.1 %) and narrow width (~0.2-0.3°) of the rocking curve (not shown). In the case of the $y = 0.08-0.09$ samples, a nominal strain of 0.15-0.20 % remained after prolonged RTA processing at 550°C. This temperature

represents the stability limit for these alloys, which are found to decompose with Sn precipitation at $\sim 575\text{-}600$ °C.

Rutherford backscattering (RBS) spectra were routinely used to measure the elemental content, layer thickness, and epitaxial alignment of the crystals in both as-grown and annealed samples. Representative examples are shown in Fig. 11.

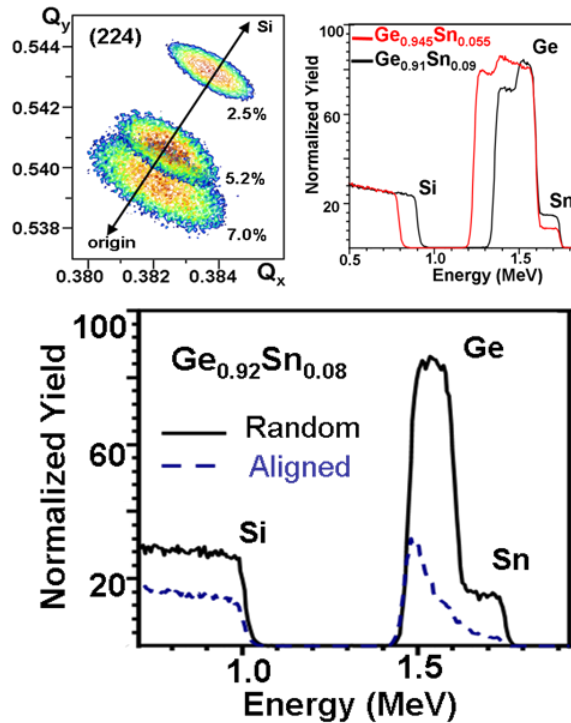


Figure 11. Top left: (224) RSM plots of RTA- processed $\text{Ge}_{1-y}\text{Sn}_y$ films. The relaxation line (double arrow) passes near the peak maximum, indicating mostly relaxed strain states in all cases. Top right: RBS spectra of $\text{Ge}_{0.945}\text{Sn}_{0.055}$ and $\text{Ge}_{0.91}\text{Sn}_{0.09}$ films with thicknesses of 420 and 600 nm, respectively. Note that although the compositions are derived from a detailed fit of the entire spectrum, the intensities of the Sn signal scale linearly with Sn content. Bottom: Aligned and channeled spectra of an “as-grown” $\text{Ge}_{0.92}\text{Sn}_{0.08}$ layer. The ratio of the peak heights indicates that Sn occupies substitutional lattice sites.

The ratio of the channeled over random peak heights (χ_{\min}) in all samples decreased sharply from the interface to the surface, indicating a reduction in the dislocation density across the layer thickness as shown for a 250-nm-thick $\text{Ge}_{0.92}\text{Sn}_{0.08}$ alloy. In addition, the χ_{\min} profile for the Sn and Ge signals was found to be identical in

any given sample, indicating full substitutionality of the atoms in the same tetrahedral lattice. The RTA processing of the films significantly reduced the intensity of the channeled spectrum and lowered the overall χ_{\min} value, as expected due to the elimination of threading defects and overall improvement of microstructure.

Room temperature PL measurements were carried out by exciting the samples with 400 mW of a 980-nm laser beam. The emitted light was collected using a Horiba micro-HR spectrometer equipped with 600 grooves/mm gratings and a single-channel InGaAs detector. Long-pass filters were used to block shorter wavelength light that appears in second order at the wavelengths of the $\text{Ge}_{1-y}\text{Sn}_y$ PL. The spectrometer response was calibrated with a tungsten-halogen lamp and the corresponding correction was applied to all data. Figure 12 shows PL spectra from samples grown with the Ge_3H_8 precursor. RTA was applied in all cases except for the $y = 0.08$ sample.

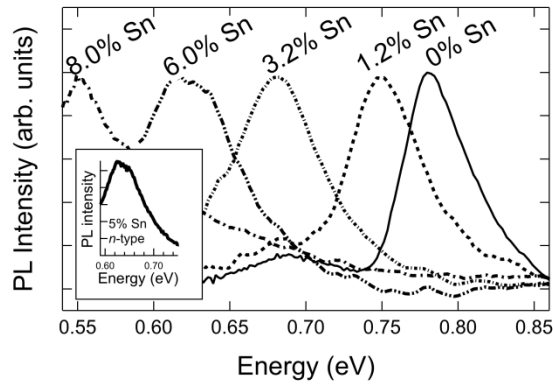


Figure 12. Room temperature PL spectra from $\text{Ge}_{1-y}\text{Sn}_y$ alloys on Si substrates, generated with 980 nm laser excitation. The maxima of all curves have been normalized to facilitate the comparison between different Sn concentrations. The inset shows the spectrum from an n -type sample with $n = 2 \times 10^{19} \text{ cm}^{-3}$.

In general, post-growth RTA is required to observe PL in undoped films. The unexpected observation of PL in the unannealed $y = 0.08$ sample can be attributed to the improved crystallinity and increased thickness of the film, combined with the close proximity of the direct and indirect edges. The inset of the figure shows the PL signal

from an n -type sample with $y = 0.05$ and $n = 2 \times 10^{19} \text{ cm}^{-3}$. The main peak of each spectrum is assigned to direct gap recombination, which dominates the PL spectrum of these films even in the case of pure Ge.¹⁰ The indirect gap emission is seen as a weaker feature near 0.7 eV in the emission from the pure Ge film and as a shoulder in the $\text{Ge}_{1-y}\text{Sn}_y$ spectra. The PL signal from the doped films is significantly enhanced, as reported previously.¹⁰ A monotonic shift to lower energy is observed as the Sn concentration is increased. Due to the residual strain and the asymmetric nature of the direct gap emission,¹⁰ the maxima in the spectra correspond only approximately to the value of the direct band gap. Nevertheless, the maximum near 0.55 eV for $y = 0.08$ confirms a strong deviation from a linear interpolation between Ge and α -Sn, according to which the direct band gap should be $E_0 = 0.70 \text{ eV}$. Most importantly, light emission is observed at Sn concentrations that exceed the most recent predictions ($y \sim 0.06$) for the crossover between indirect and direct lowest band gaps,^{8,82} confirming that the Ge_3H_8 -based approach will enable the study of this transition which may lead to the first direct gap group-IV compound on Si.

Summary

I have introduced Ge_3H_8 as a superior alternative to Ge_2H_6 for the growth of $\text{Ge}_{1-y}\text{Sn}_y$ alloys in which SnD_4 is used as the source of Sn. The advantages of the Ge_3H_8 precursor are particularly noticeable when for films with high Sn concentrations ($y > 0.04$), which require very low growth temperatures when growth rates plummet using the Ge_2H_6 precursor. By contrast, Ge_3H_8 still maintains a significant reactivity at these low temperatures, enabling the growth of thick films suitable for optical characterization and possible direct-gap devices on Si. The protocols developed here provide an unprecedented level of reproducibility and process reliability, as required for deployment of this approach at both the laboratory and industrial manufacturing scales.

Chapter 5

INTRODUCING HIGHER ORDER GERMANES FOR ULTRA LOW-TEMPERATURE EPITAXY OF GE-BASED SEMICONDUCTORS: TRIGERMANE, TETRAGERMANE

*Reprinted with permission from “Ultra Low-Temperature Epitaxy of Ge-based Semiconductors and Optoelectronic Structures on Si(100): Introducing higher order germanes (Ge_3H_8 , Ge_4H_{10})” G. Grzybowski, L. Jiang, R. T. Beeler, T. Watkins, A. V. G. Chizmeshya, C. Xu, J. Menéndez, and J. Kouvetakis, *Chemistry of Materials* 24 (9), 1619 (2012). American Chemical Society*

Introduction

Germane is the most commonly used hydride for the chemical vapor deposition of Ge-based materials and devices for applications in group IV microelectronic and optoelectronic technologies. The compound is widely available at the industrial scale in high purity form and it is routinely used to create—effectively and efficiently at appropriate temperatures— polycrystalline and epitaxial Ge films on substrates via complete thermal dehydrogenation. The digermane derivative is obtained as a byproduct in the commercial synthesis of bulk germane and it is typically utilized in niche low temperature processing, including selective area deposition of crystalline films at high growth rates, and fabrication of SiGeSn alloys under metastable conditions on silicon. The higher order trigermane has not been utilized for Ge deposition despite the expected facile reactivity, which is likely to enable ultra-low temperature processing in high performance devices and flexible photovoltaic formats.^{83,84}

Together, digermane and trigermane should significantly expand the process condition space available for the deposition of Ge-based materials under CMOS

compatible protocols. The broader temperature profile of these molecules overlaps with that of high-reactivity co-reactants, enabling the formation of kinetically stabilized compounds that are only accessible at lower temperatures (<400 °C).^{45,77,85,86} In the case of digermane, the synthesis of novel Si-Ge-Sn semiconductor alloys and the introduction of low defectivity, atomically flat layers of pure Ge on Si wafers^{87,88} represent dramatic examples of this compounds' enhanced deposition versatility. The promising new approach to Ge-on-Si suggests that Ge can be reintroduced as a practical active semiconductor for the design and realization of the next generation of high speed devices directly on silicon.^{64,89}

In the case of Si-photonics the near direct-gap character of Ge has fueled a dramatic rise in global research and development of more sensitive photodetectors, high speed modulators, and very recently laser diodes based entirely on conventional designs using Ge as the active material.^{38,90,91} In the latter case the quasi direct condition required for lasing is achieved by the simultaneous application of tensile strain and heavy *n*-type doping of the Ge layers using CVD of germanes.³⁸ From a crystal growth perspective there is a strong demand to develop new lower temperature CVD routes to replace state-of-the-art methods traditionally used to control defect microstructure and layer morphology.^{83,87,92} For example, post growth annealing cycles in these technologies invariably produce extended defects due to the thermal mismatch with silicon, while the high temperature step used to accelerate growth following the initial low temperature layer deposition also induces strains, defects and cracks which ultimately degrade the material performance.^{88,93} The ideal process should efficiently convert gas-phase Ge into thick, optical quality Ge films on silicon at the highest possible, most cost effective growth rates (commercial scale), but lowest possible temperatures to avoid the materials issues described above. This indicates that higher order germanes such as trigermane,

which is predicted to exhibit a reasonable vapor pressure of ~ 25 Torr at room temperature, may represent a suitable candidate for the development for such a process.

Higher order hydrides have already made a significant contribution in the silicon technology space, where the trisilane analog (available under the trade name “Silcore”)^{94,95} or even the heavier neopentasilane⁹² have been successfully used to enhance deposition processes in the commercial sector. In this connection trigermane is not yet commercially available as a chemical source, presumably due to the lack of practical synthesis methods to produce sufficient amounts of the pure product. The best known (widely reported) synthesis of trigermane was conducted almost 40 years ago via an electric discharge decomposition of germane gas, resulting in low yields of the main product intermixed with higher mass analogs which were tentatively identified as tetragermane and pentagermane.^{96,97} The poor production rate and the complicated experimental setup makes this method difficult to implement for large-scale production of semiconductor grade material, as required for application in materials science as described above. Nevertheless, sufficient quantities of the compound were obtained to allow some basic characterizations and preliminary demonstration of the molecular synthesis of its halide derivatives.^{98,99}

Prior mechanistic studies involving insertion reactions of silylenes and germylenes into Si-Si and Ge-Ge bonds have identified the formation of trace amounts of trisilane and trigermane byproducts by thermal decomposition of their lower order counterparts. However, the isolation of the compounds for bulk analysis or subsequent use was apparently not pursued.¹⁰⁰ Another reason for limited use of higher-order germanes may be related to the purported instability of Ge₂H₆, which have prevented its availability in pure liquid state and have casted uncertainty for the potential development and possible deployment of the even more reactive Ge₃H₈ as a potential

laboratory reagent and, perhaps more importantly, as a commercial semiconductor source. In fact, the open literature offers very limited information regarding the fundamental thermodynamic and structural properties of Ge_3H_8 as well as the determination of its physical behavior.

The focal point of my study was to develop a practical synthesis route that allows the isolation of significant amounts of the Ge_3H_8 , enabling a thorough characterization and its application as a viable ultra-low temperature deposition source for the fabrication of Ge-based semiconductors on Si. My first synthetic attempts employed a thermolysis reaction of digermene, as described by the equation below, to obtain a high yield of the pure product in gram quantities, allowing a determination of its physical behavior and stability range.

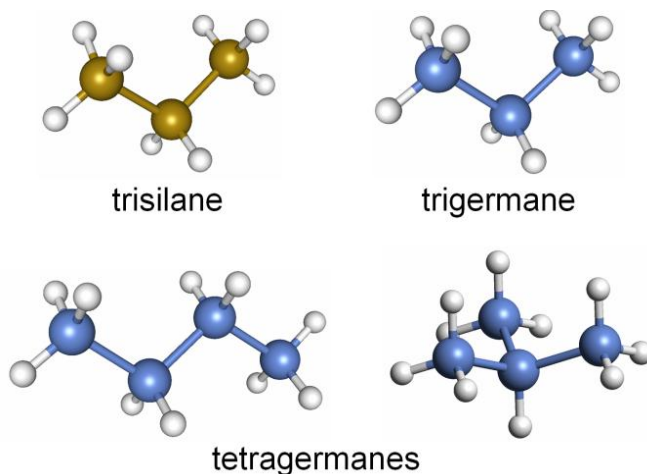


Figure 13: Molecular structures of trisilane (Si_3H_8), trigermene (Ge_3H_8) and the two tetragermene (Ge_4H_{10}) isomers produced in this study. Legend: Si (gold), Ge (blue), H (white).



Several years ago an analogous reaction to produce bulk trisilane from disilane was described in the patent literature for use in semiconductor fabrication.¹⁰¹ In the above idealized reaction (5) two moles of digermene dissociate to yield equimolar

amounts of germane and trigermane, implying a maximum theoretical yield of 50 % product and GeH_4 byproduct, which contains the remaining balance of Ge. In principle the GeH_4 can be completely recycled with no net loss, thereby also making the process cost effective for bulk production as needed in large scale crystal growth applications. In this chapter it is shown that the above reaction generates trigermane as the primary decomposition product. The trigermane is isolated from the main GeH_4 byproduct and then purified as a colorless volatile liquid. This process also yields a small amount of tetragermane (butane analog with enhanced reactivity) which was isolated as a mixture of perfectly stable isomers, as shown in Figure 13. Significant quantities of the compounds were obtained and were found to be perfectly stable, allowing a full characterization using modern experimental and theoretical methods, in order to elucidate their fundamental structural, vibrational and thermodynamic properties. In this study samples of pure trigermane and tetragermane were subsequently employed to conduct proof-of-concept depositions of Ge and GeSn films on Si wafers. The initial results are highly encouraging and indicate that the growth rate of pure Ge on Si using Ge_3H_8 is significantly enhanced—up to 30 times—over the current state-of-the-art process using digermane under the same conditions. In addition, the rapid formation of high-Sn content GeSn films on Si (100) has been observed using significantly reduced amounts of the precursor relative to Ge_2H_6 , indicating that the conversion of gaseous Ge hydride into solid material proceeds with higher efficiency. Furthermore, in both cases the crystal quality of the resultant films is comparable to the best results obtained using Ge_2H_6 , suggesting that the learning curve for the translation of the new trigermane-based process into the device arena will be extremely rapid. Finally it is shown that tetragermane provides the ultimate pathway for the formation of Ge-on-Si structures

with the desired optical and materials properties. It is speculated that further gains will be difficult to realize using chemical means.

Experimental, results, and discussion

The pyrolysis reactor comprises of a 1 inch pyrex tube packed with glass wool and heated by a “clam shell” resistance furnace with a nominal hot zone of ~ 12 inches long. The exhaust of the tube is connected in series to two sequential glass traps cooled to -196°C which can be individually isolated using high vacuum valves. The inlet of the tube is connected to a bubbler charged typically with several grams of liquid digermane, typically held at a target temperature of -30°C. Under these conditions the vapor pressure of Ge₂H₆ is ~ 25 Torr, which is sufficient to permit controlled transport of the vapor into the reactor assuming that high purity H₂ as a carrier gas is fully saturated. The flow of H₂ is regulated using a calibrated flow meter so that both the amount of reactant and its retention time in the reactor can be adjusted as needed to optimize the reaction conditions and maximize yields of the products.

Both the bubbler and the terminal trap are connected to a high vacuum line to allow differential pumping of the entire system before and after the pyrolysis experiment, and also transfer and collection of the final products and unused reactant. The vacuum line is equipped with several capacitance manometers to accurately measure pressures in the range of 0.1-1000 Torr and a mercury bubbler that serves as a “release valve” to vent the H₂ carrier gas overpressure from the closed loop system. The mercury in the bubbler prevents atmospheric back flow ensuring that the entire process is carried out under inert conditions and a total pressure of 760 Torr. A reaction temperature of 225 °C yielded no measurable decomposition of digermane under my reaction conditions (H₂ flow rate etc.) as evidenced by almost full recovery of the starting material, visual change in the appearance of the tube and packing material. Increasing the temperature

to 250 resulted in significant condensation of products in both traps and the formation of a very thin metallic coating inside the tube, presumably due to the formation of Ge-like residue.

Upon completion the cold traps containing the products, and any un-reacted source material, are isolated from the pyrolysis chamber, pumped to remove the H₂ ambient (note that H₂ does not condense at -196°C) and then warmed to room temperature while monitoring their pressure using the in-line manometers. The combined volatile content from both traps is then separated through fractionation to isolate the individual components of the pyrolysis mixture. Germane, trigermane and digermane are collected by trap-to-trap distillation at -196, -110 and -78 °C respectively. In addition a small amount of colorless mobile liquid with a nominal vapor pressure of 1.5 Torr is typically recovered at a -35°C trap and has been identified as tetragermane, as discussed below. Pure trigermane is also obtained as a colorless liquid with a room temperature vapor pressure of 21 Torr, close to the predicted 25 Torr value. Under these conditions the dissociation of ~ 2.5 grams of digermane yielded ~1.0 gram of trigermane, which represents a 55 % yield on the basis of the idealized reaction above. In addition ~ 0.30 grams of tetragermane was produced as well as 0.90 grams of germane, indicating the presence of more complex reactions channels under the current protocols. Nevertheless, my experiments thus far represent a very small excursion in a very wide parameter space that includes temperature, pressure, retention time, mass flow, tube diameter and type (glass vs. metal), length of hot zone, packing medium etc. All of these parameters can in principle be adjusted to maximize yield using the present results as a starting point. The relatively high yield obtained thus far is encouraging and indicates that further improvements of the process output may be within reach.

The collective output from several reaction runs provided sufficient amounts of material (~ 7 g) to enable a series of deposition studies using trigermane as chemical source for the first time, as described in chapter 4. In addition 1.5 grams of tetragermane were also collected. Both of these products were stored in glass vessels at room temperature and exhibited no visible color change, or other signs of decomposition. However, in the case of tetragermane infrared spectroscopy revealed trace amounts of germane over the span of approximately 1-2 months.

The structural properties of the molecules and the purity of all samples were investigated by NMR spectroscopy using a 500 MHz Varian spectrometer and the results obtained appeared consistent with those reported in early synthetic studies.⁹⁸ However, the superior quality of my samples and the availability of higher resolution NMR techniques clearly illustrates the perfect analogy with propane and butane structures and conformations for the first time. In the case of trigermane the ¹H spectrum showed two sets of peaks corresponding to a triplet at 3.273 ppm, integrated for six protons, as well as a septet at 3.18 ppm, integrated for two protons, as expected due to the terminal GeH₃ and the bridged GeH₂ moieties, respectively. The ¹H spectrum of the tetragermane sample indicated a mixture of the two configurational isomers with resonances exhibiting the appropriate multiplicities (see Figure 14).

The peaks of the *n*-Ge₄H₈ (straight chain) appeared as a triplet at 3.273 pp and a quartet at 3.18 ppm corresponding to the central GeH₂-GeH₂ and GeH₃ fragments of the molecule. Both peaks are significantly broadened due to the presence of the gauche and trans conformers, reminiscent of those observed in the classic n-butane proton spectrum. In contrast, the resonances of the *i*-Ge₄H₈ are sharp and distinct, and appeared as a doublet at 3.384 ppm and a decet at 2.868 ppm integrating for 9 and 1 protons, respectively, as expected. These assignments were confirmed by 2-D COSY

NMR spectroscopy. The combined integrated intensities of the peaks in the spectra indicated that the normal and iso species are typically present in a ~ 5:1 ratio in my samples.

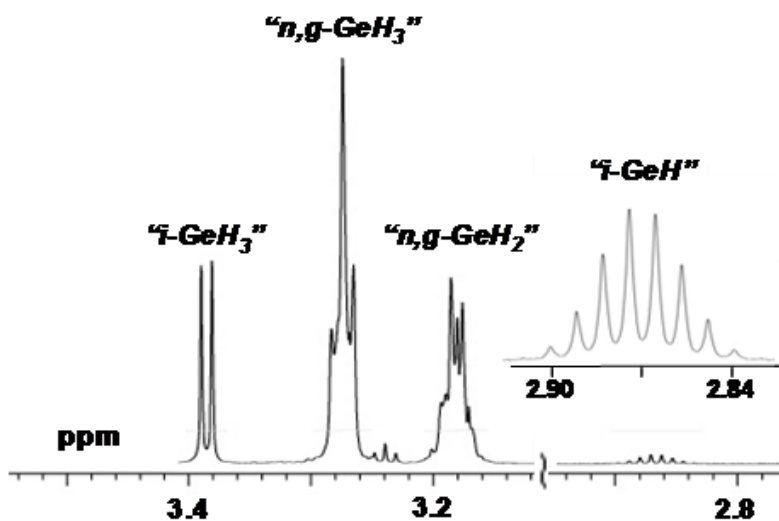


Figure 14: 500 MHz ^1H spectrum of the isomeric tetragermane mixture showing resonances corresponding to the various “ GeH_x ” moieties of the $i\text{-GeH}(\text{GeH}_3)_3$ as well as the “n” and “g” conformers of $\text{GeH}_3\text{GeH}_2\text{GeH}_2\text{GeH}_3$. The inset is a magnified view of the Ge-H resonance of the iso compound at 2.7 ppm. The 1J coupling constants from left to right are 4.28, 4.52, 4.64 and 4.41 Hz. The weak triplet in the vicinity 3.28 ppm is due to residual traces of trigermane.

The preceding isomeric ratio is in fact very similar to that obtained for liquid mixtures of commercially available tetrasilanes (Voltaix Corp) in which all of the same structural/composition conformers are present. However, the proportions of isomers in the gas phase are expected to differ from those of the liquid, and therefore the isomeric composition of the gas phase flux used as a CVD source will have a significant effect on the design and interpretation of film deposition, including layer morphology, kinetics of film assembly and other key crystal growth properties. In fact, it is remarkable that detailed studies comparing the properties of high-order group IV hydrides of Si and Ge with their classic butane analog are scarce, even though the similarities are quite apparent. For this reason in-depth characterizations have been carried out of the

vibrational and configurational behavior of gas phase trigermane and tetragermane using IR spectroscopy and quantum chemical simulations. The latter support the identification of the molecules, and provide a rigorous vibrational and thermodynamic basis for establishing the more elusive isomeric proportions in the case of tetragermane.

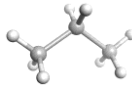
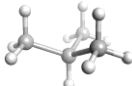
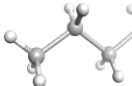
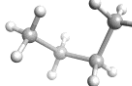
Quantum Chemical Simulations of Structural, Vibrational and Thermochemical Properties

In prior studies it was demonstrated that B3LYP hybrid density functional theory (DFT) simulations provide an excellent account of the ground state structural, thermochemical and vibrational properties of the $(\text{H}_3\text{Ge})_x\text{SiH}_{4-x}$ and butane-like Si-Ge hydride family of molecules.^{102,103} In the present work the ground state properties of trigermane and tetragermane isomers were calculated using density functional theory (DFT) as implemented in the *Gaussian03* code.¹⁰⁴ The prior work in adopting the B3LYP hybrid exchange-correlation functional in conjunction with a standard 6-311G++(3df,3pd) basis set was followed. Using so-called “very tight” structural convergence criteria, “ultrafine” integration grids and without imposing any symmetry constraints, simulations yielded the static ground state molecular structures listed in Table 1, below. In all cases all harmonic normal mode frequencies were calculated to be positive definite, indicating that the ground state structures are dynamically stable. A symmetry analysis of the final structures yielded C_{2v} , C_{3v} , C_{2h} and C_2 point groups for the Ge_3H_8 , $i\text{-Ge}_4\text{H}_{10}$, $n\text{-Ge}_4\text{H}_{10}$ and $g\text{-Ge}_4\text{H}_{10}$ molecules, respectively.

The bond lengths obtained from the simulations follow the expected trends and are in excellent agreement with those obtained by other authors, and those reported in prior work on trigermane and tetragermane¹⁰⁵ using slightly smaller basis sets and coarser grids. For example, the shortest Ge-Ge bond lengths (2.444 Å) typically occur between $-\text{GeH}_3$ and $-\text{GeH}_2-$ moieties, while slightly longer values (2.450 Å) prevail

between $-\text{GeH}_3$ and $-\text{GeH}-$, or adjoining $-\text{GeH}_2-$ groups. The Ge-H bond lengths follow the expected increasing trend 1.537 Å, 1.542 Å and 1.545 Å for the $-\text{GeH}_3$, $-\text{GeH}_2-$

Table 1: Summary of structural and energetic results for trigermane and three isomers of tetragermane. The subscripts “T” and “S” refer to terminal and sagittal H-Ge-H bond angle species. The asterisk on the $(\text{Ge-H})_s$ bond length in $i\text{-Ge}_4\text{H}_{10}$ indicates that the $-\text{Ge-H}$ moiety is distinct from the other sagittal $-\text{GeH}_2-$ moieties.

					
		Trigermane (Ge_3H_8)	iso-Tetragermane ($i\text{-Ge}_4\text{H}_{10}$)	n-Tetragermane ($n\text{-Ge}_4\text{H}_{10}$)	g-Tetragermane ($g\text{-Ge}_4\text{H}_{10}$)
<i>Point Group</i>		C_{2v}	C_{3v}	C_{2h}	C_2
<i>Bond Lengths (Å)</i>	Ge-Ge	2.444	2.450	2.445(×2), 2.449	2.444(×2), 2.451
	$(\text{Ge-H})_T$	1.537 (×3)	1.538(×3)	1.537(×2), 1.538	1.537(×2), 1.538
	$(\text{Ge-H})_S$	1.541	1.545*	1.542	1.542
<i>Bond angles (degrees)</i>	$\angle\text{Ge-Ge-Ge}$	112.9	110.5	113.1	113.1
	$(\text{H-Ge-H})_T$	108.4, 108.5(×2)	108.4(×2), 108.5	108.4, 108.5(×2)	108.4, 108.5(×2)
	$(\text{H-Ge-H})_S$	107.2	--	107.1	107.3
<i>Dipole Moment (D)</i>		0.0389	0.0708	0.0000	0.0361
<i>Thermochemistry ($T=298\text{K}$, $P=1\text{atm}$)</i>	E_0 (a.u.)	-6235.86419	-8314.09421	-8314.09378	-8314.09316
	E_0+E_{th} (a.u.)	-6235.79414	-8314.00513	-8314.00435	-8314.00407
	E_0+H_{th} (a.u.)	-6235.79319	-8314.00419	-8314.00341	-8314.00312
	E_0+G_{th} (a.u.)	-6235.83725	-8314.05737	-8314.05526	-8314.05483
	S (cal/mol K)	92.73	111.93	109.12	108.83

and $-\text{GeH}-$ moieties, respectively. The bond angle trends in these molecules also exhibit systematic patterns with typical $\angle\text{Ge-Ge-Ge}$ angles of 113.1° among the molecules/isomers containing a C_2 symmetry character, but a more tetrahedral value of 110.5° in the case of the $i\text{-Ge}_4\text{H}_{10}$ species possessing C_{3v} symmetry. While the torsion angle among the Ge atoms adopts trivial values for the high symmetry species, 58° for the gauche tetragermane isomer was obtained, which is quite close to the typical 63° value found in the gauche isomer of butane.¹⁰⁶ The dipole moments of the molecules corresponding to the equilibrium ground structures described above (listed in Table 1) indicate a maximum value of 0.071 D for the $i\text{-Ge}_4\text{H}_{10}$ molecule, similar values in the range of $\sim 0.32\text{-}0.36$ for Ge_3H_8 and $g\text{-Ge}_4\text{H}_{10}$, and a vanishing dipole moment for the $n\text{-Ge}_4\text{H}_{10}$, as expected on the basis of its symmetry.

The standard thermochemistry output from *Gaussian03* at T=298K and P=1 atm is also summarized in table 1 and includes the static electronic energy of the molecules, E_0 , as well as its thermally corrected counterparts for internal energy (E_{th}), enthalpy (H_{th}) and free-energy (G_{th}). A key outcome of these calculations for the tetragerminal species is that the *i*-Ge₄H₁₀ has the lowest free-energy (by ~ 4.4 kJ/mol), followed by *n*-Ge₄H₁₀, and *g*-Ge₄H₁₀, whose free-energies differ by a mere ~ 1 kJ/mol. These free-energies are used to develop a simple isomerization model, as described below. Finally, the table lists the molecular entropies of the molecules obtained at T=298 K for trigermene and the tetragermene isomers. In view of its relatively weak mass dependence, the translational component of the entropy (~ 43 cal/mol K) is approximately the same for all molecules and the overall magnitude of the total entropy is essentially controlled by the vibrational term, which is ~ 14.6 cal/mol K for trigermene and typically 35-39 cal/mol K for the tetragermene isomers, with *i*-Ge₄H₁₀ being dominant. By contrast, the largest rotational term occurs in the *n*-Ge₄H₁₀, due to its larger moment of inertia.

As shown in Figure 15 the calculated vibrational spectrum of trigermene is separated into two categories corresponding to high-frequency Ge-H stretching vibrations (2000-2150 cm⁻¹), and lower frequency Ge-H wagging and bending motions as well as Ge-Ge-Ge backbone vibrations (<1200 cm⁻¹). Based on prior work on closely related Si-Ge hydrides calculated using the same methodology, the differences between the observed frequencies and those calculated are reconciled using well-established scale factors 0.995 and 0.975 for the low and high frequency ranges, respectively. The corresponding plots of the calculated spectra are compared directly with those measured experimentally in Figure 15, and indicate generally good agreement. The lowest frequency normal modes, labeled ν_1 - ν_3 in the figure are assigned as follows: ν_1 – in-phase

GeH₃/GeH₂ wagging || (e.g., parallel) to backbone, ν_2 – anti-phase wagging of the GeH₃/GeH₂ || to backbone. The most intense IR modes are labeled as ν_3 – ν_7 and are assigned as follows: ν_3 – intense GeH₂ wagging || to backbone, ν_4 – intense in-phase GeH₂ wagging || to backbone, ν_5 – intense anti-phase GeH₂ wagging || to backbone, ν_6 –

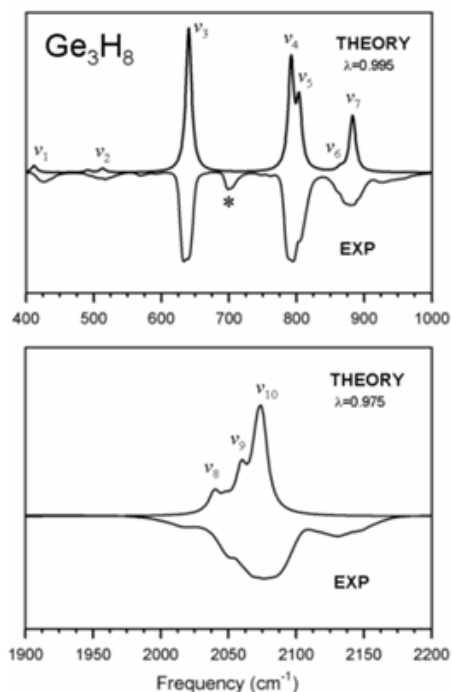


Figure 15: Comparison of the calculated and experimental IR spectrum for trigermane. Primary spectral features are designated ν_1 – ν_{10} and discussed in the text. The frequencies of simulated spectra were scaled by factors of 0.995 and 0.975 in low- and high-frequency ranges, respectively.

this band contains three very closely spaced frequencies corresponding to in-phase wagging of the terminal -GeH₃ protons \perp (e.g., perpendicular) to backbone (ν_6), as well as a in-phase and anti-phase pair of vibrations involving scissor-like GeH₃ motion \perp to backbone. It is noted that the calculated trigermane spectrum does not produce any vibrational modes in the vicinity of the 700 cm⁻¹ feature observed experimentally. However, this peak has in fact been observed in some of the first spectra recorded for this molecule, suggesting that the absorption is inherent to the pure compound.

Furthermore, the NMR spectra of trigermane (discussed above) indicate that the bulk sample is highly pure thereby precluding the assignment of this peak to a contaminant/impurity. A possible origin for the 700 cm^{-1} feature is a combination band, but a complete analysis of this mechanism is beyond the scope of the present study. The higher frequency portion of the calculated spectrum is shown in the lower panel of Figure 15, and indicates a complex band of frequencies corresponding to symmetric and anti-symmetric Ge-H stretches in various in-phase and anti-phase combinations. For example, the most intense features labeled as ν_{10} correspond to in-phase but anti-symmetric H-Ge-H modes within the $-\text{GeH}_3$ groups, while ν_8 contains closely spaced frequencies corresponding to symmetric and asymmetric stretches of the bridging $-\text{GeH}_2-$ moiety. Finally, the mode designated as ν_9 is associated with in-phase asymmetric stretching of Ge-H bonds in the terminal $-\text{GeH}_3$ groups. The above comparisons with experiment corroborate the high degree of purity of the gas phase product, which is consistent with the “text-book” NMR spectrum of the corresponding propane-like liquid phase, completely devoid of any impurity signatures.

Thermochemistry of tetragermanes

In the case of tetragermane I consider the existence of classic butane-like isomerization comprised of two conformational isomers (“trans” and “gauche”, referred to below simply as $n\text{-Ge}_4\text{H}_{10}$ and $g\text{-Ge}_4\text{H}_{10}$) and one positional isomer analogous to isobutane (referred to as $i\text{-Ge}_4\text{H}_{10}$). The predominance of any one isomer in the gas phase has important implications for the use of tetragermane as a deposition source in CVD growth of Ge-based materials. It is expected that the most thermodynamically stable configuration will lead to the most facile assembly of crystalline Ge at ultra low-temperatures. This is manifested in the analogous growth of silicon on Si(100) using the neo-pentasilane sources, which purportedly decompose on the surface via the formation

of iso-tetrasilane intermediates.⁹² According to the thermochemical data in Table 1 the most stable species is *i*-Ge₄H₁₀, which is consistent with the trends observed in classic butane, where simple gas phase models predict a room temperature equilibrium ratio of ~ 9:1 for *i*-C₄H₁₀/*n*-C₄H₁₀.¹⁰⁶ The calculated vibrational spectra of the tetragermane isomers are shown in Figure 16 (top and bottom corresponding to low- and high-frequency regimes), where they are compared with an experimental spectrum of a gas sample. The latter was obtained from a freshly distilled bulk liquid aliquot which was previously characterized by NMR (discussed above), showing a mixture of 85% *n*-Ge₄H₁₀ and 15% of *i*-Ge₄H₁₀, where the 85% can in principle be further subdivided into “trans” and “gauche”, which can not be clearly resolved by NMR.

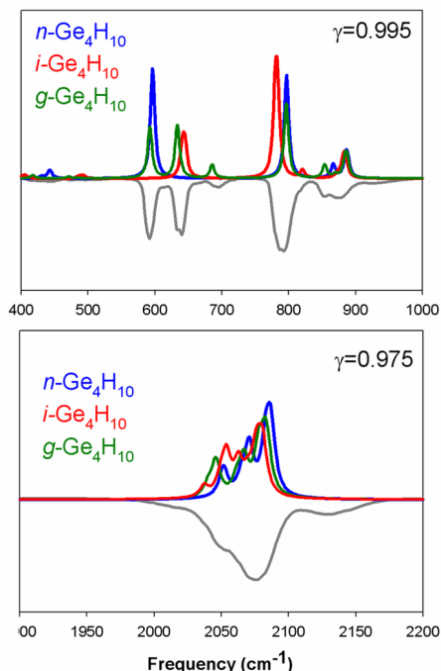
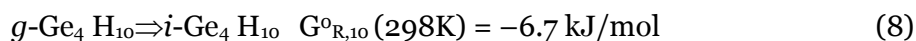
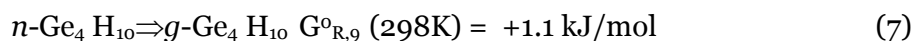
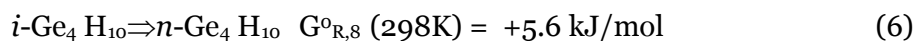


Figure 16: Low- /high- frequency IR spectra of the individual isomers used to construct the composite spectrum. The individual frequency scale factors (γ) are the same as those employed in the trigermane calculations (Figure 15).

I note, however, that the presence of two isomers in the dominant fraction is consistent with the broadening of the NMR signals for the “*n*-Ge₄H₁₀” species. The

simulated gas phase IR spectra shown in Figure 16 (top) clearly indicate that the spectral signatures of the individual isomers are unique and fairly well resolvable. For example, the intense band in the vicinity of 600 cm⁻¹ originates mainly from an intense *n*-Ge₄H₁₀ vibration associated with in-phase GeH₃/GeH₂ wagging || to Ge₄ backbone, while the strongest absorption near 780 cm⁻¹ is due to GeH₃ wagging || to a Ge-Ge bond axis in *i*-Ge₄H₁₀, where the apparent broadening is due to the close coincidence of the latter with another normal of *n*-Ge₄H₁₀ occurring near 800 cm⁻¹ due to in-phase GeH₃ wagging || to backbone. The spectra also show that the complex band bear 640 cm⁻¹ is due to wagging motions of the lone Ge-H at the tertiary site, which is entirely unique to the *i*-Ge₄H₁₀ species. Collectively the data described thus far clearly indicates the presence of significant amounts of *i*-Ge₄H₁₀ in gas phase tetragermane. Note that the Ge-H bands shown in Figure 16 (bottom) are rather complex with regards to the individual isomer contributions, but that the overall shape of the envelope is well reproduced by theory. More detailed peak assignments will be described elsewhere, but I refer the reader prior work on the analogous butane-like Si-Ge hydride molecules.⁸⁶

In prior work on isomeric mixtures in butane-like Si-Ge hydride molecules the concept of fitting a linear combination of calculated isomeric vibrational spectra to the measured spectrum of a mixture is introduced, in order to ascertain the proportions. Here a fitting procedure is avoided and instead a more straightforward thermodynamic approach is considered. From the E₀+G_{th} values listed in Table 1 the reaction free-energies for the three isomer inter-conversion reactions are obtained:



where it is noted that $\sum_m \Delta G_{P,m}^0 = 0$. Defining the extents of reaction as x , y and z

for reactions (6), (7) and (8), respectively, simple mass balance yields the mole numbers $n_{Ti} = n_{Ti}^0 - x + z$, $n_{Tn} = x - y$ and $n_{Tg} = y - z$, for the *iso*-, *n*- and *g*- species, respectively.

Then, assuming ideal gas behavior, the equilibrium constants are explicitly given by

$$K_{P,8}^0 = \frac{P_{Tn}/P^0}{P_{Ti}/P^0} = \frac{n_{Tn}}{n_{Ti}} = \frac{x-y}{n_{Ti}^0 - x + z}, K_{P,9}^0 = \frac{P_{Tg}/P^0}{P_{Tn}/P^0} = \frac{n_{Tg}}{n_{Tn}} = \frac{y-z}{x-y}, K_{P,10}^0 = \frac{P_{Ti}/P^0}{P_{Tg}/P^0} = \frac{n_{Ti}}{n_{Tg}} = \frac{n_{Ti}^0 - x + z}{y-z}$$

Where the condition $\sum_m \ln K_{P,m}^0 = 0$ is imposed by the cyclic nature of the reaction equations, and reduced the system to two independent equations with solutions

$$n_{Ti} = \frac{n_{Ti}^0 K_{P,10}^0}{1 + K_{P,10}^0 (1 + K_{P,8}^0)}, \quad n_{Tn} = \frac{n_{Ti}^0 K_{P,8}^0 K_{P,10}^0}{1 + K_{P,10}^0 (1 + K_{P,8}^0)}, \quad n_{Tg} = \frac{n_{Ti}^0}{1 + K_{P,10}^0 (1 + K_{P,8}^0)}$$

where the total mole number is $n_{TOT} = n_{Ti} + n_{Tn} + n_{Tg} = n_{Ti}^0$. Substitution of the 298K free-

energies from Table 1 then yields $K_{P,8}^0 = 0.1067$, $K_{P,9}^0 = 0.6381$ and $K_{P,10}^0 = 14.6915$,

which in turn predicts an isomeric mixture consisting of $n_{Ti} \sim 80\%$, $n_{Tn} = 12\%$ and

$n_{Tg} = 8\%$. This is clearly in contrast with the NMR data for the liquid mixture, and is

quantitatively consistent with the experimental IR spectrum. To obtain a more

quantitative estimate the equilibrium constants at the lower temperature (<-35 °C) from

which the gas analyte was drawn are evaluated. The assumption here is that the isomeric

inter-conversion is sufficiently slow to make the lower temperature equilibrium mixture

more relevant. Accordingly I re-evaluated the thermochemistry for Rx(6)-(8) over the

expanded range (200-600K), yielding the equilibrium mole fraction plots shown in

Figure 17(a). These results indicate that the lowest free-energy isomer, *i*-Ge₄H₁₀ (black

trace), is dominant at high temperatures as expected, but that its' proportion is reduced

at lower temperatures at the expense of n -Ge₄H₁₀ (red trace) and g -Ge₄H₁₀ (green trace) isomer species.

The infrared spectrum of tetragermane was then simulated by combining the calculated spectra of i -Ge₄H₁₀, n -Ge₄H₁₀ and g -Ge₄H₁₀, in a 75%, 15%, 10% proportions, as shown in Figure 17(b). The resulting composite spectrum compares very well with the experimental counterpart indicating that principal character (frequencies and intensities) are well accounted for. In particular I note that a composite spectrum based on the liquid phase NMR proportions, with a dominant n -Ge₄H₁₀ fraction, could

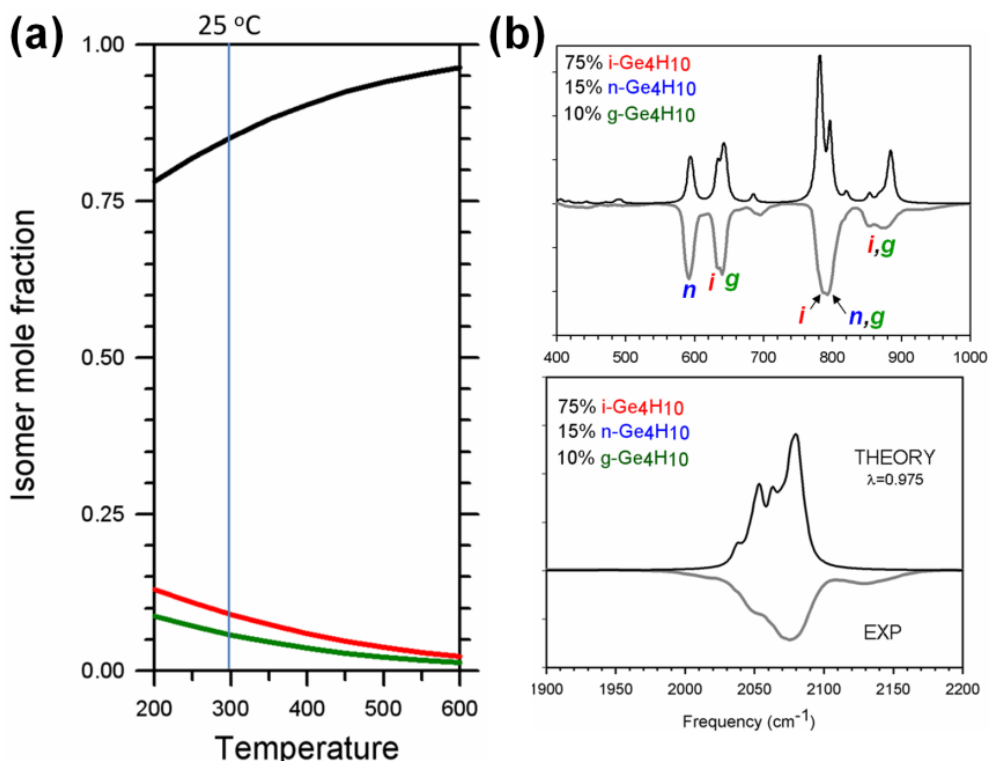


Figure 17:(a) Calculated temperature dependence of the tetragermane isomer mole fractions from 200-600 K, where the proportion of i -Ge₄H₁₀ increases with temperature, reaching nearly ~100% at typical deposition temperatures for crystalline Ge on Si(100). (b) Composite spectrum of the tetragermane corresponding to the low-temperature combination 75%, 15%, 10% of “iso”, “n” and “g” species as for the case of trigermane (Ge₃H₈) above, I applied frequency scale factors of 0.995 and 0.975 to the simulated spectra in the low- and high-frequency regimes.

not account for the observed gas phase spectrum.

The predominance of the *i*-Ge₄H₁₀ species in the gas phase suggests that depositions could be carried out with unprecedented efficiency at low-temperatures using this source, as discussed below. This development may represent a key milestone towards the realization of intricate device formats via selective growth in high-speed Si-Ge based transistor structures on Si(100).

Conclusions

In analogy to the related Si and Si-Ge counterparts, in this work I introduce viable preparations of trigermane (Ge₃H₈) and tetragermane (Ge₄H₁₀) for applications in semiconductor materials science and technology. The compounds are produced in relatively high yield and purity via thermolysis of Ge₂H₆, as implemented in a flow through reaction arrangement. They are thoroughly characterized using spectroscopic methods and first-principles quantum simulations, which provide detailed new information concerning the molecular properties and stability range, which had remained elusive to date. A key conceptual motivation of the work is the potential of these heavy hydride chemical sources to dramatically expand the functionality of group IV devices comprising of Ge-based architectures. This is achieved by lowering the process temperatures while increasing the crystal growth rate in selective and blanket growth, thereby allowing the formation of metastable structures and alloy compositions not accessible using conventional methods.

Chapter 6

GROUP III-V/IV ALLOYS OF AL, N, P, AS, AND SI GROWN ON SI(100)

Reprinted with permission from “Synthesis and properties of monocrystalline Al(As_{1-x}P_x)Si₃ alloys on Si(100)”; G. Grzybowski, T. Watkins, R. T. Beeler, L. Jiang, D. J. Smith, A. V. G. Chizmershya, J. Kouvetakis, and J. Menendez, *Chemistry of Materials* 24(9), 1619-1628 (2012). American Chemical Society

Introduction

Recent demonstration of AlPSi₃ films on (001) Si substrates marked the introduction of a new approach to the synthesis of (III-V)-(IV) semiconductor alloys.³³ Subsequent work showed that the relative fraction of AlP and Si in the material can be tuned, yielding (AlP)_xSi_{5-2x} alloys that span the whole range of concentrations for which the III-V elements can be accommodated in the lattice as *isolated* “donor-acceptor” pairs.³⁴ Key to these successes was the use of the (H₃Si)₃P molecule as a growth precursor. When (H₃Si)₃P combines with Al atoms generated from a Knudsen cell, it is presumed to form “Al:P(SiH₃)₃” intermediate complexes from which the (Al-P)-Si₃ tetrahedron can be incorporated intact into the growing solid by elimination of the terminal Si-H bonds.³³ An important characteristic of the (AlP)_xSi_{5-2x} system is the fact that the parent semiconductor materials AlP and Si have nearly identical lattice parameters, which facilitate the formation of the intermediate complexes and the growth of films lattice-matched to the Si substrate. The question then arises as to whether this approach can be generalized to mismatched systems in which the group-IV and III-V parent semiconductors have different lattice constants, thereby providing access to all families of (III-V)-(IV) compounds and not just those within the lattice-matched

subclass. The extension of the growth method to such alloys is not obvious, since it depends on the stability of the intermediate tetrahedral complexes and on the ability of the crystals to accommodate the expected lattice mismatch with the Si substrate. In this chapter it is shown that mismatched alloys can indeed be synthesized. The preparation of $\text{Al}(\text{As}_{1-x}\text{P}_x)\text{Si}_3$ alloys that incorporate Al-As bonds with natural lengths about 4% larger than those of Si-Si bonds is reported. This result confirms that the approach provides a route to all families of non-isovalent (III-V)(IV)₃ alloys with isolated III-V pairs, thereby opening up unanticipated materials chemistry avenues.

The first part of the section describes theoretical studies to provide insights regarding the local bonding environment in molecular building blocks and corresponding solid-state structures of the $\text{Al}(\text{As}_{1-x}\text{P}_x)\text{Si}_3$ systems. Equilibrium structures are then used to obtain the electronic properties, which show that the materials possess indirect band gaps that exhibit a small and systematic reduction in magnitude with increasing As content. The fundamental band gaps are larger than that of Si but the direct gaps are substantially smaller, indicating higher absorption in the visible range of the spectrum. The second part of the section reports detailed syntheses and characterizations of these new materials, which are grown reproducibly as single-phase monocrystalline layers directly on Si platforms, as required for applications in optoelectronics. Finally I describe experimental and theoretical Raman spectra that confirm the higher absorption coefficient of the films relative to Si, and suggest significant alloy disorder involving the randomization of the relative orientation of the isolated Al-As bonds in the crystal.

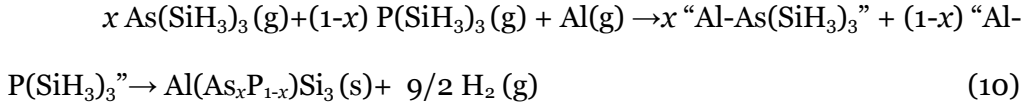
Theoretical predictions

In analogy with the successful synthesis of the $(\text{AlP})\text{Si}_3$ system, the synthesis of $(\text{AlAs})\text{Si}_3$ is expected to proceed via the interaction between gaseous $\text{As}(\text{SiH}_3)_3$ and the

supplied Al atoms to produce “AlAs(SiH₃)₃” intermediates, which in turn expel H₂ to form an AlAsSi₃ lattice with intact incorporation of the Al-AsSi₃ tetrahedron, as described by



From a solid-state perspective, both AlPSi₃ and AlAsSi₃ can be viewed as iso-structural hybrids between Si ($a = 5.431 \text{ \AA}$), and the binary AlP ($a = 5.451 \text{ \AA}$) and AlAs ($a = 5.66 \text{ \AA}$) constituents, respectively. Using Vegards’ Law,¹⁰⁷ the lattice constants of the average cubic lattices of these compounds can be estimated to be 5.435 \AA and 5.52 \AA , respectively. This range represents a $\sim 2 \%$ variation in lattice dimensions, likely to have a profound impact on the ability of the films to grow epitaxially on Si substrates. Therefore, controlling the epitaxial strain may be crucial, and the simplest approach toward this goal is to consider the formation of intermediate alloys with a general formula Al(As_{1-x}P_x)Si₃ by combining Eq. (9) with its P-analog in Ref. 33 and 34:



On the basis of the preceding synthetic scheme the atomic level structure of the resultant alloys is envisioned as a diamond-like network assembled exclusively by bonding intact Al-AsSi₃ and Al-PSi₃ tetrahedra in a manner that precludes the formation of energetically unfavorable Al-Al bonds. In this motif the As and P centers are distributed on a third nearest neighbor sublattice such that each Al-As or Al-P pair is completely coordinated by Si atoms, as shown in Fig. 18 for an ordered structural model for the Al(As_{1-x}P_x)Si₃ system.

The model was obtained by stacking 20-atom cells each containing 4 tetrahedral AlPSi₃ units (as in Ref. 33), then replacing one P center by As in each such cell to yield Al₄AsP₃Si₁₂ (e.g., AlP_{0.75}As_{0.25}Si₃). A remarkable outcome of the experiments (described

below) is that the reactions between all three co-reactants in Eq (10) proceed to completion in a highly stoichiometric manner according to their molar ratios. This underscores the great potential and generality of the approach and suggests that a broad range of new compounds could be accessed using analogous “Lewis acid-base” interactions involving group III metals and gaseous $X(YH_3)_3$ precursors where $X=(N,P,As,Sb)$ is bonded to SiH_3 and/or GeH_3 ligands ($Y=Si,Ge$).



Figure 18. Calculated ordered structure of an $AlAs_{0.25}P_{0.75}Si_3$ alloy in which the $AlPSi_3$ and $AlAsSi_3$ building units are shown as orange and purple tetrahedra, respectively (DFT estimate $a=5.484 \text{ \AA}$).

The $M(SiH_3)_3$ ($M=P,As$) precursors used in this study exhibit pyramidal geometry, which enables their lone-pair on the P/As site to readily participate in donor-acceptor reactions, as described in this study. To further explore the reaction behavior of Al with $M(SiH_3)_3$ and to gain insight into the structural changes associated with the incorporation of the corresponding “Al-M-Si₃” molecular units into the end-crystal, a

series of calculations involving the individual $M(\text{SiH}_3)_3$ reactants, the intermediate $\text{Al}:M(\text{SiH}_3)_3$ complexes, and the target AlMSi_3 crystalline products were carried out. In the case of $\text{Al}:M(\text{SiH}_3)_3$, for the sake of simplicity—and without compromising the interpretation of the results—Al is decorated with hydrogen atoms to form the hypothetical $\text{H}_3\text{Al}-M(\text{SiH}_3)_3$ adducts. These possess the inherent building units of the target solids and therefore represent ideal model compounds for my theoretical simulations.

The simulations of the molecules were performed using the *Gaussian03* code¹⁰⁴ with the 6-311G++(3df,3pd) basis set, while solid state systems were studied using the VASP code¹⁰⁸⁻¹¹⁰ which employed ultra-soft pseudopotentials with an overall energy cutoff of 400 eV for all atomic species, including As. The results in both cases are presented in Fig. 19. The top row of the figure displays the predicted molecular structures of the $\text{P}(\text{SiH}_3)_3$ and $\text{As}(\text{SiH}_3)_3$ reactant molecules. These are found to exhibit very similar geometries containing symmetrically canted silyl groups in which the apical hydrogen atoms point downwards. The calculated bond lengths and angles (in parentheses) are in good agreement with the experimental values obtained by gas electron diffraction studies of these compounds.^{111,112} The second row in the figure displays the equilibrium geometries predicted for the hypothetical molecular adducts $\text{H}_3\text{Al}-M(\text{SiH}_3)_3$. The bonding properties in this case indicate that the interaction between $M(\text{SiH}_3)_3$ and AlH_3 induces only minor deviations in the skeletal structures of the parent $\text{P}(\text{SiH}_3)_3$ and $\text{As}(\text{SiH}_3)_3$ molecules, with bond length change less than 0.01 Å. This is accompanied by a systematic “opening” of the pyramidal angles by $\sim 7^\circ$, which is presumably associated with the reduced repulsion between the bonding Si-P pairs and the lone-pair, which becomes localized in the newly formed P-Al and As-Al bonds, respectively. For the $\text{H}_3\text{Al}-\text{As}(\text{SiH}_3)_3$ adduct, the bond lengths within this molecule are

expanded by 4.1-4.5 % compared to those in the P counterpart, and the apical Si-M-Si angle is only slightly reduced ($\sim 2\%$). In both molecules the Al-M-SiH₃ cores are found to deviate significantly from regular tetrahedral structure, with edge dimensions differing by as much as $\sim 15\text{-}16\%$.

The bottom rows of Fig. 19 show the tetrahedral cores extracted from the equilibrium crystal structures of the AlPSi₃ and AlAsSi₃ phases (procedures described below). The data for AlPSi₃ solid and for the corresponding H₃Al-P(SiH₃)₃ hydride reveal that the Al-P bond length in the crystal phase (2.38 Å) is shortened relative to that in the molecular adduct (2.45 Å) while the corresponding P-Si bond become slightly longer (2.28 vs. 2.23 Å). Together these two effects lead to a regularization of the tetrahedral cores in both systems. As shown at the bottom of Fig. 19, the incorporated tetrahedra adopt nearequaledge lengths, imbuing the resulting crystal structure with a diamond-like topology. It is noted that the dimensions (edge and bond lengths) of the “As” are larger than those of their “P” counterparts by $\sim 5\%$, in analogy with the corresponding molecular trends. Furthermore, in both cases the As and P atoms are slightly displaced from their tetrahedral centers towards their respective “Si₃ base” (in contrast to elemental Si, in which all atoms are in perfect T_d coordination).

The simulation data in Fig. 19 imply that the bond lengths and tetrahedral edge dimensions of the AlAsSi₃ and AlPSi₃ molecular cores must become more regular as the molecular adduct is incorporated into the solid via elimination of the terminal H atoms. Collectively these comparisons predict a rather straightforward translation from molecule to solid, suggesting that the proposed synthetic pathways are reasonable and that “molecule-to-solid” studies may represent a valuable guide for designing similar systems in this general class of semiconductor compounds. Energetically, this concept can be formalized to describe the crystal assembly as a sum of separable, well-defined

contributions including: (i) formation energy of the “III-V-(IV-H₃)₃” precursor-intermediate, (ii) energy of H₂ abstraction to form an isolated III-V-(IV)₃ tetrahedron, (iii) bonding energy associated with interlinking individual III-V-(IV)₃ tetrahedral units, and (iv) distortion energy needed to fully relax the incorporated building blocks to their ground state.

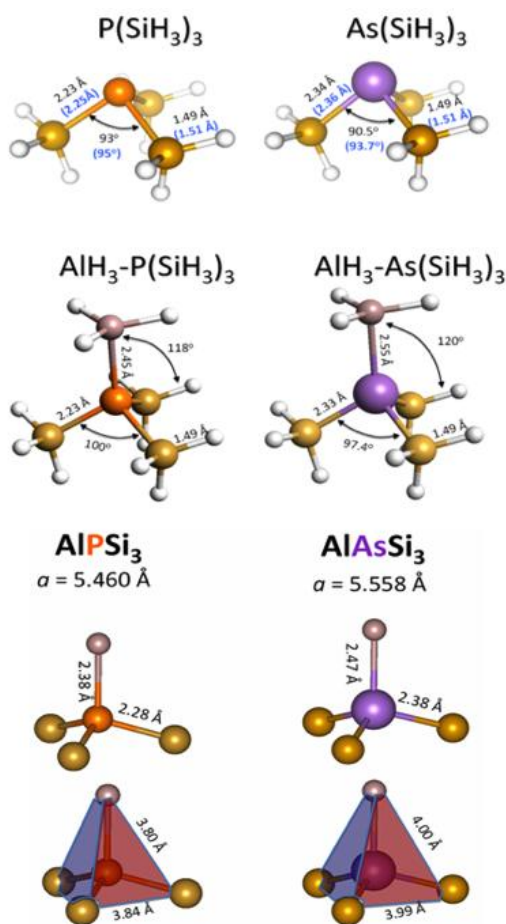


Figure 19. (top row) Equilibrium structures of $M(SiH_3)_3$ showing calculated and experimental (in parentheses) bond lengths and angles. (second row) Structures of hypothetical $AlH_3:M(SiH_3)_3$ adducts indicating that bonding of the $P(SiH_3)_3$ and $As(SiH_3)_3$ to AlH_3 induces minor departures from their parent geometries. (bottom rows) Corresponding molecular cores extracted from the equilibrium crystal structures of $AlPSi_3$ and $AlAsSi_3$ indicating regularization of the tetrahedral units. Legend Si, P, As and Al are represented by gold, orange, purple and pink spheres, respectively.

Simulations of crystal structures and their properties

In addition to providing insights with respect to local bonding in molecules and solids involved in this study, the equilibrium crystalline structure of the $\text{Al}(\text{P}_{1-x}\text{As}_x)\text{Si}_3$ alloys are also used to obtain thermodynamic and electronic properties as a by-product. To describe the crystalline systems theoretically a 20-atom cell is adopted as proposed in the original work.³³ The cell is described by the lattice parameters $\vec{a}_1 = a_0(\frac{3}{2}, -\frac{1}{2}, 0)$, $\vec{a}_2 = a_0(\frac{1}{2}, \frac{3}{2}, 0)$ and $\vec{a}_3 = a_0(0, 0, 1)$, where the Cartesian components are aligned with the conventional cubic (100), (010) and (001) directions in the parent diamond cubic lattice. This setting accommodates four tetrahedral III-V-Si₃ building units with the central Group-V atoms at fractional positions $U = (0, 0, 0)$, $U' = (0, \frac{1}{2}, \frac{1}{4})$, $U'' = (\frac{1}{2}, 0, \frac{3}{4})$ and $U''' = (\frac{1}{2}, \frac{1}{2}, \frac{1}{2})$. The corresponding neighboring atoms of each of these U atoms are then designated V_n, V'_n, V''_n and V'''_n where $n=1, \dots, 4$. A structural diagram of the unit cell and all of the atomic coordinates is provided in Figure 20. Here the isolated III-V pairs are described by placing a Group V atom (in this case As) on each U position, and a group III atom (in this case Al) on one of the associated V_n sites. This represents a general procedure for building (III-V)-(IV)₃ crystal structures containing isolated III-V pairs. The constraint of avoiding direct Al-Al bonds then limits the number of possibilities, which can nevertheless now be designated using configurations based on the lattice description. For example, the ground state structure in which all III-V pairs are oriented in the same direction is described by placing Group III atoms on $\{V_1, V'_1, V''_1, V'''_1\}$ positions. In general the atomic positions in the ground state structures of $\text{Al}(\text{P}_{1-x}\text{As}_x)\text{Si}_3$ are found to deviate only slightly from the ideal diamond-lattice values given in Figure 20.

For the AlAsSi_3 compound the ground state structure cell parameters $a_1 = 8.710 \text{ \AA}$, $a_2 = 8.691 \text{ \AA}$ and $a_3 = 5.537 \text{ \AA}$, and cell angles $\alpha = \beta = 90^\circ$ and $\gamma = 90.24^\circ$. The basal dimensions a_1 and a_2 in this monoclinic setting differ by $\sim 0.22\%$, representing a slight asymmetry which is due entirely to the bias in the cell shape induced by the highly

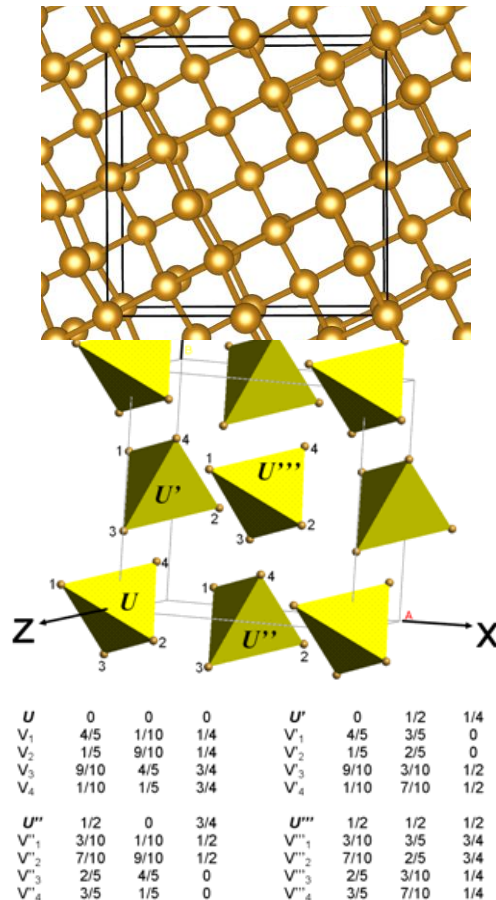


Figure 20. Structural models and specification of atomic positions for the 20-atom unit cell of III-V-IV₃ compounds. As shown in the middle panel the III-V pairs are placed on the lattice with Group-V atoms located on the U-sites, and Group-III atoms chosen from among the corresponding neighboring V_n positions, with Group-IV atoms occupying all remaining lattice positions. In this representation the ground state structure of AlAsSi_3 has Al atoms at $\{V_1, V'_1, V''_1, V'''_1\}$ corresponding to 1,1,1,1 atoms in the polyhedral model.

ordered arrangement of AlAsSi_3 units. A nominal *tetragonal* structure is then obtained by averaging the basal dimensions to yield $a_0^T = 8.700 \text{ \AA}$ and $c_0^T = c_0 = 5.537 \text{ \AA}$, and a c/a ratio of 0.6381. This latter value differs slightly from the ideal value $\sqrt{\frac{2}{5}} = 0.6326$ obtained for a diamond lattice with cell dimensions $\sqrt{\frac{5}{2}} a \times \sqrt{\frac{5}{2}} a \times a$. For example, the equivalent crystallographic value for the basal plane dimension, referenced to a silicon lattice, is $a_0^T / \sqrt{\frac{5}{2}} = 5.514 \text{ \AA}$. Adding 0.8% of this value to account for LDA's underestimate then gives a predicted value of 5.558 \AA . This is slightly larger than the value 5.52 \AA estimated from Vegard's Law assuming a linear interpolation between the lattice parameters of the end members Si_3 and AlAs .

10-atom cell description

Among the large number of ordered structures obtained by permuting the Al atoms in the available sites, the lowest energy ones (including the ground state *C1c1* structure) often possess the highest symmetry. Accordingly a 10-atom primitive cell setting derived from the cubic diamond lattice using lattice vectors $\vec{a}_1 = a_0(1,0,0)$, $\vec{a}_2 = a_0\sqrt{\frac{3}{2}}\left(\sqrt{\frac{1}{6}}, \sqrt{\frac{3}{2}}, \frac{1}{2\sqrt{3}}\right)$, and $\vec{a}_3 = a_0\left(\sqrt{\frac{3}{2}} * \sqrt{\frac{1}{6}}, -\frac{1}{2\sqrt{3}}, \sqrt{\frac{3}{2}}\right)$ is described. (Fig. 21) Here, as in the case of the 20-atom cell, the Cartesian components are aligned with the conventional cubic (100), (010) and (001) directions in the parent crystal, respectively, facilitating a systematic comparison of calculated and observed Raman spectra (described below).

For AlAsSi_3 this setting accommodates two tetrahedral Al-As- Si_3 building units with the central As in fractional positions $U = (11/20, 3/10, 1/10)$ and $U' = (4/5, 4/5, 3/5)$, and the neighboring atoms at $V_n = \{(3/5, 3/5, 1/5), (0, 0, 0), (2/5, 2/5, 4/5), (1/5, 1/5, 2/5)\}$

and $V'_n = \{(3/4, 1/2, 1/2), (19/20, 7/10, 9/10), (3/20, 9/10, 3/10), (7/20, 1/10, 7/10)\}$, respectively, where $n=1, \dots, 4$, as shown in Fig. 21.

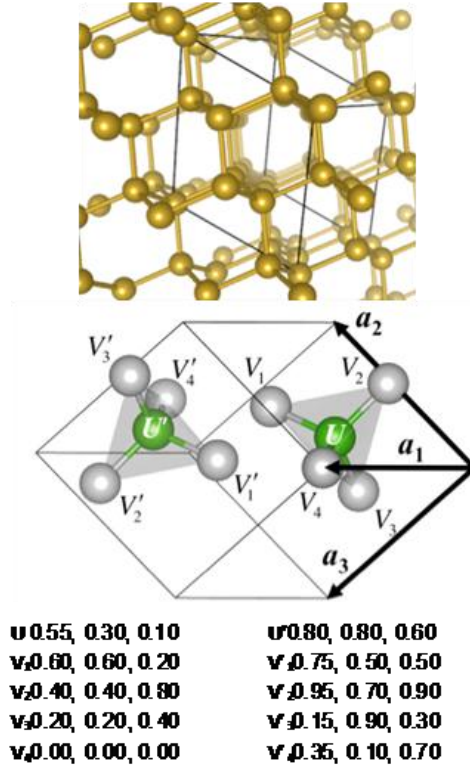


Figure 21. (top) Silicon lattice with lines designating the monoclinic 10-atom ($C1c1$) representation containing two III-V-(IV)₃ units (green tetrahedral, central panel). Atomic coordinates are listed in the adjoining table, where U, U' designate group-V atom positions and the $\{V_k\}$, and $\{V'_k\}$ sites represent the group III/group IV atom positions. Note: For clarity, the origin has been shifted so that the tetrahedral units appear within the cell as drawn.

The optimized ground state structure cell parameters are found to be $a_1 = 5.537 \text{ \AA}$, $a_2 = 6.736 \text{ \AA}$, $a_3 = 6.758 \text{ \AA}$, $\alpha = 80.42^\circ$, $\beta = 65.827^\circ$ and $\gamma = 65.729^\circ$. Here the Al atoms are located at sites V^1 and V^4 , and resulting crystal has energy $\sim 1\text{-}2 \text{ meV/atom}$ below that of the weighted sum of elemental constituents (FCC Al, hexagonal As, and diamond silicon) while a second ordered phase with only slightly higher energy ($\sim 38 \text{ meV/atom}$) is

obtained by placing Al atoms on sites V_1 and V_3' (structures with intermediate energies been identified in supercells which allow a symmetry reduction).

Band Structure Calculations

The latter 10-atom primitive cell was next used to carry out a series of systematic band structure calculations for the AlPSi_3 , AlAsSi_3 end members as well as the intermediate alloy represented by $\text{Al}(\text{As}_{0.5}\text{P}_{0.5})\text{Si}_3$. The FPLAPW ELK code¹¹³ was used to calculate the LDA electronic structure with an $8 \times 8 \times 8$ k -point grid and an RK_{max} parameter of 10. Well-converged static lattice structures, with residual forces < 0.01 eV/Å and cell stress < 0.01 kbar, were employed in all cases. For the $\text{Al}(\text{P}_{0.5}\text{As}_{0.5})\text{Si}_3$ system the P and As atoms each occupy the U and U' positions, respectively, while the Al atoms were placed on V_3 and V_4 sites. Figure 22 compares the electronic band structure of AlAsSi_3 with silicon, as a reference, in a common base-centered monoclinic setting.

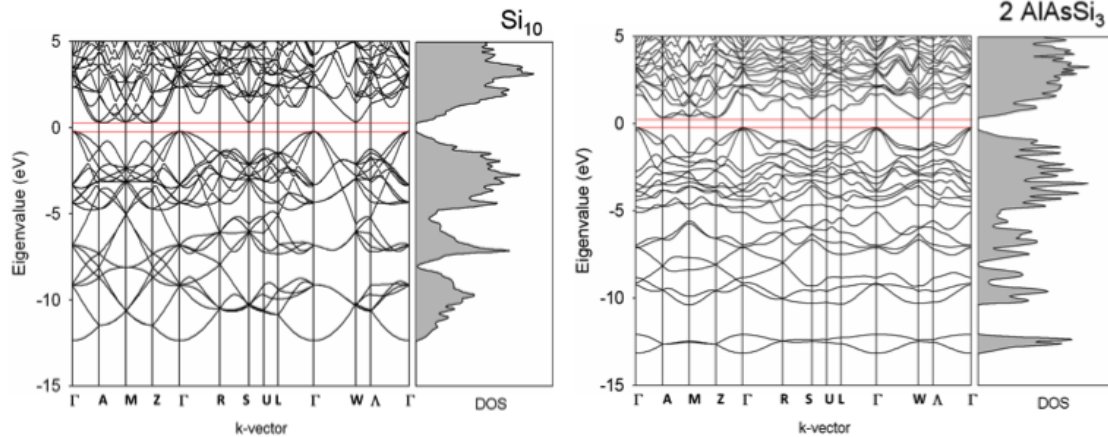


Figure 22. Comparison of the band structure of Silicon (Si_{10}) and AlAsSi_3 using a common 10-atom base-centered monoclinic setting, indicating similarity in the band widths and magnitude of the band gaps.

In the case of silicon the 40 valence electrons occupy 20 bands and yield the classic density of states, an indirect LDA band gap of ~ 0.58 eV and a direct band gap at

the Γ -point of 2.55 eV, as expected. A close inspection of the bottom of the conduction band indicates that the minimum occurs in the vicinity of the Z point $\vec{k}_Z = (\frac{2\pi}{a})(0,0,\frac{1}{\sqrt{5}})$ in the Brillouin zone of the monoclinic cell, which by comparison corresponds to the minimum close to the X-point in the Brillouin zone of the conventional 2-atom rhombohedral primitive cell of Si. In this context, prior work using explicit LDA band structure calculations demonstrated that the nature of the band gap in the AlPSi_3 end-member is very similar to that of Si. Here the study is extended to the corresponding band structure of $\text{Al}(\text{As}_x\text{P}_{1-x})\text{Si}_3$ systems as shown below in Fig. 23, which indicates a small but systematic reduction in the magnitude of the band gap in going from pure AlPSi_3 to pure AlAsSi_3 , via the intermediate $\text{Al}(\text{P}_{0.5}\text{As}_{0.5})\text{Si}_3$ alloy.

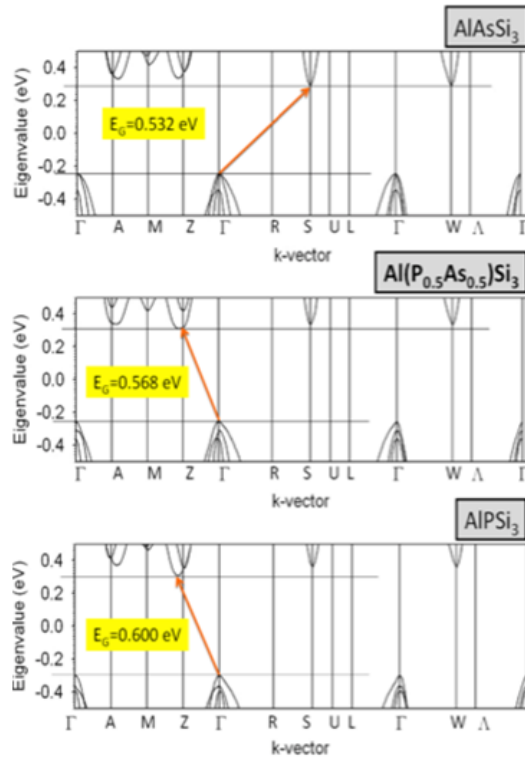


Figure 23. Band structure plots for AlPSi_3 , $\text{Al}(\text{P}_{0.5}\text{As}_{0.5})\text{Si}_3$ and AlAsSi_3 in the band gap region indicating: (i) $\sim 11\%$ reduction in the band gap magnitude ($\text{AlPSi}_3 \rightarrow \text{AlAsSi}_3$), (ii) negligible bowing and (iii) indirect band gap character determined by P/As ratio.

The band gap in the 50% alloy (0.568 eV) was found to be essentially equal to the Vegard average (0.566 eV) of the corresponding values for AlPSi_3 and AlAsSi_3 (see Fig 23) suggesting that the bowing in this system is very small. Perhaps most importantly, the calculations indicate that the band gap is indirect for all three systems shown. However, while both AlPSi_3 and the $\text{Al}(\text{P}_{0.5}\text{As}_{0.5})\text{Si}_3$ alloy exhibit indirect $\Gamma \rightarrow Z$ gap character similar to that in Silicon, the corresponding transition in the AlAsSi_3 system is found to occur between $\Gamma \rightarrow S$, where the S-point is given explicitly by $\vec{K}_S = (2\pi/a)((2/(3\sqrt{5}), -(1/\sqrt{5}), (1/\sqrt{5}))$. This asymmetrical behavior in composition, which favors the influence of P, is consistent with the stronger bonds in the AlPSi_3 end-member.

In contrast with the indirect gap values, which relative to Si change very modestly in the $\text{Al}(\text{As}_{1-x}\text{P}_x)\text{Si}_3$ and $(\text{AlP})_y\text{Si}_{5-2y}$ systems, the direct gaps are significantly reduced following the incorporation of the III-V pairs, and more so in the case of the As-compounds. For example, in AlPSi_3 the direct gap at the Γ -point is lowered by 0.32 eV relative to Si. Substituting half of the P atoms by As atoms, gives a further lowering of 0.15 eV. Finally, the direct gap at Γ for AlAsSi_3 is calculated to be 0.67 eV below that of Si. Since the spectral dependence of the absorption coefficient is largely determined by the energy of the direct gap transitions, these materials are expected to have a higher absorption coefficient than that of Si over the visible range. It is well known that the poor Si absorption in this range is a key limiting factor in Si-based solar cells. The availability of Si-compatible materials with increased absorption may thus have applications in photovoltaics.

It is emphasized that the outcome and interpretation of the band structure calculations is based on ordered ground state structures, while the actual systems likely exhibit deviations from this idealization and may even include a mixture

of accessible metastable configurations. The effects of such configurational disorder will be systematically incorporated in subsequent work by appropriate cluster averaging over a number of energetically competitive structures at each composition, as has been done in previous work on semiconductor systems.¹¹⁴ Finally, while the local density approximation adopted in the DFT calculations severely underestimates the magnitude of the band gaps, the change in character of the indirect band gaps induced by alloying between P and As is expected to be qualitatively correct.

Experimental procedure

The incorporation of As into the (III-V)(IV)₃ alloy was pursued via reactions of gaseous As(SiH₃)₃ and Al atoms. The As(SiH₃)₃ precursor is a stable liquid with a nominal vapor pressure of 10 Torr at 22 °C, well suited for film growth under low-pressure Chemical Vapor Deposition(CVD) conditions. High purity samples of the compound were synthesized at ~ 40% yield via stoichiometric reactions of BrSiH₃ and Li₃As in diethyl ether following a slightly modified literature method.¹¹⁵ The Li₃As starting material was obtained by direct solid-state combinations of finely ground As powder samples and Li ribbons under an atmosphere of He at 475 °C. The As(SiH₃)₃ product was separated from the solvent and the solid residues via fractional distillation, and it was subsequently purified to remove any remaining traces of BrSiH₃ contaminants. The identity of the compound was confirmed by gas-phase infrared absorption and its purity was established by ¹H-Nuclear Magnetic Resonance (NMR)spectroscopy. For the mixed alloy containing As and P atoms I used the P(SiH₃)₃ compound described in Refs. 33 and 34.

The films growth was conducted using gas-source Molecular Beam Epitaxy techniques in an Ultra-High Vacuum (UHV) CVD chamber equipped with a solid source of high purity aluminum. Prior to growth, the Si wafers underwent cleaning and chemical

etching and were then inserted into the reactor via a load-lock. The chamber was pumped to 10^{-10} Torr, and the wafers were flashed on the deposition stage at 1100 °C for 10 seconds to obtain an oxide-free surface.

The properties of the grown films were characterized by Rutherford Backscattering (RBS), cross-sectional transmission electron microscopy (XTEM), and high-resolution x-ray diffraction (HR-XRD). Raman spectroscopy was used to study the vibrational properties, and, indirectly via simulations, the microscopy atomic distribution.

Synthesis and structural characterization of AlAsSi₃

The growth of AlAsSi₃ was conducted at $P = 10^{-5}$ Torr and $T = 490-500$ °C . The As(SiH₃)₃ reservoir was attached to an injection manifold that was differentially pumped to 10^{-9} Torr. The flow of the source vapor into the reactor was regulated by a high precision needle valve. The crystal nucleation was initiated by introducing the As(SiH₃)₃ and the Al co-reactants onto the wafer surface at a molar ratio of ~1:1 and a constant flux/flow rate throughout the 1-2 hour duration of the experiments.

The RBS spectrum of a representative film is shown in Fig. 24. It reveals strong and distinct peaks corresponding to the Al, Si and As atoms. Spectral fits for this and other samples yield thicknesses between 40 nm and 600 nm depending on the growth conditions. The Si:As molar ratio from the fits is approximately 3:1, indicating that the entire AsSi₃ molecular core of the precursor is incorporated into the film. The Al/As ratio is 1.0 - 0.95, consistent with the expected AlAsSi₃ stoichiometry.

XTEM indicates the formation of single-phase, monocrystalline layers. The representative bright field image in Fig. 24 shows significant levels of threading defects and shallow surface undulations whose lateral scale coincides with that of imperfections located at the termination of the stacking defects at the film surface. The high-resolution

image of the interface region (inset in Fig. 24) displays a near-perfect commensuration of the {111}-type lattice fringes of the substrate and the epilayer, indicating a high degree of epitaxial alignment. Corresponding electron diffraction patterns confirm that the two materials are essentially isostructural and possess diamond-like symmetry. No evidence of ALAs precipitation was found in the electron micrographs or diffraction patterns. This is further verified by RBS channeling, which shows that the ratio of the aligned over random peak height (χ_{\min}) for Al, Si and As signals are consistently identical, indicating complete substitution of the three types of atoms in the same tetrahedral lattice.

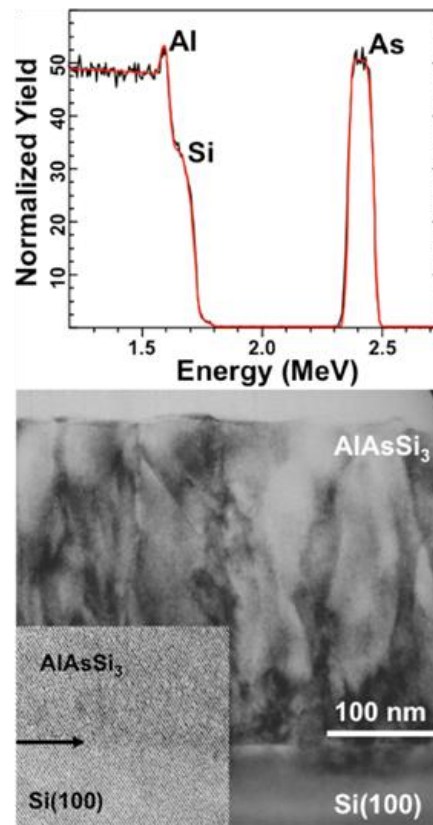


Figure 24. (top) RBS spectra (black trace) of Si/As/Al films showing well separated As, Si and Al signals. The red line corresponds to the fit of the 2 MeV data yielding an average composition of AlAsSi₃ and a thickness of 260 nm. (bottom) XTEM micrograph of the entire AlAsSi₃ layer thickness. The film is mono-crystalline, fairly uniform and exhibits threading defects penetrating to the surface. (Inset) High resolution image of the AlAsSi₃/Si(100) interface showing near perfect epitaxial alignment between the film and Si.

HR-XRD shows strain relaxation correlated with the presence of threading dislocations. For the thinnest films ($t < 40$ nm) both the on-axis (004) and off-axis (224) and (-224) plots reveal a single peak corresponding to a tetragonally distorted diamond-like lattice with $c = 5.581$ Å and $a=b = 5.45$ Å. The similarity of the in-plane lattice constant to the lattice parameter of Si ($a_0 = 5.431$ Å) suggests that the film is approaching a fully lattice-matched condition with the substrate. Using a weighted average of the AlAs and Si elastic constants, I obtain for the film a relaxed lattice parameter $a_0 = 5.52$ Å, in excellent agreement with the Vegard average of AlAs and Si.¹¹⁶ This implies an epitaxial strain of -1.3%. As the film thickness is increased, I see (Fig. 25) evidence for two distinct regions, consisting of an initiation layer with strain characteristics similar to the thinnest films followed by a second bulk region whose compressive strain state decreases systematically as a function of the overall thickness.

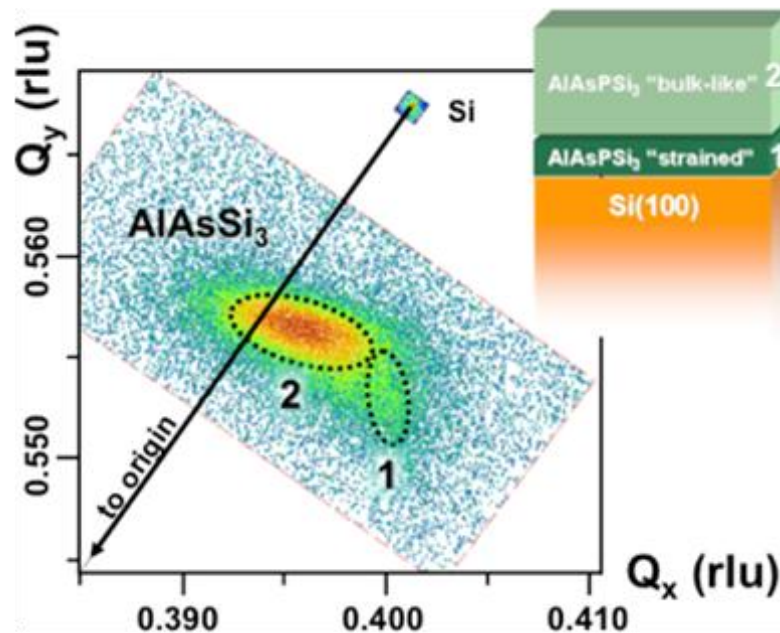


Figure 25. 224 XRD maps of the 260 nm thick AlAsSi₃ sample described in the XTEM image of Figure 24. The strong and weak peaks labeled “1” and “2” denote interface and bulk-like layers as shown in the schematic (top right). The corresponding lattice parameters are $a_1 = 5.47$ Å, $c_1 = 5.57$ Å and $a_2 = 5.501$ Å, $c_2 = 5.54$ Å yielding nearly identical relaxed values of $a_{01} = 5.52$ Å and $a_{02} = 5.52$ Å, respectively, as expected owing to their common stoichiometry.

For layers with $t \sim 100$ nm the XRD plots reveal distinct pairs of closely spaced 004, 224 and -224 peaks. A calculation of the *relaxed* lattice constant a_0 for the two regions yields the same value, consistent with a common AlAsSi₃ stoichiometry. As the film thickness is further increased into the 260-600 nm range, the bulk region peaks become progressively stronger and monotonically converge toward fully relaxed values. The corresponding peaks for the interface region remain largely unchanged, indicating that this portion of the film retains its original strain state and thickness. The strain state of the film produced by this bimodal growth mechanism remains thermally robust upon annealing at 650-700 °C.

The critical thickness for strain relaxation in my AlAsSi₃/Si heterostructure appears to be quite similar to the value found for the thoroughly investigated Si_{1-x}Ge_x/Si interface. In the latter, the equilibrium critical thickness is about 8 nm for epitaxial strains on the order of 1.3%, but for growth at 500 °C metastable critical thicknesses around 70 nm are predicted and observed experimentally.^{117,118} If the mismatch strain is reduced in half by decreasing the Ge concentration, the metastable critical thickness increases to about 300 nm.¹¹⁸

Synthesis and structural characterization of Al(As_{1-x}P_x)Si₃ alloys

As indicated above, a possible way to reduce the lattice mismatch of the AlAsSi₃ system with the Si substrate is the partial substitution of As by P. The synthesis of Al(As_{1-x}P_x)Si₃ alloys is conducted by reactions of the (H₃Si)₃P and (H₃Si)₃As precursors with Al atoms, according to Eq. (10). Thus the As/P ratio can be controlled by varying the relative fraction of the gaseous sources. As a first approximation, the P(SiH₃)₃ and As(SiH₃)₃ co-reactants are mixed at a ratio close to that of the target P/As content in the solid product. This is actually borne out in practice, where I find that a 3:1 ratio of P(SiH₃)₃ / As(SiH₃)₃ reacts directly with Al at 475-500 °C to give an alloy with

composition $\text{Al}(\text{P}_{0.75}\text{As}_{0.25})\text{Si}_3$, as determined from RBS. Similarly, a 1:1 ratio of the corresponding precursors produces an $\text{Al}(\text{P}_{0.45}\text{As}_{0.55})\text{Si}_3$ alloy. RBS ion channeling also indicated a high degree of epitaxial alignment confirming the full substitutability of the constituent atoms in the same diamond-like lattice, consistent with mono-crystalline single-phase character, as shown in Figure 26 for the $\text{Al}(\text{P}_{0.45}\text{As}_{0.55})\text{Si}_3$ material. The RBS thicknesses of the samples produced in this study are between 100-200 nm, so that I might expect fully strained films if the analogy with the $\text{Si}_{1-x}\text{Ge}_x/\text{Si}$ system continues to hold. This is fully confirmed by HR-XRD measurements.

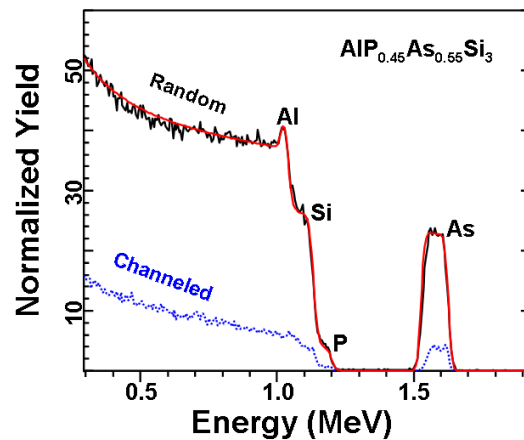


Figure 26 Random (black trace) and aligned (blue trace) RBS spectra of an alloy sample acquired at 2 MeV showing that the signals of Al, Si, P and As exhibit the same degree of channeling indicating single phase material. The fit of the data (red trace) yields a thickness of 160 nm and an alloy composition of $\text{AlP}_{0.45}\text{As}_{0.55}\text{Si}_3$.

Figure 27 shows on- and off-axis spectra of a representative $\text{AlP}_{0.75}\text{As}_{0.25}\text{Si}_3$ film. The θ - 2θ plots contain 004 peaks with remarkably narrow profiles similar to those of the underlying Si. The thickness fringes near the base line indicate the presence of a highly registered and crystalline overlayer. The 224 diffraction maps of the alloy and the substrate exhibit virtually identical shape and intensity distributions. The exact vertical alignment observed between the film and substrate 224 maxima is consistent with a perfect in-plane lattice matching. The c -values of the tetragonal unit cell are 5.484 Å for

AlP_{0.75}As_{0.25}Si₃ and 5.530 Å for AlP_{0.45}As_{0.55}Si₃. Using weighted averages of the elastic constants of AlP, AlAs, and Si,¹¹⁶I compute relaxed lattice parameters $a_0 = 5.455$ Å and 5.476 Å, respectively, in excellent agreement with the Vegard averages of AlP, AlAs, and Si.

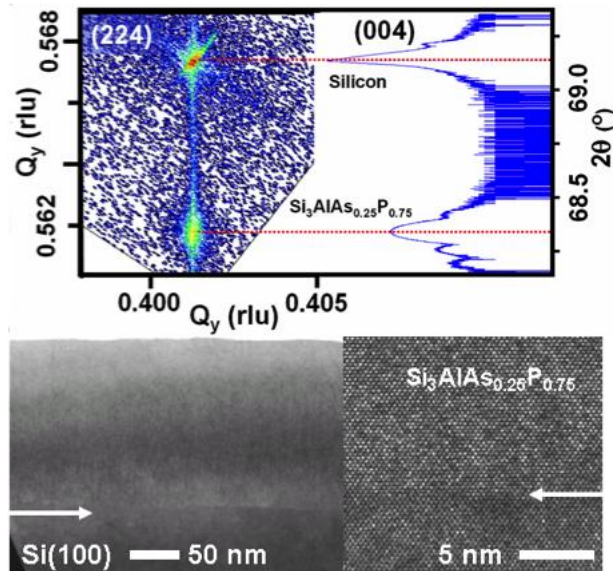


Figure 27. (top): XRD plots of Si₃AlAs_{0.25}P_{0.75}/Si(100). The (224) reciprocal space maps at left show that the alloy peak is vertically aligned with that of the substrate, indicating in-plane lattice matching between the fully compressive epilayer and Si(100). The corresponding (004) 2θ plot (far right) confirms the high crystalline quality of the epilayer. (bottom): XTEM micrograph of Si₃AlAs_{0.25}P_{0.75}/Si(100) sample (at left) showing a uniform and flat layer largely devoid of threading defects. The high resolution image of the interface region (at right) reveals a flawless epitaxial registry.

Further structural analysis was performed by XTEM. The micrograph in Figure 27 shows the typical microstructure across the entire film thickness of a Si₃AlAs_{0.25}P_{0.75}/Si(100) sample. Note that the film surface is smooth and continuous and the bulk material is devoid of threading defects within fields of view (typically 2 μm). The high resolution image of the interface region shows seamless commensuration with no indication of misfit dislocations in spite of the relatively large mismatch. This

observation is consistent with the presence of full pseudomorphic growth as determined by HR-XRD. The lack of defects and the tendency to strain match in this diffusion limited growth regime can be rationalized with epitaxial stabilization achieved by incorporation of excess Si bonds at the interface. This behavior is attributed to the unique low temperature protocols afforded by the specifically designed chemistry employed.

Raman studies

Vibrational spectroscopy can provide insight into the atomic distribution within the material. Figure 28 shows Raman spectra from a 600-nm AlAsSi₃ film and a 150-nm AlP_{0.45}As_{0.55}Si₃ film. The data were collected at room temperature using a 532-nm laser excitation source. The Si substrate Raman line is visible as a very narrow peak at 520 cm⁻¹ in the AlAsSi₃ spectrum. The substrate signal attenuation implies a film absorption coefficient $\alpha \sim 4 \times 10^4 \text{ cm}^{-1}$ at 2.3 eV, about four times larger than that of bulk Si.¹¹⁹ This is qualitatively consistent with the theoretical band structure predictions, which indicate lower direct gap transitions for this material relative to Si. The substrate signal is much stronger for the thin AlP_{0.45}As_{0.55}Si₃ film, and it was subtracted from the spectrum to display the film vibrational modes. The film spectra consist of a main peak near 500 cm⁻¹ and an additional weaker structure around 370 cm⁻¹. The high-frequency main peak is assigned to Si-Si optical vibrations with displacement patterns similar to those of the zone-center optical mode in pure Si. The second peak at $\sim 370 \text{ cm}^{-1}$ has a frequency intermediate between the TO and LO modes in bulk AlAs.¹²⁰ Since this peak is not observed in (AlP)_xSi_{5-2x} alloys, it seems natural to assign it to stretching, optic-like vibrations involving the Al-As pairs.

To gain insight into the mode assignments Raman spectra as an average of the lowest-energy crystalline structures discussed in the theoretical section were computed.

The highly converged ground-state discussed in the theoretical section were employed in Γ -point density-functional-perturbation-theory (DFPT) phonon calculations,¹²¹ which used standard pseudopotentials supplied with the CASTEP package, a cutoff energy of 700 eV and a Γ -centered k -point grid with a spacing of 0.05 \AA^{-1} .

The solid and dotted lines in the bottom panel of Figure 28 show the average of the Raman spectra for the ground state structure in Fig. 21 and the next higher energy structure (with the Al atoms at sites $V_2, V'_2, V''_4,$ and V'''_4 using the notation of Figure 20) for AlAsSi_3 and $\text{AlAs}_{0.5}\text{P}_{0.5}\text{Si}_3$, respectively. The theoretical frequencies are rigidly upshifted by 7 cm^{-1} to match the calculated and experimental Raman frequencies in pure Si, and an additional strain correction is added using the pure Si strain shift coefficient from Ref.122. Raman intensities were computed using a bond polarizability model with Si-Si bond polarizability parameters taken from Go *et al.*¹²³ The Al-As bond polarizabilities were set equal to those of Si times the ratio (7.8/11.9) of the dielectric constant ϵ_∞ of both materials,¹²⁴ and the Si-Al and Si-As polarizabilities were approximated as the average of the other two. The spectra were averaged over all possible orientations of the two crystals compatible with (001) epitaxy on Si. The resulting Raman spectra were convoluted with a Gaussian with full-width at half maximum (FWHM) of 6 cm^{-1} .

The high-energy peaks in the theoretical calculations correspond to Si-Si-like modes. Their predicted frequency shifts relative to bulk Si are in reasonably good agreement with experiment. The theoretical spectra also reproduce the secondary low-energy peaks and their weaker strength in the $\text{AlP}_{0.45}\text{As}_{0.55}\text{Si}_3$ alloy, but the peaks are upshifted by about 40 cm^{-1} relative to the experiment, which is beyond the accuracy of the *ab initio* method. An examination of displacement pattern reveals that modes with the largest amplitude of Al-As bond stretching have frequencies over the grey band in

Fig. 28, much closer to the experimental peaks, whereas the theoretical Raman peaks just above 400 cm^{-1} arise from modes with large Si-displacements that are reminiscent of the Si-Ge Raman mode in $\text{Si}_{1-x}\text{Ge}_x$ alloys. In these alloys the Si-Ge mode also appears at a frequency near 400 cm^{-1} .¹²⁵The theoretical Raman modes have similar frequencies due to the comparable As/Ge and Al/Si masses.

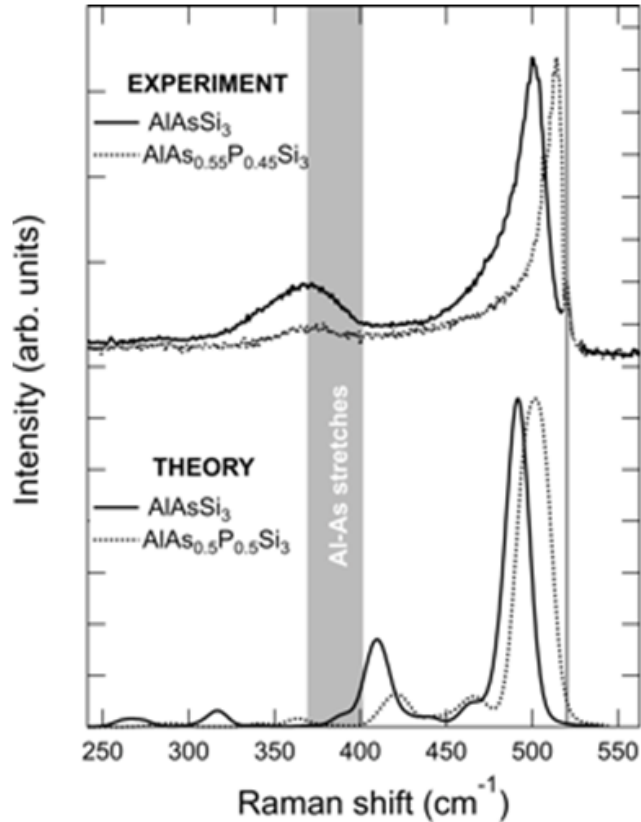


Figure 28. Experimental and theoretical Raman spectra for AlAsSi_3 and $\text{Al}(\text{As}_{1-x}\text{P}_x)\text{Si}_3$.

The scattering configuration is $z^{(x,y)}\bar{z}$ in the Porto notation, where x, y, z refer to the cubic axes in the underlying Si substrate. The grey band spans the range of the theoretical Al-As bond stretching frequencies in both materials. The vertical line on the right corresponds to the Raman frequency in bulk Si.

The discrepancies between observed and calculated spectra suggest that alloy disorder contributes substantially to the observed peaks at $\sim 370 \text{ cm}^{-1}$. The simplest form of disorder involves the randomization of the relative orientation of the Al-As bonds.

The vibrational properties of the resulting random alloys can be studied theoretically using supercell calculations. These are beyond the scope of the present work, but my preliminary observations suggest that the spectroscopy of modes in the $350\text{ cm}^{-1} - 450\text{ cm}^{-1}$ range can generate valuable information on the structure of $\text{Al}(\text{As}_{1-x}\text{P}_x)\text{Si}_3$ alloys at the nanoscale level. In the case of the $\text{AlP}_{0.45}\text{As}_{0.55}\text{Si}_3$ alloys, the simulations assume perfect alternance between the As- and P-centered tetrahedra, but the growth method suggests that this is very unrealistic, and that the tetrahedra are more likely to be distributed at random. Thus, the $\text{AlP}_{0.45}\text{As}_{0.55}\text{Si}_3$ alloy Raman spectrum should be closer to an average of the AlPSi_3 and AlAsSi_3 Raman spectra. This is actually suggested by the experimental data, where the main effect seen, aside from the shift of the Si-Si line, is a reduction in intensity but not a shift of the $\sim 370\text{ cm}^{-1}$ feature.

Conclusion

In summary, it has been demonstrated that the method introduced in Ref. 33 to synthesize $(\text{AlP})_x\text{Si}_{5-2x}$ alloys can be generalized to additional families of (III-V)-(IV) semiconductor alloys in which the III-V and group-IV components have very different bond lengths. In addition to their intrinsic relevance for a host of applications, alloys containing elements with masses very different from that of Si have a rich vibrational structure that can be detected spectroscopically and provide important information on the nanostructure of these novel materials.

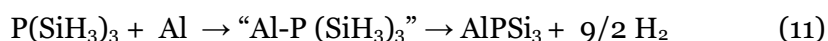
Chapter 7

QUANTUM CHEMICAL SIMULATIONS ON THE STRUCTURE, BONDING , AND REACTIVITIES OF (IV)₃M PRECURSORS AND THE THERMODYNAMICS OF CORRESPONDING (III-V)IV SOLID STRUCTURES

Reprinted with permission from “Monocrystalline Al(As_{1-x}N_x)Si₃ and Al(P_{1-x}N_x)Si_{5-2y} alloys with diamond-like structures: New chemical approaches to semiconductors lattice matched to Si” ; J. Kouvetakis, A. V. G. Chizmeshya, L. Jiang, T. Watkins, G. Grzybowski, R. T. Beeler, C. Poweleit, and J. Menéndez, Chemistry of Materials 24, 3219 (2012) American Chemical Society

Introduction

Recently an entirely new approach was introduced to the synthesis of (III-V)-(IV) materials that is specifically designed to avoid phase separation. As an initial proof of concept, it was demonstrated by the growth of AlPSi₃ on Si (100) substrates according to³³



At higher temperatures, the decomposition of the P(SiH₃)₃ compound induces the incorporation of excess Si, yielding alloys of the form (AlP)_ySi_{5-2y} with $y < 1$.³⁴ As mentioned in the previous chapter, the first attempt at generalizing the above approach focused on the substitution of P by As. This was a natural choice based on chemical compatibility and availability of the As(SiH₃)₃ analog to P(SiH₃)₃. This work led to the successful demonstration of AlAsSi₃ layers on Si using similar reaction pathways and deposition protocols to those employed in the original studies on AlPSi₃ (Ref.33). The AlAsSi₃ compound contains Al-As bond with natural lengths about 4% larger than those

in Si. Accordingly, relatively large epitaxial strains—as large as $\sim 1.7\%$ —are expected on the basis of Vegard’s Law. This significant misfit strain leads to a bimodal growth mechanism in which a thin (~ 40 nm), initiation layer is formed which provides a template for the subsequent bulk-like crystal growth. The lattice mismatch between AlAsSi₃ and Si can be mitigated via intermediate Al(As_{1-x}P_x)Si₃ alloys, which were obtained using straightforward stoichiometric combinations of the corresponding As(SiH₃)₃ and P(SiH₃)₃ precursors.³⁵ However, since the cubic average lattice constant of AlPSi₃ is slightly larger than that of Si, the mismatch strain with the substrate can never be completely eliminated within this system, potentially leading to significant strain management issues in applications that require thick layers, such as photovoltaics. Accordingly, the substitution of arsenic and phosphorus by the markedly smaller nitrogen can, in principle, lead to perfect lattice matching with Si, while maintaining—and even enhancing—the flexibility to tailor the electronic properties. Using literature lattice parameter data for cubic AlN ($a = 4.38$ Å), AlAs ($a = 5.66$ Å), and Si ($a = 5.431$ Å),^{126,127} I estimate on the basis of Vegard’s law that the lattice constants of Al(As_{1-x}N_x)Si₃ should decrease from 5.52 Å for $x = 0$ (e.g., pure AlAsSi₃), to 5.431 Å (e.g., silicon lattice match) for a nitrogen content corresponding to $x \sim 0.18$. In the case of AlPSi₃ the misfit is considerably smaller and thus only $\sim 3-4\%$ nitrogen is sufficient to achieve the same balance. The formation of AlP_{1-x}N_xSi₃ perfectly lattice matched to Si might be important for Si-based multijunction solar cells. Moreover, the incorporation of N may provide the means to introduce significant changes in the electronic structure.

In this context I note that the substitutional incorporation of N into dimensionally disparate III-V materials such as GaAs(N) and InGaAs(N) has been pursued for the past 10 years precisely because of the dramatic N “impurity”-induced bowing of the direct gap and the potential applications of this effect in

photovoltaics.¹²⁸The strain-minimized $\text{Al}(\text{As}_{1-x}\text{N}_x)\text{Si}_3$ and $\text{Al}(\text{P}_{1-x}\text{N}_x)\text{Si}_3$ materials are created via reactions of Al atoms with appropriate mixtures of either $\text{As}(\text{SiH}_3)_3$ or $\text{P}(\text{SiH}_3)_3$, and their planar $\text{N}(\text{SiH}_3)_3$ analog.³⁶ While the PSi_3 and AsSi_3 cores in these molecules are inherently pyramidal, the NSi_3 core is planar and far less reactive toward nucleophilic attack. Nevertheless, it was shown that under appropriate conditions the $\text{N}(\text{SiH}_3)_3$ compound reacts with Al to form trigonal prismatic intermediates which can then be readily inserted into the structure as intact NSi_3 , leading to significant incorporation of N into $\text{Al}(\text{As}_{1-x}\text{N}_x)\text{Si}_3$. These notions are corroborated by detailed quantum chemical calculations, which are used to study the reactivity of the silyl precursors on the basis of their electrostatic and electron density maps, as well as their energies. The molecular calculations are then combined with solid-state simulations to elucidate the path from “molecule to solid” by quantifying the structural and energetic changes associated with the incorporation of the “III-V-IV₃” cores into the solid.

Most of the experimental work leading to the formation of the $\text{Al}(\text{As}_{1-x}\text{N}_x)\text{Si}_3$ and $\text{Al}(\text{P}_{1-x}\text{N}_x)\text{Si}_3$ materials and associated measurements of their optical properties were performed collaboratively and are reported in detail in paper by Kouvetakis et al.³⁶ This chapter presents complementary quantum chemical calculations, which are used to study the reactivity of the silyl precursors on the basis of their electrostatic and electron density maps, as well as their energies. The molecular calculations are then combined with solid-state simulations to elucidate the path from “molecule to solid” by quantifying the structural and energetic changes associated with the incorporation of the “III-V-IV₃” cores into the solid.

Structural and bonding insights from first principles simulations

As described in Ref. 36, the synthesis of $\text{Al}(\text{As}_{1-x}\text{N}_x)\text{Si}_3$ and $\text{Al}(\text{P}_{1-x}\text{N}_x)\text{Si}_3$ materials is based on a strategy which exploits the decomposition of intermediate “ $\text{Al}:\text{M}(\text{SiH}_3)_3$ ”

complexes envisioned to be formed via reactions of Al atoms and the $M(\text{SiH}_3)_3$ ($M=\text{N,P,As}$) precursors. This interaction can be naturally interpreted in terms of acid-base type combinations between atomic Al species and the $M(\text{SiH}_3)_3$ co-reactants. To further explore this reaction behavior a series of first-principles quantum chemical calculations of the atomic and electronic structure were carried out, and reactivity trends of the individual $M(\text{SiH}_3)_3$ precursors as well as those of the corresponding intermediate $\text{Al}:M(\text{SiH}_3)_3$ complexes. For the sake of simplicity, and without compromising the interpretation of the results, the Al atoms in the latter are decorated with hydrogen atoms to form the hypothetical $\text{H}_3\text{Al}-M(\text{SiH}_3)_3$ adducts. These harbor the inherent building units of the target solids and therefore represent ideal model compounds for the theoretical simulations. The detailed structural information derived from these adducts can then be used to gain new insight into the structural changes associated with their incorporation as bonded “Al-M-Si₃” units within the target $\text{AlP}_{1-x}\text{N}_x\text{Si}_3$ and $\text{AlAs}_{1-x}\text{N}_x\text{Si}_3$ crystalline products. As shown below, the structural, electronic and thermodynamic properties of the solids can be readily obtained using a consistent computational procedure using density functional theory at the LDA level and a standard plane-wave pseudopotential basis description (details are provided in the following pages). For this reason the molecular calculations are carried out at the LDA level using the *Gaussian03* package, and a high quality basis sets (6-311G++(3pd,3df)).¹⁰⁴

The main results of the simulations are summarized in Figure 29, where the structural properties of the precursor molecules, and their corresponding AlH_3 adducts, are compared in the top and bottom panels. Shown in the top left is the $\text{N}(\text{SiH}_3)_3$ molecule, which adopts the expected and well-established planar structure about the central NSi_3 core with Si-N-Si bond angles of $\sim 120^\circ$. This geometry is typically explained in textbooks by the classic (p \rightarrow d) π bonding model in which the lone-pair electrons on

the N is delocalized onto the Si 3d orbitals, thereby making these electrons unavailable for bonding in donor-acceptor reactions of the type described in this study. Also shown are the predicted structures of the $\text{P}(\text{SiH}_3)_3$ and $\text{As}(\text{SiH}_3)_3$ molecules. These are found to exhibit very similar geometries containing symmetrically canted silyl groups in which the apical hydrogen atoms point downwards.

In all three cases the calculated bond lengths and angles (in parentheses) are in good agreement with the experimental values obtained by gas electron diffraction studies of these compounds.^{111,112,129} For completeness, these basic calculations were also repeated for the $\text{Sb}(\text{SiH}_3)_3$ where, however, the unavailability of a full standard basis set necessitated the use of an effective core potential (ECP) on the Sb atom. After verifying that the ECP treatment of the related $\text{As}(\text{SiH}_3)_3$ system reproduces the full basis set structure and thermochemistry to within a few fractions of a percent, LDA level Sb-Si bond lengths and Si-Sb-Si bond angles of 2.58 Å and $\sim 86^\circ$ were obtained, in good agreement with the corresponding experimental values of 2.557 Å and 88° .^{130,131} In view of the trend towards even smaller bond angles about the central atom in this heavier molecule, a concomitant increase in its reactivity relative to that of $\text{As}(\text{SiH}_3)_3$ molecule is expected.

Next the reactivity of the $\text{N}(\text{SiH}_3)_3$, $\text{P}(\text{SiH}_3)_3$ and $\text{As}(\text{SiH}_3)_3$ molecules involved in the growth experiments of the $\text{Al}(\text{As}_{1-x}\text{N}_x)\text{Si}_3$ and $\text{Al}(\text{P}_{1-x}\text{N}_x)_y\text{Si}_{5-2y}$ alloys was quantified by evaluating their propensity to donate bonding charge in the context of the Lewis acid-base reactions. This was elucidated by mapping the total molecular electrostatic potential onto appropriate charge density contours, as illustrated for all three molecules using the 0.0005 density isosurface in the second row of Figure 29. These maps clearly indicate the electron-rich and electron-poor sites associated with local nucleophilic and electrophilic character, respectively. Here it is noted that both the $\text{P}(\text{SiH}_3)_3$ and $\text{As}(\text{SiH}_3)_3$

compounds possess favorable binding sites (orange region) with respect to nucleophilic attack. The prominent features above the P and As atoms in these perfectly pyramidal

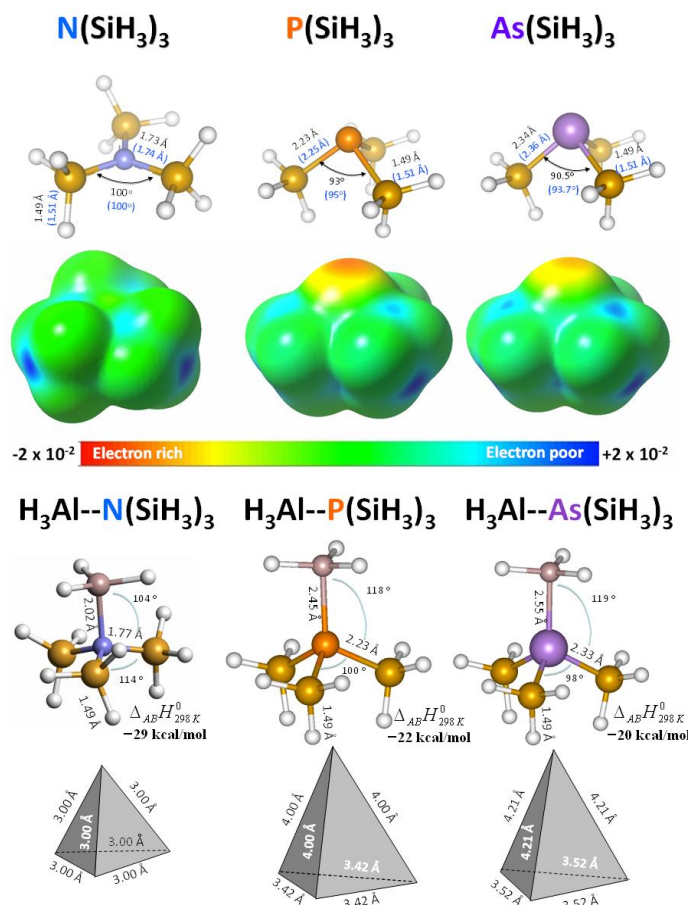


Figure 29: Equilibrium structures of the $M(\text{SiH}_3)_3$ precursor molecules (top), showing good agreement between calculated and experimental (in parentheses) bond lengths and angles. (middle) Molecular electrostatic potentials (ESP) of the $M(\text{SiH}_3)_3$ molecules mapped onto a common $\rho = 0.0005$ isodensity surface indicating distinct nucleophilic character above the central atom in both $\text{P}(\text{SiH}_3)_3$ and $\text{As}(\text{SiH}_3)_3$. The “neutral” ESP in $\text{N}(\text{SiH}_3)_3$ is consistent with the planar NSi_3 core and its associated weak basicity. (bottom) Adduct structures indicating that acid-base bonding minor changes in $\text{H}_3\text{Al}-\text{P}(\text{SiH}_3)_3$ and $\text{H}_3\text{Al}-\text{As}(\text{SiH}_3)_3$ units from their parent structures but a significant change in both the $\text{N}(\text{SiH}_3)_3$ and AlH_3 components upon bonding to form the $\text{H}_3\text{Al}-\text{N}(\text{SiH}_3)_3$ complex (see text). Bottom row shows the edge lengths of the tetrahedral structures subtended by the Al and Si atoms indicating the expected dilations along the M-Al bond direction.

structures correspond to lone-pairs enabling these molecules to readily participate in bonding with the electron-deficient Al atoms. This leads to the higher reactivity that

enables the target AlPSi_3 and AlAsSi_3 solids in perfectly single crystalline form at moderate temperatures (475-500 °C), as reported in prior work. In contrast to the ESP maps of $\text{P}(\text{SiH}_3)_3$ and $\text{As}(\text{SiH}_3)_3$, that of the $\text{N}(\text{SiH}_3)_3$ molecule (Figure 29) is virtually uniform in value, exhibiting no distinguishable features, which is consistent with the well-known poor reactivity of the latter compound. This distinct behavior is also manifestly evident in the experiments described above where the $\text{N}(\text{SiH}_3)_3$ precursor is only found to react with Al atoms at significantly higher temperatures ($\sim 550\text{-}600$ °C) suggesting the presence of a kinetic barrier. In this case the eventual reaction of $\text{N}(\text{SiH}_3)_3$ likely occurs via thermal activation of the out-of-plane “trampoline” mode in which the N-atom oscillates ($\sim 136\text{ cm}^{-1}$) with sufficient amplitude to create a dynamic nucleophilic site, thereby allowing bonding interaction with Al atoms. Nevertheless, under these conditions single phase crystalline films with the desired $\text{AlAs}_{1-x}\text{N}_x\text{Si}_3$ and $\text{AlP}_{1-x}\text{N}_x\text{Si}_3$ stoichiometries have been produced.

In the bottom portion of Figure 29 the predicted equilibrium structures are shown for the molecular AlH_3 adducts of the $\text{M}(\text{SiH}_3)_3$ compounds. To quantify the strength of these acid-base interactions in the context of “building blocks” their heat of reaction was computed by combining the enthalpy-corrected electronic energies (at 298K) for the AlH_3 and $\text{M}(\text{SiH}_3)_3$ units, and subtracting these from the corresponding values for the adducts, which yields -29, -22 and -20 kcal/mol for the N, P and As-based reactions, respectively. These values are very similar, and are in fact typical for analogous interactions involving Al and B alkyl compounds (methyl and ethyl) interacting with ammonia, where the corresponding interactions range from -20 to -35 kcal/mol. The calculated reaction energies are also consistent with the isosurface plots shown in Figure 29 which qualitatively display a very similar magnitude of nucleophilic character in the

case of the $\text{AlH}_3\text{-P}(\text{SiH}_3)_3$ and $\text{AlH}_3\text{-As}(\text{SiH}_3)_3$, but a distinctly larger value for $\text{AlH}_3\text{-N}(\text{SiH}_3)_3$.

Next the structures of $\text{AlH}_3\text{-P}(\text{SiH}_3)_3$ and $\text{AlH}_3\text{-As}(\text{SiH}_3)_3$ are compared with those of their parent molecules. Here it is found that the dative bonding induces typical changes of $\sim 0.01 \text{ \AA}$ in bond lengths and a systematic increase in the pyramidal angles by $\sim 7^\circ$. However, in the case of the $\text{AlH}_3\text{-N}(\text{SiH}_3)_3$ adduct the re-configuration upon bonding is more dramatic and involves both a significant dilation of the Si-N bond length (from 1.73 to 1.77 \AA), and concerted adjustment of all bond angles from planar towards a tetrahedral geometry. Furthermore, the strength of the Al-N bond is reflected by its compact length (2.02 \AA) in comparison to its somewhat weaker Al-P and Al-As counterparts (the latter (2.45-2.55 \AA)). From the point of view of internal angles (about the central atom) the average of the Al-M-Si and Si-M-Si angles is (perhaps coincidentally) $\sim 109^\circ$ in all three adducts, with the largest deviations of $\pm 10^\circ$ occurring in the P and As centered molecules, while a variation of only $\pm 5^\circ$ is found in the $\text{H}_3\text{Al-N}(\text{SiH}_3)_3$ case. These trends are also reflected in the tetrahedral edge lengths subtended by the outer adduct Al and Si constituents. In the case of the N compound all edges are virtually identical in length (3.00 \AA), while for the P and As compounds the basal edges are shorter (but identical) and the apical edges along the M-Al direction are dilated, thus giving rise to broader edge length distributions of $3.71 \pm 0.30 \text{ \AA}$ and $3.87 \pm 0.45 \text{ \AA}$, respectively.

The above findings at the molecular level suggest that the bond length and bond angle deviations in the tetrahedral III-V-IV₃ cores must be accommodated upon interlinking of these units to form a regular diamond-like framework. On the basis of this notion the ground state crystalline properties have been calculated, from which the equilibrium structures are obtained as a byproduct. The nature and degree of

“accommodation” required for the incorporation of the building blocks can then be inferred by comparing the tetrahedral cores of the “Al-M-Si₃” in the AlH₃-M(SiH₃)₃ molecules with their solid-state counterparts extracted from the equilibrium crystal structure. Here my prior work on AlPSi₃, AlAsSi₃ and their Al(As_xP_{1-x})Si₃ alloys is followed. The VASP code¹⁰⁸⁻¹¹⁰ is used, which employs ultra-soft pseudopotentials with an overall energy cutoff of 500 eV for all atomic species, including As, to carry out the electronic and crystal structure optimization calculations within the local density approximation (LDA) for exchange and correlation. The ground state crystal structure is described using a 20-atom cell with lattice parameters $\vec{a}_1 = a_0(\frac{3}{2}, -\frac{1}{2}, 0)$, $\vec{a}_2 = a_0(\frac{1}{2}, \frac{3}{2}, 0)$ and $\vec{a}_3 = a_0(0, 0, 1)$ where the Cartesian components are aligned with the conventional cubic (100), (010) and (001) directions in the parent diamond cubic structure with lattice parameter a_0 . A detailed description of the atomic positions of the III, IV and IV atoms is provided in prior publications.³³⁻³⁵

Briefly, the prototype ground state structure consists of III-V pairs—completely isolated from one another—in which the V atoms constitute a 3rd nearest neighbor sublattice in a manner that precludes the formation of energetically unfavorable Al-Al bonds. All crystal structures were optimized using the local density approximation and approximately 40 irreducible k -points for reciprocal space integration. With these settings highly converged structures with residual forces of < 0.01 eV/Å and stresses < 0.01 kbar were obtained. The same computational settings are employed in calculating the equilibrium properties of the constituent binary III-V alloys AlN, AlP and AlAs, and all relevant elemental reference states including Si, Al, P, As and N. The ground state forms of the latter are listed in the top portion of table 2, and indicate generally good agreement with respect to the experimental structures with a LDA underestimate of ~ - 0.8%. The main results for the ground state monoclinic structure of AlNSi₃, AlPSi₃ and

AlAsSi₃ (space group *C1c1*) (Ref.33) are summarized at the bottom of Table 2. Although the relative atomic positions are not explicitly listed here, it is found that they deviate only slightly from the ideal diamond-lattice values in AlAsSi₃ and AlPSi₃ (2-6%), while larger deviations (~9%) are predicted for the AlNSi₃ systems. The trends in deviation from ideal diamond structure are also manifested in the lattice parameters. As a point of reference, the 20-atom representation of the perfect ideal cubic lattice has unit cell

dimensions $\sqrt{\frac{5}{2}} a_0 \times \sqrt{\frac{5}{2}} a_0 \times a_0$. This can be viewed as a tetragonal cell with basal

dimension $a_T = \sqrt{\frac{5}{2}} a_0$, $c_T = a_0$ and c/a ratio of $\sqrt{\frac{2}{5}} = 0.63246$. As can be seen from the data in the table for the AlNSi₃ system, the basal dimensions a and b of the monoclinic cell deviate by as much as ~2% from their averaged value of $a_T = 7.796 \text{ \AA}$, while the c/a ratio exhibits a value 0.654, significantly different (~3-4%) from the ideal ratio for a cubic system.

Table 2: Summary of LDA equilibrium crystalline properties calculated for the (III-V)IV₃ alloys, and their constituent binary alloys and elemental reference states. The N₂ dimer was structurally optimized in a slightly asymmetrical supercell with fixed edge dimensions ~ 10 Å, yielding a bond length of 1.107 Å. For simplicity, the small PV correction ($\frac{1}{2}RT \sim 13 \text{ meV}$ at T= 298K) to the binding energies of compounds involving the N₂ reactant is not included. The $\langle a_0 \rangle$ lattice constants represent a equivalent cubic average obtained as $(8\Omega)^{1/3}$, where Ω is the atomic volume obtained by dividing the cell volumes by 20. Departures from ideality are described in the text.

	Z	a (Å)	b (Å)	c (Å)	α (°)	β (°)	γ (°)	$\langle a_0 \rangle$ (Å)	E ₀ (eV/atom)	ΔE_0 (eV)	ΔE_A (eV)
Elements											
Al (FCC)	4	3.974	3.974	3.974	90	90	90	3.974	-4.177		
Si (diamond)	8	5.386	5.386	5.386	90	90	90	5.386	-5.992		
P (monoclinic)	84	9.075	9.002	21.909	90	106.1	90		-6.028		
As (hexagonal)	3	3.761	3.761	10.076	90	90	120		-5.423		
N ₂ (gas)*	---	---	---	---	---	---	---		-8.655		
Binary Alloys											
AlN (wurtzite)	2	3.083	3.083	4.937	90	90	120		-8.2076	-3.583	
AlP (zincblende)	4	5.420	5.420	5.420	90	90	90	5.420	-5.7386	-1.273	
AlAs (zincblende)	4	5.623	5.623	5.623	90	90	90	5.623	-5.2878	-0.980	
(III-V)IV₃ Alloys											
AlNSi ₃	4	7.640	7.951	5.096	90	90	91.32	4.984	-6.4345	-1.365	+2.218
AlPSi ₃	4	8.525	8.555	5.448	90	90	90.33	(---) 5.460 (5.44)	-5.7032	-0.337	+0.936
AlAsSi ₃	4	8.709	8.690	5.537	90	90	90.24	5.558 (5.52)	-5.5149	-0.005	+0.975

By contrast the AlAsSi₃ system exhibits nearly equal basal dimensions differing by less than ~0.1% from the average value $a_T = 8.6995 \text{ \AA}$, with a corresponding c/a ratio of ~0.636, very close to the ideal $\sqrt{\frac{2}{3}}$ value. Accordingly, the AlAsSi₃ system is expected to be intrinsically very close to ideal cubic, while the AlNSi₃ shows very significant discrepancies from cubic symmetry. The origin of these non-idealities can be traced to the internal structure of the Al-M-Si₃ building blocks, extracted from the calculated ground state crystal structures, shown in Figure 29. In the case of AlNSi₃, the precursor H₃Al-N(SiH₃)₃ hydride contains Al-N and N-Si bonds with lengths of 2.02 Å and 1.77 Å, respectively, while the corresponding values in the solid are 1.96 Å and 1.84 Å, indicating the expected trend towards regularization. This is, however, accompanied by a significant broadening of the bond angle distribution from 104-114° in the molecule, to ~106-120° in the solid. The net result is a distortion of the tetrahedral units, as can be seen from the spread in edge lengths (2.95 Å-3.05 Å) (see bottom of Figure 30). In the case of AlPSi₃ and AlAsSi₃ systems the bond lengths exhibit a very similar regularization trend, but the bond angle distributions become significantly narrower and closer to the ideal tetrahedral value 109.4°. As a result, the incorporated tetrahedra in these systems adopt nearequalede lengths, imbuing the resulting crystal structure with a much more diamond-like topology. On the basis of the foregoing discussion the contrast in the deviations from perfect diamond symmetry can be most clearly seen by comparing the ground state structures of AlNSi₃ and AlAsSi₃ along a high-symmetry projection, such as (110) as shown in Figure 30.

In this structure's diagram it was chosen to show the most stable configurational motif comprised of AlNSi₃ and AlAsSi₃ building units ordered in a manner which avoids any Al-Al bonding. The figure clearly shows that the atomic positions in the AlNSi₃

appear “randomized” even though its crystal structure is in fact perfectly ordered and uniquely described by a relatively small unit cell.³⁵ This observation indicates that the small deviations from tetrahedral symmetry in the Al-N-Si₃ building blocks lead to an irregular assembly of a tetrahedral network, while the virtually ideal Al-As-Si₃ units produce the expect “diamond-like” projection, as shown in the right panel of Figure 31.

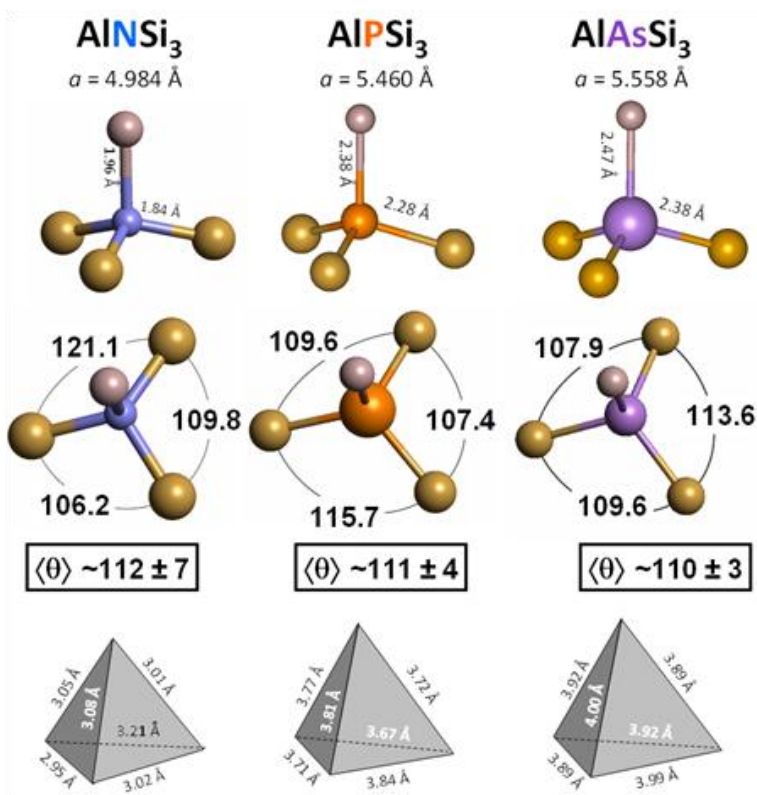


Figure 30: Structures of the molecular cores extracted from the equilibrium crystal structures (with lattice constants a) of AlNSi₃, AlPSi₃ and AlAsSi₃ indicating a systematic regularization of the tetrahedral units in the sequence N, P and As. First row indicates that the apical (M-Al) and basal M-Si bonds lengths differ by no more than 0.1 Å in any system. The irregularities in the crystalline structures are dictated by the deviations from regular tetrahedral values of the average bond angles and their spread. The largest departures are found in AlNSi₃, while the smallest occur in AlAsSi₃. This is manifested in the variation of edge lengths of the corresponding tetrahedral units (bottom row) which also decrease from AlNSi₃ to AlAsSi₃. Legend Si, N, P, As and Al are represented by gold, orange, purple and pink spheres, respectively.

Finally, the energy-structure-composition relationship in the AlMSi₃ (M=N,P,As) compounds is examined. One thermodynamic figure of merit is the heat of formation

(enthalpy), $\Delta_f H$, which is approximated here using static-lattice ground state energy (E_0) differences: $\Delta_f H \approx \Delta E_0[\text{AlMSi}_3] = E_0[\text{AlMSi}_3] - E_0[\text{Al}] - E_0[\text{M}] - 3 E_0[\text{Si}]$, where thermal corrections are not included. From the point of view of classic alloy theory $\Delta_f H$ is usually defined with respect standard elemental states of the constituents, which are themselves assumed to be randomly distributed on a lattice. In the AlMSi_3 alloys described in my work the incorporation of integral Al-M-Si₃ units confers a remarkable stability to the solids formed with this unusual stoichiometry.

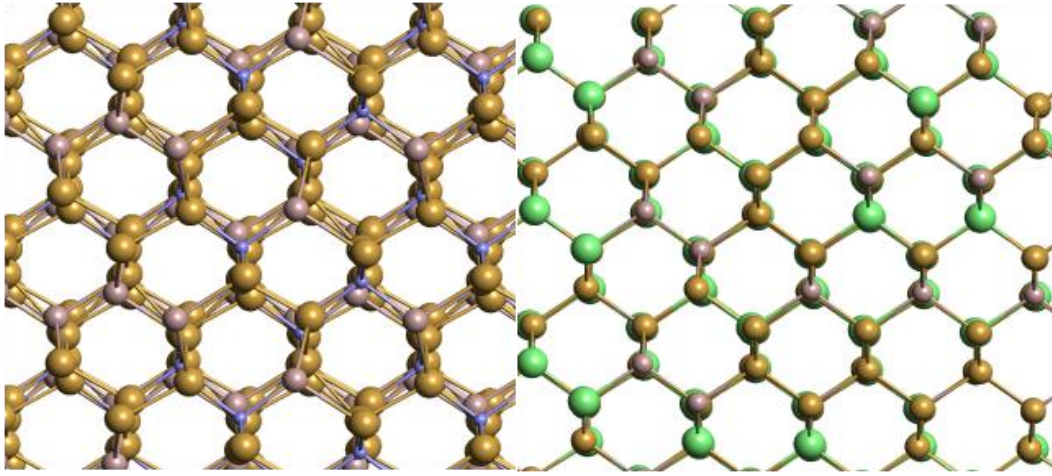


Figure 31: Structural models of AlNSi_3 (left) and AlAsSi_3 (right) in the (110) projection illustrating that for the nitride the tetrahedral atomic positions deviate significantly from those expected in a perfect diamond lattice. Legend :green blue violet and gold spheres represent As, N,Al, and Si, respectively

Accordingly, here the formation energies, ΔE_A , with respect to elemental Si and the stable binary alloys AlN, AlP and AlAs in their appropriate reference ground state structures are computed (see Table 2). These two measures of stability, ΔE_0 and ΔE_A , are simply related by the formula $\Delta E_0 = \Delta E_A + \Delta E_{\text{AIM}}$ where ΔE_{AIM} is the proxy for the formation enthalpy for the binary AlN, AlP and AlAs alloys from elements, listed as ΔE_0 in Table 2, e.g., $\Delta_f H_{\text{AIM}} \approx \Delta E_{\text{AIM}} = E_0[\text{AlM}] - E_0[\text{Al}] - E_0[\text{M}]$ where (M=N,P,As). The main results are contained in the last two columns of Table 2, which list ΔE_0 for both the AlMSi_3 and AlM alloys, as well as ΔE_A for the formation of AlMSi_3 from the AlM alloys

and silicon. The internal consistency of the simulation procedures can be readily verified by adding the latter quantity (ΔE_A) to the binary alloy formation energy ΔE_{AIM} to obtain the formation energy of $AlMSi_3$ from elements. For example, in the case of $AlPSi_3$, $\Delta E_o[AlPSi_3] = -0.337$ eV, $\Delta E_{AIM}[AlN] = -1.273$ eV and $\Delta E_A = +0.936$ eV. The principal conclusion from the calculations is that all of the $AlMSi_3$, and perhaps in general all (III-V)IV₃ compounds, are expected to be stable with respect to formation from their elements.

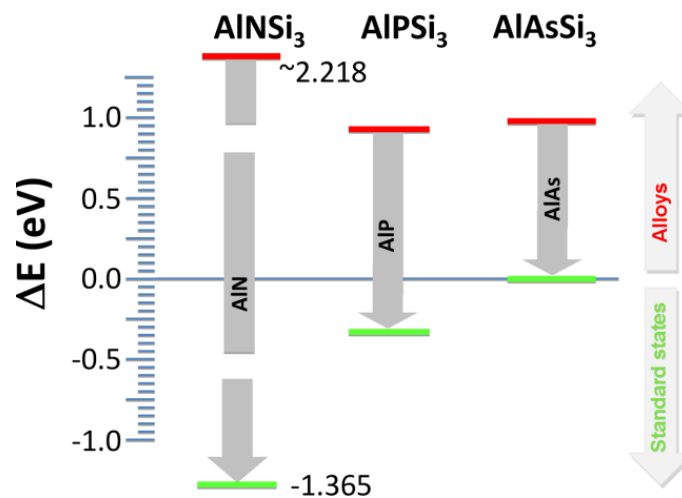


Figure 32: Formation energies of $AlPSi_3$, $AlPSi_3$, $AlAsSi_3$ compounds relative to the elements (green lines), binary AlN , AlP and $AlAs$ alloys, and Si (red lines).

In particular, the data suggests that $\Delta E_o(\text{nitrides}) < \Delta E_o(\text{phosphides}) < \Delta E_o(\text{arsenides})$ as shown in Figure 32, which summarizes the main results from Table 2 graphically. It is noted, however, as described above, that the nitrides exhibit significant deviations from cubic /tetrahedral symmetry making epitaxy-driven crystal assembly difficult.

Summary

It has been demonstrated that the addition of $N(SiH_3)_3$ into the reaction mixtures of $M(SiH_3)$ ($M = P, As$) with Al atoms under appropriate conditions, readily yields novel

$\text{Al}(\text{As}_{1-x}\text{N}_x)\text{Si}_3$ and $\text{Al}(\text{P}_{1-x}\text{N}_x)_y\text{Si}_{5-2y}$ alloys which exhibit enhanced optical absorption with respect to silicon as evidenced by spectroscopic measurements indicating potential applications in Si-based photovoltaics.³⁶ These materials can be grown as mono-crystalline layers completely lattice matched on Si via substitution of As and P by the markedly smaller N atoms.

REFERENCES

- 1 R. A. Soref and L. Friedman, *Superlattices and Microstructures* 14, 189 (1993).
- 2 V. R. D'Costa, C. S. Cook, A. G. Birdwell, C. L. Littler, M. Canonico, S. Zollner, J. Kouvetakis, and J. Menendez, *Phys. Rev. B* 73 (12), 125207 (2006).
- 3 C. H. L. Goodman, *Solid State and Electronic Devices*, IEEE Proceedings I 129 (5), 189 (1982).
- 4 O. Gurdal, R. Desjardins, J. R. A. Carlsson, N. Taylor, H. H. Radamson, J.-E. Sundgren, and J. E. Greene, *J. Appl. Phys.* 83, 162 (1998)
- 5 D. W. Jenkins and J. D. Dow, *Phys. Rev. B* 36, 7994 (1987).
- 6 J. Mathews, R. T. Beeler, J. Tolle, C. Xu, R. Roucka, J. Kouvetakis, and J. Menéndez, *Appl. Phys. Lett.* 97, 221912 (2010).
- 7 S.-L. Cheng, J. Lu, G. Shambat, H.-Y. Yu, K. Saraswat, J. Vuckovic, and Y. Nishi, *Opt. Express* 17, 10019 (2009).
- 8 H. S. Lan, S. T. Chan, T. H. Cheng, C. Y. Chen, S. R. Jan, and C. W. Liu, *Appl. Phys. Lett.* 98 (10), 101106 (2011).
- 9 M. Bauer, J. Taraci, J. Tolle, A. V. G. Chizmeshya, S. Zollner, D. J. Smith, J. Menendez, C. Hu, and J. Kouvetakis, *Appl. Phys. Lett.* 81, 2992 (2002).
- 10 G. Grzybowski, R. Roucka, J. Mathews, L. Jiang, R. Beeler, J. Kouvetakis, and J. Menéndez, *Phys. Rev. B* 84 (20), 205307 (2011).
- 11 F. A. Trumbore, *J. Electrochem. Soc.* 103 (11), 597 (1956).
- 12 R. F. C. Farrow, D. S. Robertson, G. M. Williams, A. G. Cullis, G. R. Jones, I. M. Young, and M. J. Dennis, *J. Cryst. Growth* 54, 507 (1981).
- 13 J. P. Leonard, B. Shin, J. W. McCamy, and M. J. Aziz, *Mat. Res. Soc. Symp. Proc.* 749, W16.11 (2002).
- 14 R. Loo, G. Wang, L. Souriau, J. C. Lin, S. Takeuchi, G. Brammertz, and M. Caymax, *J. Electrochem. Soc.* 157 (1), H13 (2010).
- 15 J. Taraci, J. Tolle, M. R. M. Cartney, J. Menendez, M. A. Santana, D. J. Smith, and J. Kouvetakis, *Appl. Phys. Lett.* 78, 3607 (2001).

- 16 R. Roucka, R. Beeler, J. Mathews, M.-Y. Ryu, Y. Kee Yeo, J. Menéndez, and J. Kouvetakis, *J. Appl. Phys.* 109, 103115 (2011).
- 17 J. Mathews, R. Roucka, J. Q. Xie, S. Q. Yu, J. Menendez, and J. Kouvetakis, *Appl. Phys. Lett.* 95 (13), 133506 (2009).
- 18 R. Roucka, J. Mathews, C. Weng, R. Beeler, J. Tolle, J. Menendez, and J. Kouvetakis, *IEEE J. Quant. Electron.* 47 (2), 213 (2011).
- 19 R. Roucka, J. Mathews, R. T. Beeler, J. Tolle, J. Kouvetakis, and J. Menéndez, *Appl. Phys. Lett.* 98, 061109 (2011).
- 20 J. Q. Xie, J. Tolle, V. R. D'Costa, C. Weng, A. V. G. Chizmeshya, J. Menendez, and J. Kouvetakis, *Solid-State Electronics* 53 (8), 816 (2009).
- 21 A. J. Noreika and M. H. Francombe, *J. Appl. Phys.* 45 (8), 3690 (1974).
- 22 K. C. Cadien, A. H. Eltoukhy, and J. E. Greene, *Appl. Phys. Lett.* 38 (10), 773 (1981).
- 23 I. Banerjee, D. W. Chung, and H. Kroemer, *Appl. Phys. Lett.* 46 (5), 494 (1985).
- 24 A. G. Norman, J. M. Olson, J. F. Geisz, H. R. Moutinho, A. Mason, M. M. Al-Jassim, and S. M. Vernon, *Appl. Phys. Lett.* 74 (10), 1382 (1999).
- 25 K. Newman and J. Dow, *Phys. Rev. B* 27 (12), 7495 (1983).
- 26 J. Greene, *J. Vac. Sci. Technol. B* 1 (2), 229 (1983).
- 27 K. Newman, A. Lastras-Martinez, B. Kramer, S. Barnett, M. Ray, J. Dow, J. Greene, and P. Raccah, *Phys. Rev. Lett.* 50, 1466 (1983)
- 28 H. Holloway and L. Davis, *Phys. Rev. Lett.* 53, 1510 (1984).
- 29 R. Osório, S. Froyen, and A. Zunger, *Phys. Rev. B* 43, 14055 (1991)
- 30 G. Giorgi, M. Schilfgaarde, A. Korkin, and K. Yamashita, *Nanoscale Research Letters* 5, 469 (2010).
- 31 V. L. Solozhenko, D. Andrault, G. Fiquet, M. Mezouar, and D. C. Rubie, *Appl. Phys. Lett.* 78 (10), 1385 (2001).
- 32 T. C. McGlinn, M. V. Klein, L. T. Romano, and J. E. Greene, *Phys. Rev. B* 38 (5), 3362 (1988).

- 33 Watkins, T.; Chizmeshya, A. V.; Jiang, L.; Smith, D. J.; Beeler, R. T.; Grzybowski, G.; Poweleit, C. D.; Menendez, J.; Kouvetakis, J. J. *Am. Chem. Soc.* 2011, 133, 16212.
- 34 Watkins, T.; Jiang, L.; Xu, C.; Chizmeshya, A. V. G.; Smith, D. J.; Menéndez, J.; Kouvetakis, J. *Appl. Phys. Lett.* 2012, 100, 022101.
- 35 G. Grzybowski, T. Watkins, R. T. Beeler, L. Jiang, D. J. Smith, A. V. G. Chizmeshya, J. Kouvetakis, and J. Menendez, *Chemistry of Materials* 24, 2347-2355 (2012).
- 36 J. Kouvetakis, A. V. G. Chizmeshya, L. Jiang, T. Watkins, G. Grzybowski, R. T. Beeler, C. Poweleit, and J. Menéndez, *Chemistry of Materials* 24, 3219 (2012).
- 37 M. J. Adams and P. T. Landsberg, in 9th International Conference on the Physics of Semiconductors (Akademiya Nauk, Moscow, 1968), p. 619.
- 38 J. Liu, X. Sun, R. Camacho-Aguilera, L. C. Kimerling, and J. Michel, *Opt. Lett.* 35, 679 (2010).
- 39 X. Sun, J. Liu, L. C. Kimerling, and J. Michel, *Appl. Phys. Lett.* 95, 011911 (2009).
- 40 X. Sun, J. Liu, L. C. Kimerling, and J. Michel, *Opt. Lett.* 34, 1198 (2009).
- 41 S.-L. Cheng, G. Shambat, J. Lu, H.-Y. Yu, K. Saraswat, T. I. Kamins, J. Vuckovic, and Y. Nishi, *Appl. Phys. Lett.* 98, 211101 (2011).
- 42 S. R. Jan, C. Y. Chen, C. H. Lee, S. T. Chan, K. L. Peng, C. W. Liu, Y. Yamamoto, and B. Tillack, *Appl. Phys. Lett.* 98, 141105 (2011).
- 43 M. Kittler, T. Arguirov, M. Oehme, Y. Yamamoto, B. Tillack, and N. V. Abrosimov, *phys. stat. sol. (a)* 208, 754 (2011).
- 44 T. H. Cheng, C. Y. Ko, C. Y. Chen, K. L. Peng, G. L. Luo, C. W. Liu, and H. H. Tseng, *Appl. Phys. Lett.* 96, 091105 (2010).
- 45 Beeler, R. T.; Grzybowski, G. J.; Roucka, R.; Jiang, L.; Mathews, J.; Smith, D. J.; Menéndez, J.; Chizmeshya, A.V.G.; Kouvetakis, J. *Chem. Mater.* 2011, 23, 4480
- 46 M. A. Wistey, Y. Y. Fang, J. Tolle, A. V. G. Chizmeshya, and J. Kouvetakis, *Appl. Phys. Lett.* 90, 082108 (2007).
- 47 A. L. Smirl, S. C. Moss, and J. R. Lindle, *Phys. Rev. B* 25, 2645 (1982).
- 48 E. Gaubas and J. Vanhellefont, *Appl. Phys. Lett.* 89, 142106 (2006).

- 49 J. R. Haynes, Phys. Rev. 98, 1866 (1955).
- 50 S. L. Chuang, Physics of Optoelectronic Devices (Wiley, New York, 1995).
- 51 O. Madelung ed., Semiconductors: Intrinsic Properties of Group IV Elements and III-V, II-VI, and I-VII compounds (Springer-Verlag, Berlin, 1985).
- 52 V. Sorianello, A. Perna, L. Colace, G. Assanto, H. C. Luan, and L. C. Kimerling, Appl. Phys. Lett. 93, 111115 (2008).
- 53 W. Klingenstein and H. Schweizer, Solid-State Electronics 21, 1371.
- 54 E. Grushka, Anal. Chem. 44, 1733 (1972).
- 55 C. Haas, Phys. Rev. 125, 1965 (1962).
- 56 C. J. Stanton and D. W. Bailey, Phys. Rev. B 45, 8369 (1992).
- 57 K. Tanaka, H. Ohtake, and T. Suemoto, Phys. Rev. Lett. 71, 1935 (1993).
- 58 B. P. Swain, H. Takato, Z. Liu, and I. Sakata, Solar Energy Materials and Solar Cells 95, 84 (2011).
- 59 A. Trita, I. Cristiani, V. Degiorgio, D. Chrastina, and H. von Känel, Appl. Phys. Lett. 91, 041112 (2007).
- 60 J. Mathews, Investigation of light absorption and emission in germanium and germanium-tin films grown on silicon substrates, PhD thesis, Arizona State University, 2011.
- 61 J. Wagner and L. Viña, Phys. Rev. B 30, 7030 (1984).
- 62 M. El Kurdi, T. Kociniewski, T. P. Ngo, J. Boulmer, D. Débarre, P. Boucaud, J. F. Damlencourt, O. Kermarrec, and D. Bensahel, Appl. Phys. Lett. 94, 191107 (2009).
- 63 P. Allen, Phys. Rev. B 18, 5217 (1978).
- 64 J. Michel, J. Liu, and L. C. Kimerling, Nat Photon 4 (8), 527 (2010).
- 65 Y. Bai, K. E. Lee, C. Cheng, M. L. Lee, and E. A. Fitzgerald, J. Appl. Phys. 104 (8), 084518 (2008).

- 66 Y. Huo, H. Lin, R. Chen, M. Makarova, Y. Rong, M. Li, T. I. Kamins, J. Vuckovic, and J. S. Harris, *Appl. Phys. Lett.* 98 (1), 011111 (2011).
- 67 R. Jakomin, M. de Kersauson, M. El Kurdi, L. Largeau, O. Mauguin, G. Beaudoin, S. Sauvage, R. Ossikovski, G. Ndong, M. Chaigneau, I. Sagnes, and P. Boucaud, *Appl. Phys. Lett.* 98 (9), 091901 (2011).
- 68 J. Kouvetakis, J. Menendez, and A. V. G. Chizmeshya, *Annual Review of Materials Research* 36, 497 (2006).
- 69 R. Beeler, R. Roucka, A. Chizmeshya, J. Kouvetakis, and J. Menéndez, *Phys. Rev. B* 84 (3) (2011).
- 70 S. Groves and W. Paul, *Phys. Rev. Lett.* 11, 194 (1963).
- 71 R. J. Temkin, G. A. N. Connell, and W. Paul, *Solid State Commun.* 11 (11), 1591 (1972).
- 72 D. J. Paul, *Semicond. Sci. Technol.* 19 (10), R75 (2004).
- 73 C. H. L. Goodman, *Jap. J. of Appl. Phys. Supplement 22-1* 22 (Supplement 22-1), 583 (1982).
- 74 S. I. Shah, J. E. Greene, L. L. Abels, Q. Yao, and P. M. Raccah, *J. Cryst. Growth* 83, 3 (1987).
- 75 P. R. Pukite, A. Harwit, and S. S. Iyer, *Appl. Phys. Lett.* 54 (21), 2142 (1989).
- 76 G. He and H. A. Atwater, *Appl. Phys. Lett.* 68 (5), 664 (1996).
- 77 B. Vincent, F. Gencarelli, H. Bender, C. Merckling, B. Douhard, D. H. Petersen, O. Hansen, H. H. Henrichsen, J. Meersschaut, W. Vandervorst, M. Heyns, R. Loo, and M. Caymax, *Appl. Phys. Lett.* 99 (15), 152103 (2011).
- 78 F. Gencarelli, B. Vincent, L. Souriau, O. Richard, W. Vandervorst, R. Loo, M. Caymax, and M. Heyns, *Thin Solid Films* 520 (8), 3211 (2012).
- 79 V. R. D'Costa, Y. Fang, J. Mathews, R. Roucka, J. Tolle, J. Menendez, and J. Kouvetakis, *Semicond. Sci. Technol.* 24 (11), 115006 (2009).
- 80 G. Grzybowski, L. Jiang, R. T. Beeler, T. Watkins, A. V. G. Chizmeshya, C. Xu, J. Menéndez, and J. Kouvetakis, *Chemistry of Materials* 24 (9), 1619 (2012).

- 81 H. Kim, N. Taylor, T. R. Bramblett, and J. E. Greene, *J. Appl. Phys.* 84 (11), 6372 (1998).
- 82 W.-J. Yin, X.-G. Gong, and S.-H. Wei, *Phys. Rev. B* 78 (16), 161203 (2008).
- 83 Thomas, S. G.; Bauer, M.; Stephens, M.; Kouvetakis, J. *Solid State Technology* 2009, 52, 12.
84. Green, M. A. *Prog. Photovoltaics* 2001, 9, 123.
85. Xie, J.; Chizmeshya, A.V.G.; Tolle, J.; D'Costa, V.R.; Menéndez, J.; Kouvetakis, J.; *Chem. Mater.* 2010, 22, 3779.
86. Kouvetakis, J.; Mathews, J.; Roucka, R.; Chizmeshya, A.V.G.; Tolle, J.; Menéndez, J. *IEEE Photonics Journal* 2010, 2, 924.
87. Fang, Y-Y; Tolle, J.; D'Costa, V.R.; Menendez, J.; Chizmeshya, A.V.G.; Kouvetakis, J. *Chem. Mater.* 2007, 19, 5910.
88. Luan, H.-C.; Lim, D.R.; Lee, K.K.; Chen, K. M.; Sandland, J.G.; Wada, K.; Kimerling, L.C. *Appl. Phys. Lett.* 1999, 75, 2909.
89. Shang, H.; Frank, M.M.; Gusev, E.P.; Chu, J.O.; Bedell, S.W.; Guarini, K.W.; Jeong, M. *IBM J. Res. Dev.* 2006, 50/4-5, 377.
90. Liu, J.F.; Michel, J.; Giziewicz, W.; Pan, D.; Wada, K.; Cannon, D. D.; Jongthammanurak, S.; Danielson, D. T.; Kimerling, L.C.; Chen, J.; Ilday, F. O.; Kartner, F.X.; Yasaitis, J. *Appl. Phys. Lett.* 2005, 87, 103501.
91. Kuo, Y. H.; Lee, Y.K.; Ge, Y.S.; Ren, S.; Roth, J.E.; Kamins, T.I.; Miller, D.A.B.; Harris, J.S. *Nature* 2005, 437, 1334.
92. Chung, K. H.; Yao, N.; Benziger, J.; Sturm, J.C.; Singh, K. K.; Carlson, D.; Kuppurao, S. *Appl. Phys. Lett.* 2008, 92, 113506.
93. Fitzgerald, E. A.; Samavedam, S. B. *Thin Solid Films* 1997, 294, 3.
94. Fischer, P.R.; Aerde, S.V.; Oosterlaken, E.; Bozon, B.; Zagwijn, P.M.; Bauer, M.; Yan, M.; Verweij W. *ECS Transact.* 2006, 3/2, 203.
95. Fang, Y.-Y.; D'Costa, V.R.; Tolle, J.; Poweleit, C.D.; Kouvetakis J.; Menéndez, J. *Thin Solid Films* 2008, 516, 8327.
96. Drake J.E.; Jolly W.L. *Inorg. Synth.* 1963, 7, 34.

97. Drake, J.E.; Jolly, W.L. *J. Chem Soc.* 1962, 2807
98. Mackay, K.M; Sutton, K. J. *J. Chem. Soc.*1968, 2312.
99. Mackay, K.M.; Robinson, P. J. *Chem. Soc.* 1965, 5121.
100. Estacio, P.; Sefcik, M. D.; Chan, E.K.; Ring M. A. *Inorg. Chem.* 1970, 9,1068.
101. Boourasseau C. Patent Application US 2008/0175784 A1; Pub. Date Jul. 24, 2008.
102. Ritter, C. J.; Hu, C.-W.; Chizmeshya, A.V.G.; Tolle, J.; Klewer, D.; Tsong, I.S.T.; Kouvetakis, J. *J. Am. Chem. Soc.* 2005, 127, 9855.
103. Ritter, C.J.; Hu, C-W.; Chizmeshya, A.V.G.; Tolle, J.; Nieman, R.; Tsong, I.S.T.; Kouvetakis, J. *J. Am. Chem. Soc.* 2006, 128, 6919.
104. Gaussian 03, Revision C.02, M. J. Frisch, G. W. Trucks, H. B. Schlegel, G. E. Scuseria, M. A. Robb, J. R. Cheeseman, J. A. Montgomery, Jr., T. Vreven, K. N. Kudin, J. C. Burant, J. M. Millam, S. S. Iyengar, J. Tomasi, V. Barone, B. Mennucci, M. Cossi, G. Scalmani, N. Rega, G. A. Petersson, H. Nakatsuji, M. Hada, M. Ehara, K. Toyota, R. Fukuda, J. Hasegawa, M. Ishida, T. Nakajima, Y. Honda, O. Kitao, H. Nakai, M. Klene, X. Li, J. E. Knox, H. P. Hratchian, J. B. Cross, V. Bakken, C. Adamo, J. Jaramillo, R. Gomperts, R. E. Stratmann, O. Yazyev, A. J. Austin, R. Cammi, C. Pomelli, J. W. Ochterski, P. Y. Ayala, K. Morokuma, G. A. Voth, P. Salvador, J. J. Dannenberg, V. G. Zakrzewski, S. Dapprich, A. D. Daniels, M. C. Strain, O. Farkas, D. K. Malick, A. D. Rabuck, K. Raghavachari, J. B. Foresman, J. V. Ortiz, Q. Cui, A. G. Baboul, S. Clifford, J. Cioslowski, B. B. Stefanov, G. Liu, A. Liashenko, P. Piskorz, I. Komaromi, R. L. Martin, D. J. Fox, T. Keith, M. A. Al-Laham, C. Y. Peng, A. Nanayakkara, M. Challacombe, P. M. W. Gill, B. Johnson, W. Chen, M. W. Wong, C. Gonzalez, and J. A. Pople, Gaussian, Inc., Wallingford CT, 2004.
105. Weng, C.; Kouvetakis, J.; Chizmeshya, A. V. G. *J. Comput. Chem.* 2011, 32 (5), 835.
106. Chen, S.S.; Wilhoit, R.C.; Zolinski, B.J. *J. Phys. Chem. Ref. Data.* 1975, 4 (4).
107. Vegard, L. *Zeitschrift für Physik* 1921, 5, 17.
108. Kresse, G.; Hafner, J. *Phys. Rev. B* 1993, 47, 558.
109. Kresse, G.; Furthmüller, J. *Computational Materials Science* 1996, 6, 15.

110. Kresse, G.; Furthmüller, J. *Phys. Rev. B* 1996, 54, 11169.
111. Beagley, B.; Robiette, A. G.; Sheldrick, G. M. *Journal of the Chemical Society A: Inorganic, Physical, Theoretical* 1968.
112. Blake, A. J.; Ebsworth, E. A. V.; Henderson, S. G. D. *Acta Crystallographica* 1991, C47, 486.
113. Sharma, S.; Dewhurst, J.; Ambrosch-Draxl, C. *Phys. Rev. Lett.* 2005, 95, 136402.
114. Roucka, R.; Tolle, J.; Chizmeshya, A. V. G.; Crozier, P. A.; Poweleit, C. D.; Smith, D. J.; Tsong, I. S. T.; Kouvetakis, J. *Phys. Rev. Lett.* 2002, 88, 206102/1.
115. Davidson, G.; Woodward, L. A.; Ebsworth, E. A. V.; Sheldrick, G. M. *Spectrochimica Acta* 1967, 23A, 2609.
116. *Semiconductors: Physics of Group IV Elements and III-V compounds*; Madelung, O., Ed.; Springer-Verlag: Berlin, 1985; Vol. 17a.
117. Bean, J. C.; Feldman, L. C.; Fiory, A. T.; Nakahara, S.; Robinson, I. K. *J. Vac. Sci. Technol. A* 1984, 2, 436.
118. Menéndez, J. *J. Appl. Phys.* 2009, 105, 063519.
119. Aspnes, D. E.; Studna, A. A. *Phys. Rev. B* 1983, 27, 985.
120. Menéndez, J. In *Raman Scattering in Materials Science*; Weber, W. H., Merlin, R., Eds.; Springer: Berlin, 2000; Vol. 42, p 55.
121. Refson, K.; Clark, S. J.; Tulip, P. R. *Phys. Rev. B* 2006, 73, 155114.
122. Omote, K. *J. Phys: Condens. Matter* 2010, 22, 474004.
123. Go, S.; Bilz, H.; Cardona, M. *Phys. Rev. Lett.* 1975, 34, 580.
124. *Semiconductors: Intrinsic Properties of Group IV Elements and III-V, II-VI, and I-VII compounds*; Madelung, O., Ed.; Springer-Verlag: Berlin, 1985; Vol. 22a.
125. Shin, H. K.; Lockwood, D. J.; Baribeau, J.-M. *Solid State Commun.* 2000, 114, 505.
126. I. Vurgaftman, J. R. Meyer, and L. R. Ram-Mohan, *J. Appl. Phys.* 89 (11), 5815 (2001).

127. I. Vurgaftman and J. R. Meyer, *J. Appl. Phys.* 94 (6), 3675 (2003).
128. D. J. Friedman, S. R. Kurtz, and J. F. Geisz, presented at the Photovoltaic Specialists Conference, 2002. Conference Record of the Twenty-Ninth IEEE, 2002 (unpublished).
129. K. Hedberg, *J. Am. Chem. Soc.* 77 (24), 6491 (1955).
130. D. W. H. Rankin, A. G. Robiette, G. M. Sheldrick, B. Beagley, and T. G. Hewitt, *Journal of Inorganic and Nuclear Chemistry* 31 (8), 2351 (1969).
131. A. V. G. Chizmeshya, C. Ritter, J. Tolle, C. Cook, J. Menendez, and J. Kouvetakis, *Chem. Mater.* 18 (26), 6266 (2006).

APPENDIX A
SYNTHESIS OF COMMON REACTANTS

Experimental

The growth method used in this work to produce (III-V)IV alloys required the synthesis of pure $(IV_3)_3M$ hydrides. Accordingly, the following syntheses were used to produce $(SiH_3)_3M$ (P, As, Sb) and $(GeH_3)_3P$ hydrides. The $(SiH_3)_3M$ and $(GeH_3)_3P$ have been produced for future thin film development. I note a general warning on the use of silanes used in these chemistries. They are pyrophoric and potentially explosive and thus special care should be taken to prevent personal injury in these syntheses.

General considerations

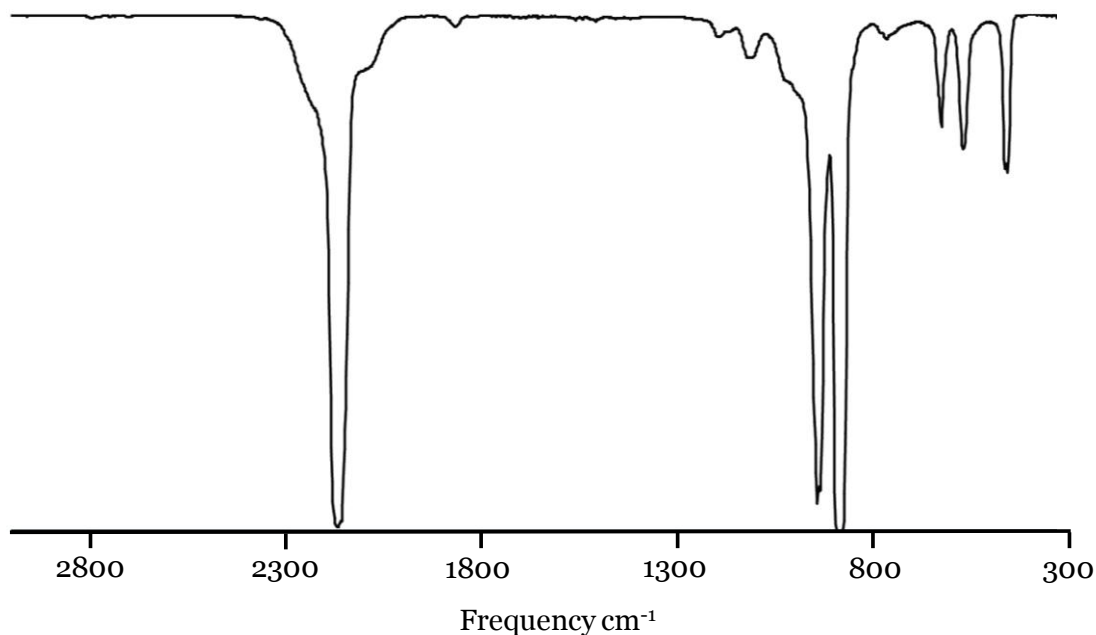
All manipulations were carried out under inert conditions using standard vacuum line and drybox techniques. All glass joints were lubricated using halogenated Krytox grease. Ethyl ether was distilled from sodium and benzophenone ketyl prior to use. NMR spectra were taken from a Bruker 400 MHz instrument. FTIR spectra were taken with a Nicolet-Magna IR 550 spectrometer using a 10 cm gas cell with KBr windows

Li_3X (X = P, As, Sb)

Lithium ribbon was loaded in to a 6 in. x 1/2 in. diameter stainless steel tube containing finely ground phosphorous (red, lump), arsenic, or antimony powder (>99% purity). The tube, containing a blanket of argon, was subsequently elevated to a temperature of 450°C for a period of 5 hours. At which time it was allowed to slowly come to room temperature and thoroughly blended using mortar and pestle. A thermal treatment for 9 h at 450°C was then applied to the compound. Upon completion it was reground and used with no further purification.

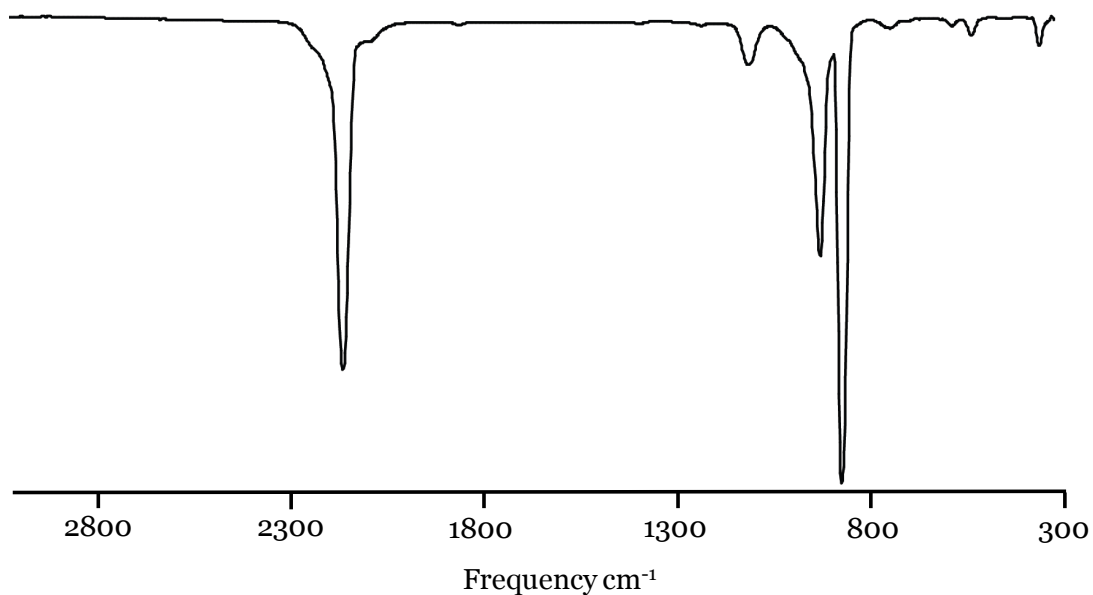
(SiH₃)₃P

SiH₃Br (5.9 g, 53mmol) was prepared using literature methods and was condensed into a 250ml flask containing Li₃P (0.7 g, 13.4mmol) and 30ml diethyl ether. The mixture was stirred at -78°C for 18 h. The volatiles were passed through U-traps at -60, -78, and -196. The latter retained the unreacted SiH₃Br and ether, while the -78°C trap contained the remaining ether. The -60°C trap was redistilled through -55°C and -196°C traps to obtain pure product (SiH₃)₃P (0.56 g, 4.5mmol, 33% yield). ¹H NMR : δ 3.820 (d, ¹J_{Si-H} = 212.16 Hz, ²J_{P-H} = 16.89 Hz, 9 H, SiH₃), IR (gas, cm⁻¹): 2166(vs), 2090(sh), 1194(w), 1113(w), 1023(sh), 942(s), 885(vs), 625(m), 570(m), 463(m), 455(m). The figure here shows the gas IR spectrum of the molecule.



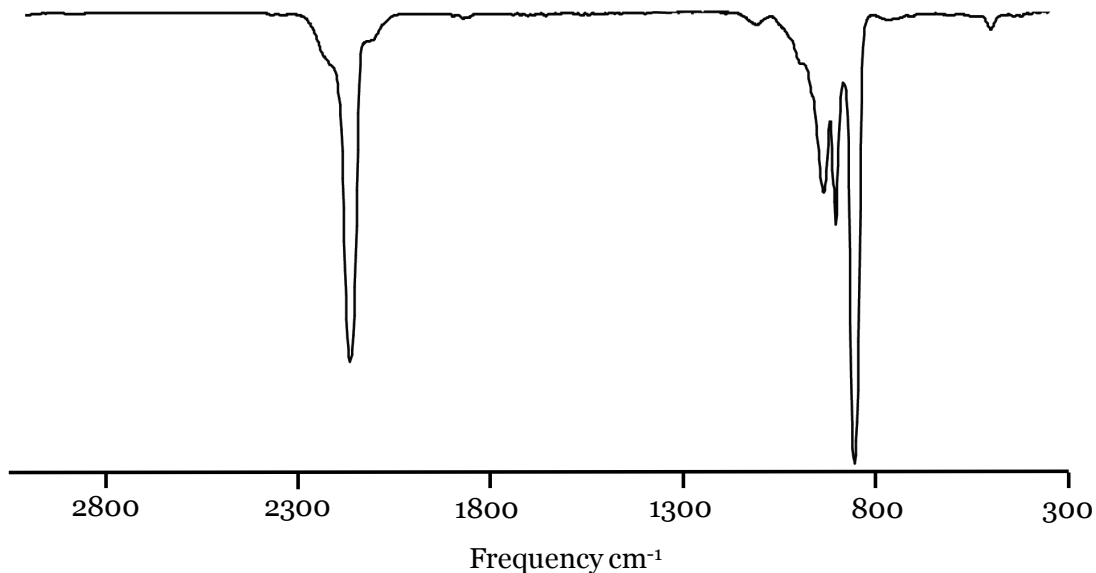
(SiH₃)₃As

SiH₃Br (6.6 g, 60 mmol) was condensed into a 250ml flask containing Li₃As (1.5 g, 20 mmol) and 30ml diethyl ether. The mixture was stirred at -78°C for 18 h. The volatiles were passed through U-traps at -60, -78, and -196. The latter retained the unreacted SiH₃Br and ether, while the -78°C trap contained the remaining ether. The -60°C trap was redistilled through -40°C and -196°C traps to obtain pure product (SiH₃)₃As (1.4 g, 10 mmol, 50% yield). ¹H NMR : δ 3.68 (s, ¹J_{Si-H} = 211.99 Hz, 9 H, SiH₃), IR (gas, cm⁻¹) 2163(vs), 2096(sh), 1115(m), 930(s), 875(vs), 749(w), 590(w), 540(w), 365(w). The figure here shows the gas IR spectrum of the molecule.



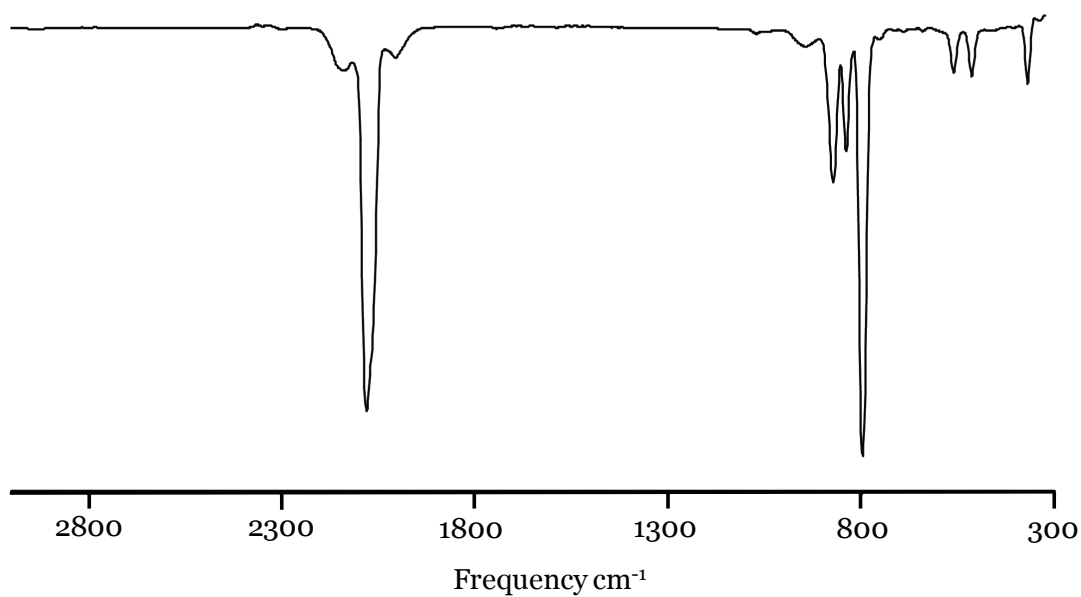
(SiH₃)₃Sb

SiH₃Br (6.2 g, 56 mmol) was condensed into a 250ml flask containing Li₃Sb (2.0 g, 14 mmol) and 30ml diethyl ether. The mixture was stirred at -78°C for 18 h. The volatiles were passed through U-traps at -60, -78, and -196. The latter retained the unreacted SiH₃Br and ether, while the -78°C trap contained the remaining ether. The -60°C trap was redistilled through -20°C and -196°C traps to obtain pure product (SiH₃)₃Sb (2.1 g, 10 mmol, 70% yield). ¹H NMR : δ 3.502 (s, ¹J_{Si-H} = 208.92 Hz, 9 H, SiH₃), IR (gas, cm⁻¹) 2206(sh), 2159(vs), 2104(sh), 932(s), 906(sh), 900(s), 851(vs), 498(w). The figure below shows the gas IR spectrum of the molecule.



(GeH₃)₃P

Freshly prepared GeH₃Cl (2.27 g, 21 mmol) was condensed into a 250ml flask containing Li₃P (0.315 g, 6.1 mmol) and 10 ml diethyl ether. The mixture was stirred at -78°C for 18 h, allowed to slowly warm to 20°C for 2 h, and subsequently purified. The volatiles were passed through U-traps at -40, -78, and -196 and analyzed by FTIR. The latter retained the unreacted GeH₃Cl and ether, while the -78°C trap contained the remaining ether. The -40°C trap was redistilled through -50°C and -196°C traps to obtain pure product (GeH₃)₃p (0.3 g, 10 mmol, 20% yield). ¹H NMR : δ 3.86 (d, ²J_{p-H} = 15.85 Hz, 9 H, GeH₃), IR (gas, cm⁻¹) 2137(sh), 2079(vs), 2066(sh), 944(w), 872(m), 839(m), 797(vs), 561(m), 514(m), 370(m). The figure here shows the gas IR spectrum of the molecule.



APPENDIX B

COPYRIGHT RELEASE FOR PUBLICATIONS

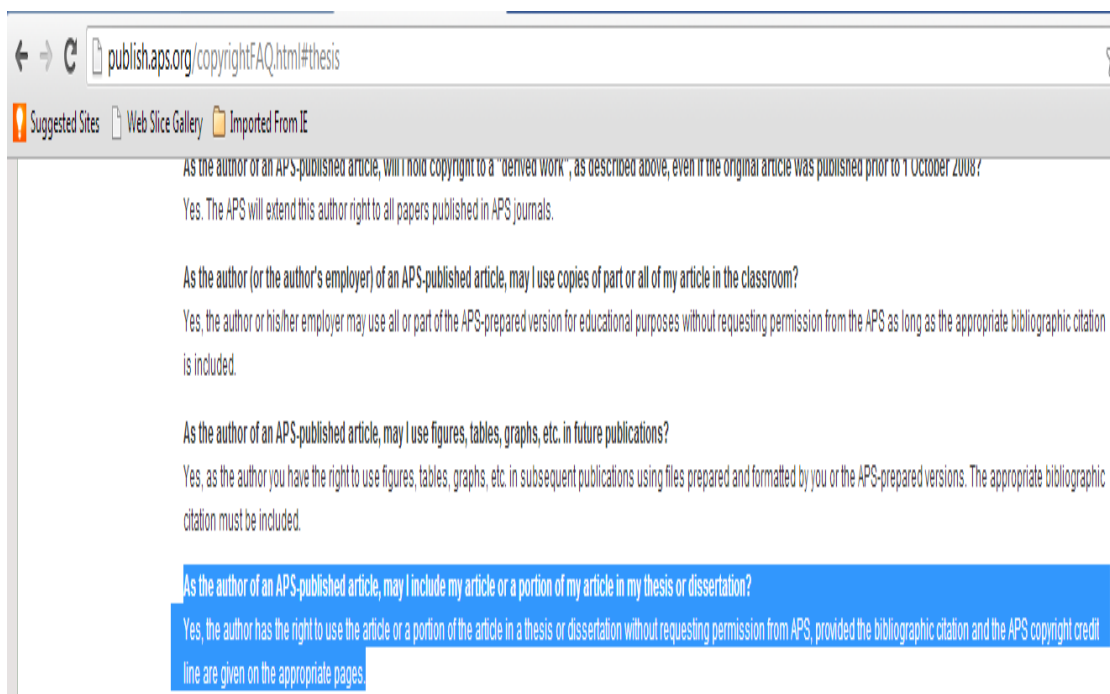
All co-authors on publications have granted permission to the publication of their respective manuscripts contained in this thesis. I have also received copyright release from the respective publishers as shown below in the following images.

American Physical Society

PHYSICAL REVIEW B 84, 205307 (2011)

Direct versus indirect optical recombination in Ge films grown on Si substrates

Author: G. Grzybowski, R. Roucka, J. Mathews, L. Jiang, R. T. Beeler, J. Kouvetakis, and J. Menendez



American Institute of Physics : Liscence number 3072600815528 for “Photoluminescence from heavily doped GeSn:P materials grown on Si(100)

**AMERICAN INSTITUTE OF PHYSICS LICENSE
TERMS AND CONDITIONS**

Jan 19, 2013

All payments must be made in full to CCC. For payment instructions, please see information listed at the bottom of this form.

License Number	3072600815528
Order Date	Jan 19, 2013
Publisher	American Institute of Physics
Publication	Applied Physics Letters
Article Title	Photoluminescence from heavily doped GeSn:P materials grown on Si(100)
Author	G. Grzybowski, L. Jiang, J. Mathews, R. Roucka, et al.
Online Publication Date	Oct 27, 2011
Volume number	99
Issue number	17
Type of Use	Thesis/Dissertation
Requestor type	Author (original article)
Format	Print and electronic
Portion	Excerpt (> 800 words)
Will you be translating?	No
Title of your thesis / dissertation	Epitaxy of Group IV and III-V-IV Optoelectronic Materials on Silicon by Purpose Driven Synthesis of Designer Molecules (tentative)
Expected completion date	Apr 2013
Estimated size (number of pages)	150

American Institute of Physics : Liscence number 3072600282315

Next Generation of Ge₁-YSn_Y (Y = 0.01-0.09) alloys grown on Si(100) via Ge₃H₈ and SnD₄: Reaction kinetics and tunable emission

**AMERICAN INSTITUTE OF PHYSICS LICENSE
TERMS AND CONDITIONS**

Jan 19, 2013

All payments must be made in full to CCC. For payment instructions, please see information listed at the bottom of this form.

License Number	3072600282315
Order Date	Jan 19, 2013
Publisher	American Institute of Physics
Publication	Applied Physics Letters
Article Title	Next generation of Ge ₁ -ySn _y (y = 0.01-0.09) alloys grown on Si(100) via Ge ₃ H ₈ and SnD ₄ : Reaction kinetics and tunable emission
Author	G. Grzybowski, R. T. Beeler, L. Jiang, D. J. Smith, et al.
Online Publication Date	Aug 16, 2012
Volume number	101
Issue number	7
Type of Use	Thesis/Dissertation
Requestor type	Author (original article)
Format	Print and electronic
Portion	Excerpt (> 800 words)
Will you be translating?	No
Title of your thesis / dissertation	Epitaxy of Group IV and III-V-IV Optoelectronic Materials on Silicon by Purpose Driven Synthesis of Designer Molecules (tentative)
Expected completion date	Apr 2013
Estimated size (number of pages)	150
Total	0.00 USD

Ultralow temperature epitaxy of Ge based semiconductors and optoelectronic structures on Si(100) :Introducing higher order germanes (Ge₃H₈ and Ge₄H₁₀)

Gordon Grzybowski, Liying Jiang, Richard T. Beeler, Tylan Watkins, Andrew V. G. Chizmeshya, Chi Xu,

Jose Menéndez, and John Kouvetakis*

Department of Chemistry and Biochemistry and Department of Physics, Arizona State University, Tempe, Arizona 85287-1604, United States



RightsLink®

Home

Account Info

Help



ACS Publications
High quality. High impact.

Title: Ultra-Low-Temperature Epitaxy of Ge-based Semiconductors and Optoelectronic Structures on Si(100): Introducing Higher Order Germanes (Ge₃H₈, Ge₄H₁₀)

Author: Gordon Grzybowski, Liying Jiang, Richard T. Beeler, Tylan Watkins, Andrew V. G. Chizmeshya, Chi Xu, José Menéndez, and John Kouvetakis

Publication: Chemistry of Materials

Publisher: American Chemical Society

Date: May 1, 2012

Copyright © 2012, American Chemical Society

Logged in as:

Gordon Grzybowski

Account #:

3000613746

LOGOUT

PERMISSION/LICENSE IS GRANTED FOR YOUR ORDER AT NO CHARGE

This type of permission/license, instead of the standard Terms & Conditions, is sent to you because no fee is being charged for your order. Please note the following:

- Permission is granted for your request in both print and electronic formats, and translations.
- If figures and/or tables were requested, they may be adapted or used in part.
- Please print this page for your records and send a copy of it to your publisher/graduate school.

Synthesis and properties of monocrystalline Al(As₁-XPX)Si₃ alloys on Si(100)



RightsLink®

[Home](#)

[Account Info](#)

[Help](#)



Title: Synthesis and Properties of Monocrystalline Al(As₁-xPx)Si₃ Alloys on Si(100)
Author: G. Grzybowski, T. Watkins, R.T. Beeler, L. Jiang, D.J. Smith, A.V.G. Chizmeshya, J. Kouvetakis, and J. Menéndez
Publication: Chemistry of Materials
Publisher: American Chemical Society
Date: Jun 1, 2012
Copyright © 2012, American Chemical Society

Logged in as:
Gordon Grzybowski
Account #:
3000613746

[LOGOUT](#)

PERMISSION/LICENSE IS GRANTED FOR YOUR ORDER AT NO CHARGE

This type of permission/license, instead of the standard Terms & Conditions, is sent to you because no fee is being charged for your order. Please note the following:

- Permission is granted for your request in both print and electronic formats, and translations.
- If figures and/or tables were requested, they may be adapted or used in part.
- Please print this page for your records and send a copy of it to your publisher/graduate school.
- Appropriate credit for the requested material should be given as follows: "Reprinted (adapted) with permission from (COMPLETE REFERENCE CITATION). Copyright (YEAR) American Chemical Society." Insert appropriate information in place of the capitalized words.
- One-time permission is granted only for the use specified in your request. No additional uses are granted (such as derivative works or other editions). For any other uses, please submit a new request.

Monocrystalline Al(As_{1-x}N_x)Si₃ and Al(P_{1-x}N_x)_ySi_y alloys with diamond structures: New chemical approaches to semiconductors lattice matched to silicon

Monocrystalline Al(As_{1-x}N_x)Si₃ and Al(P_{1-x}N_x)_ySi_y Alloys with Diamond-like Structures: New Chemical Approaches to Semiconductors Lattice Matched to Si

Author: John Kouvetakis, Andrew V. G. Chizmeshya, Liying Jiang, Tylan Watkins, Gordon Grzybowski, Richard T. Beeler, Christian Poweleit, and José Menéndez

Publication: Chemistry of Materials
Publisher: American Chemical Society
Date: Aug 1, 2012
Copyright © 2012, American Chemical Society

Logged in as:
Gordon Grzybowski
Account #: 3000613746
[LOGOUT](#)

Quick Price Estimate

Permission for this particular request is granted for print and electronic formats, and translations, at no charge. Figures and tables may be modified. Appropriate credit should be given. Please print this page for your records and provide a copy to your publisher. Requests for up to 4 figures require only this record. Five or more figures will generate a printout of additional terms and conditions. Appropriate credit should read: "Reprinted with permission from {COMPLETE REFERENCE CITATION}. Copyright {YEAR} American Chemical Society." Insert appropriate information in place of the capitalized words.

• Portion is a required field. Please make a selection.

I would like to...	reuse in a Thesis/Dissertation	This service provides permission for reuse only. If you do not have a copy of the article you are using, you may copy and paste the content and reuse according to the terms of your agreement. Please be advised that obtaining the content you license is a separate transaction not involving Rightslink.
Requestor Type	Author (original work)	
Portion	make a selection	
Format	Print	
Select your currency	USD - \$	
Quick Price	Click Quick Price	